Organic Selective Contacts for Crystalline Silicon Solar Cells

Von der Fakultät für Mathematik und Physik
der Gottfried Wilhelm Leibniz Universität Hannover
zur Erlangung des Grades

Doktor der Naturwissenschaften
Dr. rer. nat.

genehmigte Dissertation von

M. Sc. Marc-Uwe Halbich

2021

Kurzzusammenfassung

Das lochleitende Polymer Poly(3,4-ethylendioxythiophen):Poly(styrolsulfon-säure) [PEDOT:PSS] ist dafür bekannt, dass es kristalline Siliziumoberflächen effektiv passiviert und gleichzeitig einen geringen Kontaktwiderstand für Löcher bietet. PEDOT:PSS kann daher als lochselektive Kontaktschicht in Siliziumsolarzellen verwendet werden. In dieser Arbeit werden PEDOT:PSS/c-Si-Solarzellen mit phosphordiffundierter Vorderseite und PEDOT:PSS/c-Si-Heteroübergang auf der Rückseite ('BackPEDOT'-Solarzellen) hergestellt und die Selektivität von PEDOT:PSS auf kristallinen Silizium in Abhängigkeit der Prozessparameter wird untersucht. Auf texturierten Siliziumoberflächen, die mit PEDOT:PSS beschichtet sind, beobachten wir erstmals eine zusätzliche dünne organische Schicht, die einen erhöhten Schwefelgehalt aufweist und für die Passivierung der Siliziumoberfläche verantwortlich ist. Die maximale Kurzschlussstromdichte von BackPEDOT-Solarzellen nimmt mit abnehmender PEDOT:PSS-Schichtdicke zu. Um jedoch die parasitäre Absorption weiter zu reduzieren, wird der Einfluss von Additiven zur PEDOT:PSS Dispersion untersucht. In dieser Arbeit konnte dabei erstmals nachgewiesen werden, dass die Beimischung von Sorbitol zur PEDOT:PSS Dispersion nicht nur die parasitäre Absorption im PEDOT:PSS reduziert, sondern auch die Passivierqualität des PEDOT:PSS/c-Si-Heteroübergangs verbessert. Eine maximale Energieumwandlungseffizienz von 20,6% wurde für PEDOT:PSS mit Beimischung von Sorbitol erreicht. Dies ist der höchste Wirkungsgrad, der bisher für eine c-Si-Solarzelle mit einem organischen selektiven Kontakt erreicht wurde. Darüber hinaus wird die Bandverbiegung innerhalb des Siliziums des PEDOT:PSS/c-Si-Heteroübergangs durch eine neu eingeführte Methodik untersucht, die auf dem DRM-Effekt (Depletion Region Modulation) basiert. Zum ersten Mal zeigen wir, dass die Beimischung von Sorbitol zur PEDOT:PSS-Dispersion die chemische Passivierung der Grenzfläche verbessert, die Bandverbiegung im Silizium zur PEDOT:PSS Grenzfläche hin jedoch unverändert bleibt.

Schlagworte: Siliziumsolarzelle, Selektiver Kontakt, PEDOT:PSS/c-Si Heteroübergang

Abstract

The hole-conducting polymer poly(3,4-ethylenedioxythiophene):poly(styrene-sulfonic acid) [PEDOT:PSS] is known to effectively passivate crystalline silicon surfaces and to simultaneously provide a low contact resistance for holes. PEDOT:PSS can therefore be applied as a hole-selective, passivating contact layer in silicon solar cells. In this thesis, PEDOT:PSS/c-Si solar cells with phosphorus-diffused front and PEDOT:PSS/c-Si heterojunction at the rear ('BackPEDOT' solar cells) are manufactured and the selectivity of PEDOT:PSS on crystalline silicon is examined. On random-pyramid-textured silicon surfaces covered with PEDOT:PSS we observe for the first time an additional thin organic layer, which has an increased sulfur content in comparison to the bulk PEDOT:PSS and which is responsible for the passivation of the silicon surface. The maximum short-circuit current density increases with decreasing PEDOT:PSS layer thickness. In order to further reduce the parasitic absorption, the impact of additives to the PEDOT:PSS dispersion is investigated. We hereby demonstrate for the first time, that the admixture of sorbitol not only reduces the parasitic absorption in PEDOT:PSS, but also improves the passivation quality of PEDOT:PSS on silicon. A maximum energy conversion efficiency of 20.6% of a BackPEDOT solar cell was achieved for PEDOT:PSS with sorbitol admixture. This is the highest efficiency achieved so far for a c-Si solar cell with an organic selective contact. Furthermore, the band bending within the silicon bulk of the PEDOT:PSS/c-Si junction is examined by a newly introduced methodology based on the Depletion Region Modulation (DRM) effect. For the first time we demonstrate that admixture of sorbitol to the PEDOT:PSS dispersion improves the chemical interface passivation, but the band bending within the silicon bulk towards the PEDOT:PSS/c-Si interface remains unaffected.

Keywords: silicon solar cell, selective contact, PEDOT:PSS/c-Si heterojunction

Contents

1 Introduction

With the development of the first solar cell in history, a new way of producing energy opened up. Suddenly it was possible to produce energy sustainably without the use of fossil fuels. The development of the first solar cell goes back to Becquerel's discovery of the photoelectric effect in 1839, which made it possible to generate electricity from solar energy. The first solar cells, which were based on silicon, achieved 6.0% energy conversion efficiency in the beginning and 11.0% in later years[1]. This was the first major leap in the development of silicon solar cell technology. Today, a large market has emerged from this, which will guarantee a supply of inexpensive regenerative energy for the coming generations. Today, there are many different solar cell concepts that are designed for the highest possible energy conversion efficiencies, while at the same time keeping the process flow simple and the production costs low. Today, industrial silicon-based solar cells achieve energy conversion efficiencies of over 21.0%[2], with a record efficiency of 22.6%[3]. At such a high level, other limitations play a significant role than in the past, such as the passivation of the silicon surface states, especially below the metal contacts of the solar cell, to avoid recombination of the charge carriers at the interface between the silicon and the metal contact. The selectivity of the contacts, where the conductivity is large for one type of carrier and low for the other one, is the crucial parameter for assessing the contact quality[4]. The identification and implementation of new passivating contact materials, allowing high carrier selectivities (i.e. low contact resistance for one type of carrier, and low surface recombination for the other one), is the next step towards very high efficiencies in silicon-based photovoltaics. Currently the record efficiency for a silicon-based solar cell with passivating contacts is 26.7%[5]. The passivation layer used in this solar cell is intrinsic amorphous silicon, which ensures an excellent passivation of the c-Si surface. Either n- or p-doped amorphous silicon is used to determine the selectivity type of the contact. Whether a contact layer is selective for electrons or holes depends on its work function. For example, in the case of crystalline silicon, a layer with a large work function is selective for holes, while a rather low work function ensures the selectivity for electrons[6].

1 Introduction

The material of the selective layer is in principle free to choose, and alternative materials such as metal oxides and conductive polymers have been shown to be usable[7, 8]. An example of a conductive polymer, that provides effective silicon surface passivation and a sufficiently low contact resistivity for holes, is poly(3,4-ethylenedioxythiophene):poly(styrenesulfonic acid) (PEDOT:PSS). The advantage of using PEDOT:PSS as a hole-selective contact on c-Si is the simple processing of the organic dispersion at room temperature as well as the cost effectiveness in the production of the polymers. Neither high temperature steps nor ultra-high vacuum systems are required for the deposition, which has the potential of reducing the solar cell production costs and keeps the process flow simple. In this thesis, the properties of PEDOT:PSS as hole-selective layer in silicon solar cells with phosphorus-diffused front and PEDOT:PSS/c-Si heterojunction at the rear (so called 'BackPEDOT' solar cells) are investigated. A BackPEDOT solar cell is schematically shown in Figure 1.1. We examine the impact of organic
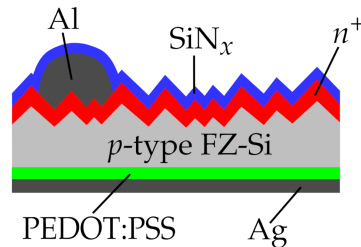
Figure 1.1: Cross-section of a BackPEDOT solar cell, as developed in this thesis.

additives to the PEDOT:PSS dispersion on the carrier selectivity, and on the optical transparency of PEDOT:PSS. In addition, we introduce a novel contactless characterization methodology for the organic-silicon heterojunction, based on the "Depletion Region Modulation" (DRM) effect.

In the following, the content of the Chapters of the thesis is briefly described:

Chapter 2 briefly summarizes the state of research on the topic of silicon solar cells with organic selective contacts based on PEDOT:PSS before the beginning of the thesis work.

Chapter 3 describes the theoretical background of organic semiconductors and the characterization methods applied in this thesis.

Chapter 4 focuses on the implementation of PEDOT:PSS layers into BackPEDOT solar cells. First, the specific contact resistance of the PEDOT:PSS/c-Si junction

and the passivation of the junction are characterized as an function of process causalities. It is shown for the first time, that thinner PEDOT:PSS layers in BackPE-DOT cells lead to reduced parasitic absorption losses, increasing the cells photocurrent.

The PEDOT:PSS is implemented into BackPEDOT solar cells and in **Chapter 5**, different additives to the PEDOT:PSS Dispersion are examined, which are supposed to reduce the parasitic absorption in PEDOT:PSS. The impact of the additives on the transparency of the PEDOT:PSS layer and the impact on the passivation quality on c-Si is examined. PEDOT:PSS layers with additives are implemented into solar cells and the effects of the admixture of the additives on the solar cell parameters are investigated. It is demonstrated for the first time that adding sorbitol to the PEDOT:PSS dispersion not only reduces the parasitic absorption in PEDOT:PSS, and thus improves the cells photocurrent, but it also improves the surface passivation quality, which increases the open-circuit voltage. The process parameters are optimized to achieve the highest energy conversion efficiency of 20.6% achieved so far for a silicon solar cell with an organic selective contact.

For a better understanding of the passivation effect of PEDOT:PSS on c-Si, in **Chapter 6** the band bending within the n-type silicon bulk of the PEDOT:PSS/c-Si junction is investigated by a newly introduced methodology, based on the Depletion Region Modulation (DRM) effect. For the first time we demonstrate, that admixture of sorbitol to the PEDOT:PSS dispersion improves the chemical interface passivation, but the band bending within the n-type silicon bulk remains unchanged.

2 Silicon Solar Cells with Organic Selective Contact

One of the first silicon solar cells with organic selective contact layers was published by Avasthi et al.[9]. The organic layer consisting of a stack of poly(3-hexylthiophene) (P3HT) and PEDOT:PSS replaced the *p-n* junction of a planar *n*-type silicon solar cell on the front side of the cell, leading to relatively low short-circuit current densities J_{sc} due to the predominant parasitic absorption losses within the PEDOT:PSS. The rear side of the cell was metallized on the entire surface, leading to large recombination losses at the cell rear. In 2011, this type of solar cell achieved an energy conversion efficiency of 10.1% with a short-circuit current density J_{sc} of $29.0\,\mathrm{mA/cm^2}$ and an open circuit voltage V_{oc} of $590\,\mathrm{mV}$. A schematic representation of the cell concept according to Avasthi et al.[9] is shown in Figure 2.1a. In 2012, He et al.[10] achieved an efficiency of 11.3% with the same cell design using a thin native silicon dioxide in-between the PEDOT:PSS layer and the silicon wafer in order to improve the passivation of the silicon surface. Table 2.1 summarizes some milestones in the evolution of crystalline silicon solar cells featuring organic selective contacts. Note thet there are further studies combining silicon solar cells with PEDOT:PSS achieving efficiencies of over 11.0%[16, 17, 18, 19]. In 2013, Schmidt et al.[11] then introduced random-pyramid texturing underneath the PEDOT:PSS layer on the front of the cell and a phosphorus-diffused back surface field on the solar cell rear to reduce recombination at the metal/silicon junction, which further increased the efficiency to 12.3%. However, it was also shown, that the V_{oc} values of $603\,\mathrm{mV}$ were still limited by recombination of the fully metallized rear of the cell. The J_{sc} values were limited by the predominant parasitic absorption in the PEDOT:PSS layer on the textured front of the cell. A schematic representation of the cell concept according to Schmidt et al.[11] is shown in Figure 2.1c. In 2014, Avasthi et al.[12] combined PEDOT:PSS as hole-selective contact layer on the front of the cell, with titanium dioxide at the cell rear as electron-selective layer. By passivating the rear side of the solar cell with titanium dioxide, higher open-circuit voltages up to $620\,\mathrm{mV}$

Table 2.1: Milestones in the evolution of crystalline silicon solar cells featuring organic selective contacts.

Author	Year	J_{sc} [mA/cm^2]	V_{oc} [mV]	*FF* [%]	η [%]
Avasthi et al.[9]	2011	29.0	590	59.0	10.1
He et al.[10]	2012	26.3	600	70.9	11.3
Schmidt et al.[11]	2013	29.0	603	70.6	12.3
Avasthi et al.[12]	2014	29.0	620	72.1	12.9
Zielke et al.[13]	2014	39.0	663	66.3	17.1
Zielke et al.[14]	2015	38.9	657	80.6	20.6
Gogolin et al.[15]	2017	31.7	680	78.7	16.0

were achieved, leading to a better cell efficiency of 12.9% (the cell structure is shown in Figure 2.1b). The short-circuit current densities were, however, still limited to $J_{sc} = 29.0\,\text{mA/cm}^2$ by the parasitic absorption in the PEDOT:PSS layer on the cell front. In order to reduce the parasitic absorption in the PEDOT:PSS layer and thus improve the J_{sc} values, Zielke et al.[13] have relocated the PEDOT:PSS layer to the cell rear in the so-called BackPEDOT solar cell concept, where the hole-selective PEDOT:PSS layer is now located on the cell rear (see Figure 2.1d), whereas the front side of the cell is random-pyramid-textured and has a conventional phosphorus-diffused emitter. Silicon nitride is used for emitter passivation of the front and as anti-reflex coating. The cell structure according to Zielke et al.[13] is also shown schematically in Figure 2.1d. In addition, higher efficiencies were obtained by switching from *n*-type silicon to *p*-type silicon base material[14]. These efforts resulted in record J_{sc} values up to $39.0\,\text{mA/cm}^2$ and solar cell efficiencies of over 17%. Best V_{oc} values of 663 mV were achieved. Zielke et al. further improved the PEDOT:PSS dispersion and achieved solar cell efficiencies exceeding 20%[20] by improving the fill factor *FF* of the BackPEDOT solar cells. The improvement of the *FF* was achieved by optimizing the treatment of the silicon surface before PEDOT:PSS deposition. Furthermore, Gogolin et al.[15] have shown that the maximum V_{oc} value of 663 mV is strongly limited by the recombination at the conventional phosphorus-diffused front. In combination with a well-passivating electron-selective amorphous silicon layer stack on the textured solar cell front and PEDOT:PSS on the solar cell rear as hole-selective contact, V_{oc}
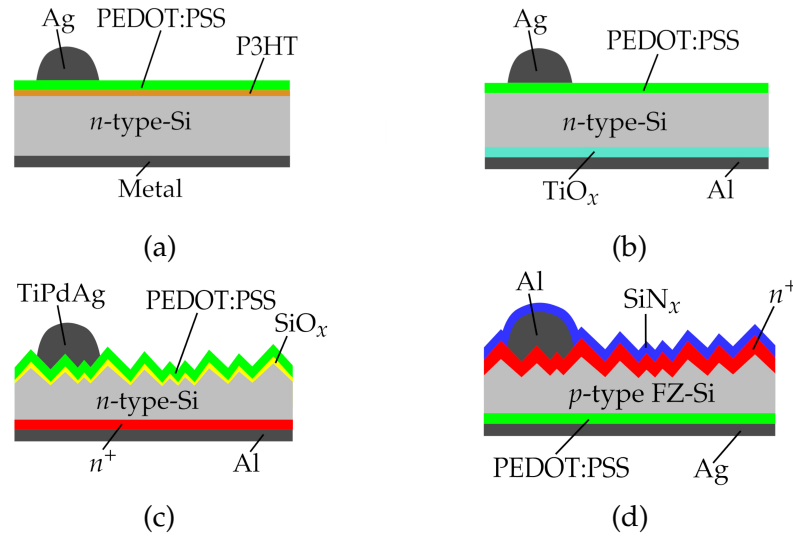
Figure 2.1: (a) First solar cell structure including an organic hole selective layer at the cell front and an n-type silicon substrate according to Avasthi et al.[9]. (b) Solar cell structure according to Avasthi et al.[12] adding titanium dioxide as electron-selective layer on the solar cell rear. (c) Organic-silicon solar cell on n-type silicon featuring a random-pyramid-textured front with a SiO_x tunneling layer and a phosphorus diffused rear according to Schmidt et al.[11]. (d) BackPEDOT solar cell concept with PEDOT:PSS layer relocated to the cell rear to reduce parasitic absorption losses according to Zielke et al.[13].

values of 680 mV (and 688 mV, if the cell was measured without a shadow mask) were achieved[15]. Still it turned out that even for the BackPEDOT cell, J_{sc} is limited by parasitic free-carrier absorption within the PEDOT:PSS layer of infrared photons reaching the cell rear[13, 14, 20].

3 Theory and Characterization Methods

3.1 Organic Semiconductors

If carbon is present in the atomic composition of a material and a delocalized π-electron system exists on the molecule or polymer[21], the material is called an organic semiconductor. Organic semiconductors exhibit a electrical conductivity in the range of 10^{-5} S/cm to 10^{-1} S/cm[22]. The length of the region over which a delocalized π-electron system can form is called the conjugation length. By sp^2-hybridization of the carbon atoms, in which one s-orbital is mixed with three of four p-orbitals, three sp^2-hybrid orbitals are formed, which can establish σ-bonds to the neighbouring atoms. The electron in the remaining p_z-orbital, which is not involved in the hybridization, can form a π-bond with electrons in p_z-orbitals of the neighbouring atoms if these are also sp^2-hybridized. This configuration results in a double bond between carbon atoms consisting of a σ- and a π-bond. Alternating single and double bonds between carbon atoms result in a delocalized π-electron system[21]. In the case of benzene, for example, two electrons of each carbon atom form bonds to their neighbours, one electron bonds one hydrogen atom to the carbon atom and one electron remains per atom. The six remaining electrons in the p_z-orbitals form three π-bonds. Since it is not determined with which of the three hybrid orbitals a π-bond is formed, there are two possibilities in the case of benzene. The two possibilities are shown schematically in Figure 3.1. The bond length between carbon atoms with a double bond
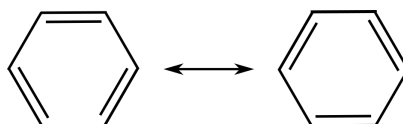

Figure 3.1: Schematic representation of the mesomeric bonding structures of benzene.

is smaller than the bond length between carbon atoms with a single bond. In

benzene, however, the bond length between all carbon atoms is the same regardless of their bond[23]. The real state can be explained by a superposition of both bonding structures, which is associated with the formation of a delocalized π-electron system. This delocalized π-electron system exists along the carbon ring with the electrons being present as a delocalized charge cloud above and below the entire conjugation length of the molecule [24]. The hybrid orbitals of a carbon atom, as well as the π-electron system resulting from the p_z-orbitals are schematically shown in the example of benzene in Figure 3.2. An atom has orbitals, which
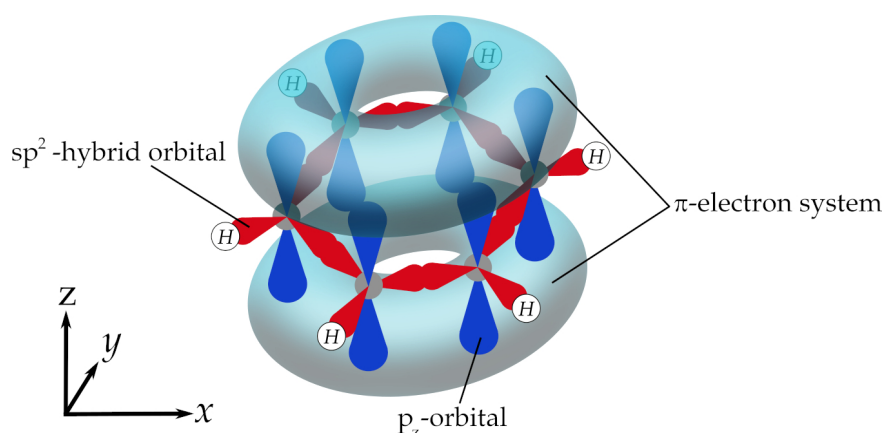

Figure 3.2: Schematic representation of the sp^2-hybridized orbitals (red clubs) and the p_z-orbitals (blue clubs) of the carbon atoms (grey spheres) and the delocalized π-electron system (turquoise doughnut) of benzene.

can be occupied by electrons. If the atomic orbitals overlap in a chemical bond to form molecular orbitals, they split up into bonding and anti-bonding orbitals. The energetically higher orbital is the anti-bonding molecular orbital and the energetically lower orbital is the bonding molecular orbital. In the ground state all bonding orbitals are occupied and all non-bonding orbitals are unoccupied. The highest bonding orbital is called the highest occupied molecular orbital (HOMO) and the lowest anti-bonding orbital is called lowest unoccupied molecular orbital (LUMO). Since π-bonds have a lower bonding energy than σ-bonds, there is a smaller energy split between the bonding and anti-bonding π-molecular-orbital than the split between the bonding and anti-bonding σ-molecular-orbital. The energetic splitting between the π-molecular orbitals can be compared to the band gap of an inorganic semiconductor. The energy difference between the two π-molecular-orbitals is in the visible range for many organic semiconductors, the energy difference between the σ-molecular-orbitals is in the UV range[25]. The band gap depends not only on the type of atomic bond, but also on the conjugation length. The larger the conjugation length, the smaller the energetic distance

between HOMO and LUMO becomes, since the electrons are delocalized over a larger range. The HOMO and LUMO molecule orbitals are each limited to one molecule. The energetic position of HOMO-LUMO levels varies slightly from molecule to molecule, as it depends on the interactions of the molecules with neighbouring molecules and the polarizability of the environment. The state density $D(E)$ can be described by a Gaussian distribution[26]:

$$D(E) = \frac{N}{\sqrt{2\pi b}} \exp\left(\frac{-(E - E_0)^2}{2b^2}\right) ,$$

(3.1)

with E being the energy, E_0 being the center of the Gaussian distribution and N being the spatial density of states. b is the width of the Gaussian distribution of the density of states. For organic semiconductors, b is typically in the range of $100\,\mathrm{meV}$[26]. Figure 3.3 shows the density of states schematically for the HOMO energy levels as well as for the LUMO energy levels. If an electron on a molecule
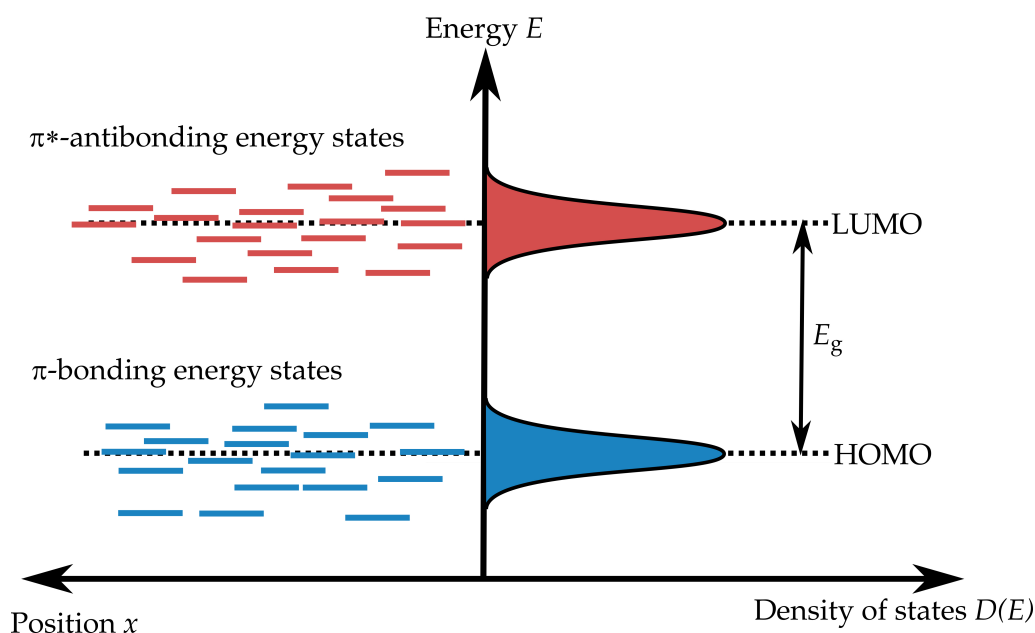
Figure 3.3: Schematic representation of the density of states $D(E)$ in an organic semiconductor.

is excited from HOMO into LUMO, an hole remains in HOMO, which can interact with the excited electron via the Coulomb interaction. The resulting electron-hole pair is a so-called exciton. The exciton is charge-neutral and can move through the organic semiconductor by hopping from molecule to molecule. Since electron and hole are each localized on one molecule, these excitons are described in organic semiconductors as Frenkel excitons[27].

3.1.1 The Hole-Conducting Organic Semiconductor PEDOT:PSS

The synthesis of Poly(3,4-ethylenedioxythiophene):poly(styrenesulfonic acid) [PE-DOT:PSS] was patented in 1988[28] by Bayer AG. Since the organic compound PEDOT cannot be synthesized as a single polymer, PSS is used as a counter ion in the synthesis, forming a water-soluble PEDOT:PSS complex. The PEDOT:PSS complex is dissolved in water as small gel particles with an average diameter of 25 nm [8]. A schematic representation of the PEDOT:PSS gel particles and the chemical structure of PEDOT and PSS are shown in Figure 3.4. A typical solid
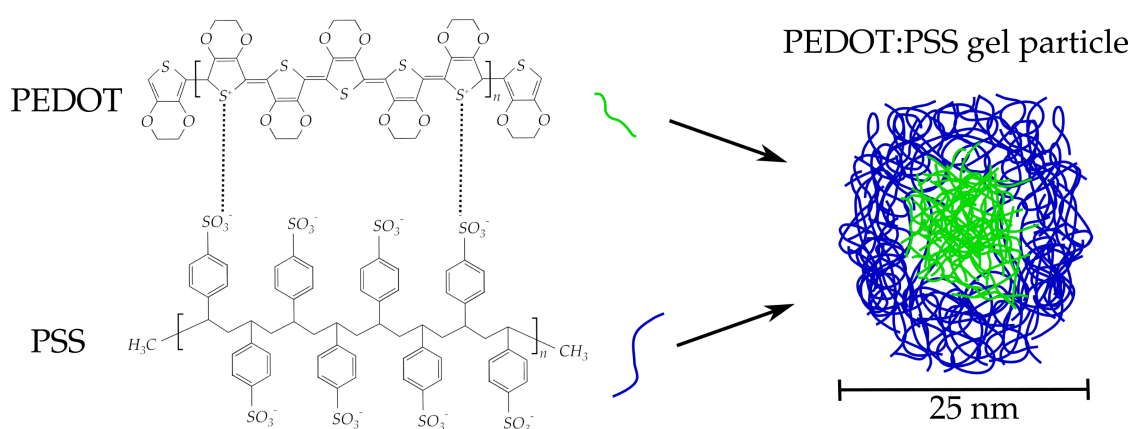

Figure 3.4: Chemical structure of PEDOT and PSS (left) and PEDOT:PSS as gel particle as present in an aqueous dispersion (right).

content in an aqueous PEDOT:PSS dispersion is 2.0 wt.% PEDOT:PSS. If this dispersion is applied, for example using spin coating, a solid PEDOT:PSS film is formed from the gel particles during the annealing on a hotplate. Other deposition techniques such as dip-coating, spraying-coating, slot-die-coating or printing are also possible. The conductivity of PEDOT:PSS can be varied over a broad range of 10^{-5} S/cm to 1000 S/cm by adding additives such as ethylene glycol or dimethyl sulfoxide[29]. The structure of the PEDOT:PSS film is determined by the structure of the gel particles[30]. The gel particles are stacked as spherical packing and are dried by thermal annealing and shrink to ellipsoids. PSS rich lamellae are formed, which form pancake-like shapes from the PEDOT:PSS gel particles. PEDOT is located between the PSS lamellae, which of course is also the reason for the good lateral conductivity of PEDOT:PSS. The structure taken from Nardes et al.[31] for a PEDOT:PSS thin film is shown schematically in Figure 3.5. In addition to the simple processing techniques, PEDOT:PSS has entered
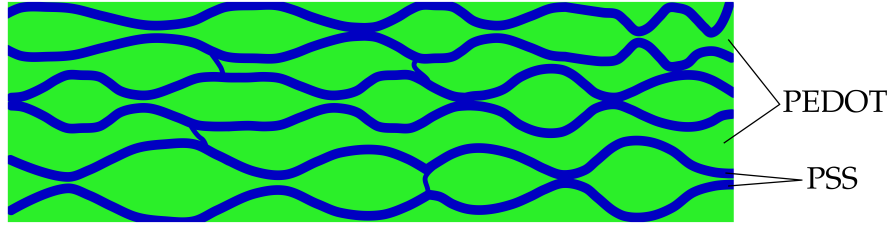
Figure 3.5: Cross-sectional view of the schematic morphological model for PE-DOT:PSS films according to Nardes et al.[31]. The PSS-rich lamellas are formed by stacking the PEDOT:PSS gel particles.

mass production especially for its material properties. Besides the high conductivity of up to $1000\,S/cm$, PEDOT:PSS is thermally stable up to $200°C$[8]. Since it has a transparency of up to 80% in the visible wavelength range and its work function can be varied over a broad range from 4.7 to 5.6 eV, PEDOT:PSS is predestinated as a transparent electrode. Today, PEDOT:PSS is mainly applied as antistatic coating[32] on surfaces and is used in organic electrochemical transistors, where the drain current is controlled by the injection of holes from PEDOT:PSS into a semiconductor channel[33].

3.2 Selectivity

If a selective layer is used beneath a contact, good passivation properties for the minority-carriers and a good transport of the majority-carriers must be provided. Both properties, the suppression of minority carrier recombination as well as good majority-carrier transport, define the selectivity S_{10} of the carrier-selective contact. Brendel et al.[34] introduced a quantitative definition of the selectivity. The minority-carrier recombination current density J_{m} into the selective contact is given by:

$$J_{\mathrm{m}} = J_0 \left(\exp \left(\frac{V}{V_{\mathrm{th}}} \right) - 1 \right),$$

(3.2)

where J_0 is a recombination current density parameter and V_{th} is the thermal voltage at a temperature of $298.15\,K$. The Voltage V depends on the internal quasi-Fermi level splitting of the quasi-Fermi potentials of electrons Φ_n and holes Φ_p at the contact. Since the resistance of the minority-carriers V/J_{m} is voltage dependent, the inverse slope of the current voltage curve around zero is used as

characteristic value for the contact resistivity of the minority-carriers ρ_m:

$$\rho_m = \left(\frac{dJ_m}{dV} \Big|_{V=0} \right)^{-1} = \frac{V_{th}}{J_0}. \tag{3.3}$$

By assuming a linear relationship between the voltage and the recombination current density of the majority-carriers $J_M = V / \rho_c$, the contact resistance of the majorities ρ_M is given by:

$$\rho_M = \left(\frac{dJ_M}{dV} \Big|_{V=0} \right)^{-1} = \rho_c. \tag{3.4}$$

With the ratio of the majority-carrier resistance to the minority-carrier resistance, the selectivity S is defined:

$$S = \frac{\rho_m}{\rho_M} = \frac{V_{th}}{J_0 \rho_c}. \tag{3.5}$$

In order to avoid large numbers, the logarithmically scaled selectivity S_{10} is used:

$$S_{10} = \log_{10} \left(\frac{V_{th}}{J_0 \rho_c} \right). \tag{3.6}$$

The selectivity S_{10} allows a direct comparison of the selectivities of different contacts with a single number. Figure 3.6 shows J_0 values in dependence of the specific contact resistance ρ_c for different selective contacts. The data was taken from Schmidt et. al.[35]. The orange lines in Figure 3.6 are lines of constant selectivity S_{10}. The selectivity S_{10} values are usually between $S_{10} = 11.0$ and 17.0 for selective contact layers used in silicon solar cells. $SiO_x/poly\text{-}Si(n^+)$ electron-selective layers, featuring a interfacial oxide, show the largest selectivities S_{10} of around 16.0. The highest selectivity of PEDOT:PSS achieved in this thesis is $S_{10} = 13.2$. The maximum achievable combined selectivity $S_{e\,\&\,h,max}$ of an electron-selective and a hole-selective contact layer, is given by[36]:

$$S_{e\,\&\,h,max} = \frac{1}{\left(\frac{1}{\sqrt{S_e}} + \frac{1}{\sqrt{S_h}} \right)^2}. \tag{3.7}$$

For a BackPEDOT solar cell with phosphorus-diffused front (which provides an electron-selectivity of 12.0[34]) and PEDOT:PSS (which provides a maximum hole-selectivity of 13.2 in this thesis), a combined selectivity $S_{e\,\&\,h,max}$ of 11.8 is obtained. With the given combined selectivity $S_{e\,\&\,h,max}$, the maximum achievable
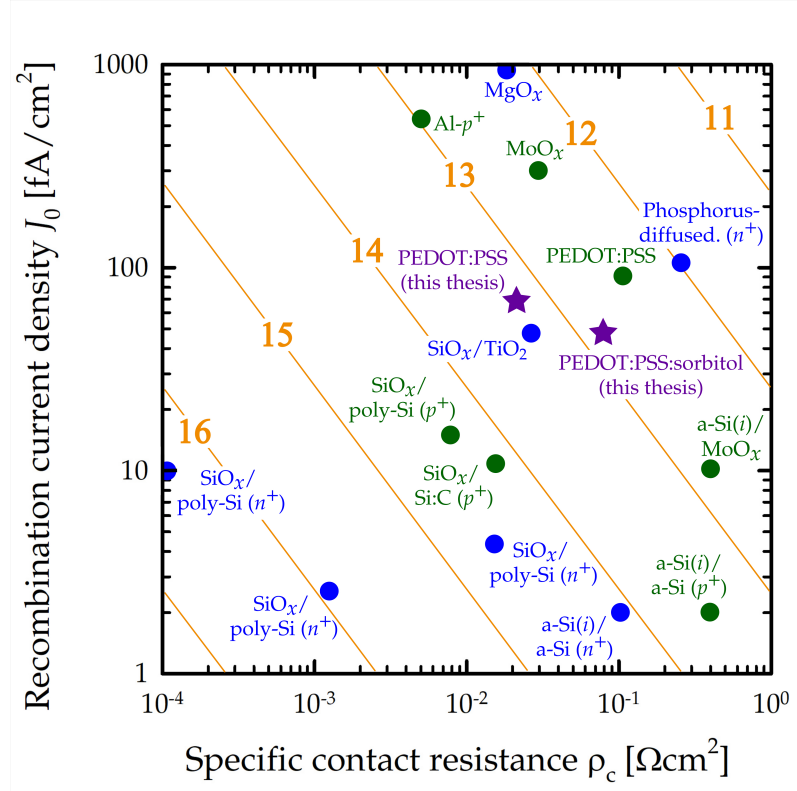
Figure 3.6: Recombination current density parameters J_0 in dependence of the contact resistances ρ_c for electron-selective layers (blue symbols) and hole-selective layers (green symbols). The orange lines are lines of constant selectivity S_{10}. The highest selectivity of PEDOT:PSS achieved in this thesis is also shown (purple stars).

efficiency η_{max} can be calculated[34]:

$$\eta_{max} = (2.452\, S_{e\,\&\,h,max} - 4.240)\%\,.\tag{3.8}$$

Using Equation (3.8) and the combined selectivity of 11.8, the maximum achievable efficiency η_{max} for BackPEDOT solar cells is 24.7%.

3.3 Surface Recombination

A semiconductor has an ordered crystal structure in the volume, but the crystal structure is interrupted at the surface of the semiconductor. In the case of silicon this leads to unsaturated bonds, the so-called dangling bonds. The energy levels of the dangling bonds are within the band gap in the case of silicon and are therefore recombination active. Minimizing the surface recombination, and thus also minimizing the surface states, is important for the production of good solar cells.

The saturation of the dangling bonds is a chemical passivation and is usually achieved by a dielectric film. Dielectric materials for passivation of silicon surfaces are for example silicon dioxide[37], silicon nitride[38, 39, 40, 41, 42, 43], aluminum oxide[44, 45, 46, 44] or amorphous silicon[47, 48, 49]. In addition to their passivation properties, these films also provide an effective anti-reflection layer on the solar cell front, which maximizes the light absorption of the solar cell. The carrier concentration near the surface can be adjusted to reduce the surface recombination. Since recombination depends on the concentration of both electrons and holes, the absence of a carrier species limits the recombination. An electric field that repels a type of charge carrier can therefore reduce recombination to a minimum. This is called field effect passivation. Field effect passivation is accomplished by a fixed charge on a capping dielectric film[50]. Silicon nitride contains fixed positive charges[51] in addition to the chemical passivation of the silicon surface, while aluminum oxide contains fixed negative charges[51]. One way to describe the surface recombination is by the saturation current density parameter J_0[52], the effective lifetime τ_{eff}, which is composed of bulk and surface recombination of a *p*-type silicon wafer with doping concentration N_A and thickness W is given by[53]:

$$\frac{1}{\tau_{eff}} = \frac{1}{\tau_{intrinsic}} + \frac{1}{\tau_{SRH}} + 2J_0\frac{(N_A + \Delta n)}{qWn_i^2}. \qquad (3.9)$$

The recombination current density parameter J_0[52] is a parameter to describe the recombination at the silicon surface. The factor 2 takes into account samples with two symmetrical surfaces. A method to determine J_0 from a lifetime measurement is the so-called Kane and Swanson method[54]. There are three requirements to be fulfilled. Firstly, high injection conditions must be present: $\Delta n \gg N_A$, secondly the Shockley-Read-Hall lifetime must be constant in high injection conditions and thirdly the excess charge carriers must be homogeneously distributed in the bulk silicon. This results in:

$$\frac{1}{\tau_{eff}} - \frac{1}{\tau_{intrinsic}} = \frac{1}{\tau_{SRH}} + 2J_0\frac{\Delta n}{qWn_i^2}. \qquad (3.10)$$

By plotting $\frac{1}{\tau_{eff}} - \frac{1}{\tau_{intrinsic}}$ as a function of the excess carrier concentration Δn, J_0 can be determined. Figure 3.7 shows $\frac{1}{\tau_{eff}} - \frac{1}{\tau_{intrinsic}}$ as a function of the excess carrier concentration Δn. Using a linear fit with slope m, J_0 can be determined with:
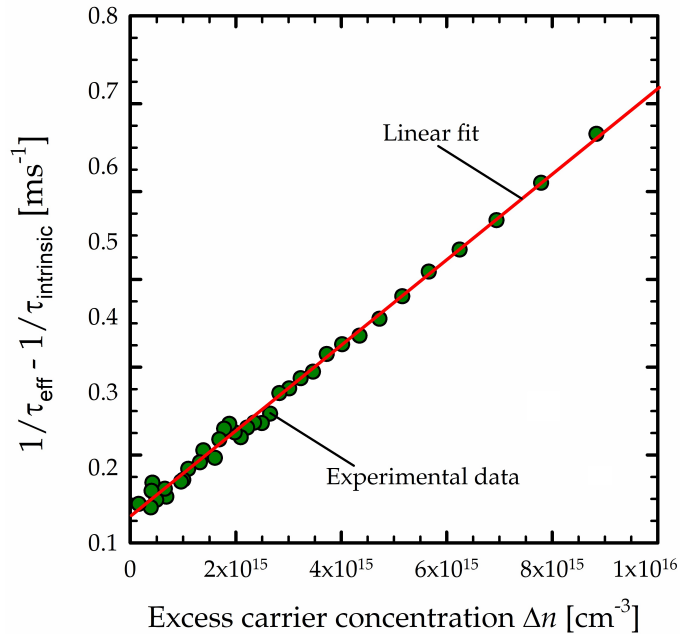
$$J_0 = m\frac{qWn_i^2}{2}. \qquad (3.11)$$

Figure 3.7: Measured inverse lifetime τ_{eff} minus inverse lifetime $\tau_{\mathrm{intrinsic}}$ as a function of the excess carrier concentration Δn. J_0 is determined using a linear fit of the measured data (red line) according to the Kane and Swanson method.

3.3.1 Influence of Surface Charges on the Surface Recombination

In a semiconductor, the conduction and valence bands are usually considered constant over the position within the bulk, but in the area close to the semiconductor surface a band bending can occur. The reason for this band bending can be charges on the semiconductor surface or charge carriers trapped in interface states of the surface interface. Further causes can be a strong doping concentration at the surface or a junction with a material with a different work function. The area near the surface where band bending occurs in the semiconductor is called the surface space charge region. If charge carriers are generated in a semiconductor with a band bending at the surfaces, the excess charge carrier concentration Δn is only present in the bulk and at the edge of the surface space charge region. Within the surface space charge region, the electron and hole concentrations are now position-dependent due to the band bending Ψ_s, which iteself also depends on the position in the surface space charge region. The quasi-Fermi po-

tentials of electrons Φ_n and holes Φ_p in the bulk and hence at the edge of the surface space charge region can be calculated by the equations[55]:

$$\Phi_n = -\frac{k_B T}{q} \ln \left(\frac{n_0 + \Delta n}{n_i} \right) \quad , \text{ and } \quad \Phi_p = +\frac{k_B T}{q} \ln \left(\frac{p_0 + \Delta p}{n_i} \right). \tag{3.12}$$

Furthermore, the surface carrier concentrations n_s and p_s as a function of the band bending Ψ_s can be calculated by[56]:

$$n_s = (n_0 + \Delta n) \exp \left(\frac{+q\Psi_s}{k_B T} \right), \text{ and } \tag{3.13}$$

$$p_s = (p_0 + \Delta p) \exp \left(\frac{-q\Psi_s}{k_B T} \right). \tag{3.14}$$

Combining this with Equation (3.12) results for the surface concentrations of electrons and holes.

$$n_s = n_i \exp \left(\frac{-q\Phi_n}{k_B T} \right) \exp \left(\frac{+q\Psi_s}{k_B T} \right), \text{ and } \tag{3.15}$$

$$p_s = n_i \exp \left(\frac{+q\Phi_p}{k_B T} \right) \exp \left(\frac{-q\Psi_s}{k_B T} \right). \tag{3.16}$$

The recombination rate is now obtained completely analogously for derivation in the bulk via the Shockley-Read-Hall formalism. It is assumed that there are no transitions of charge carriers between two interface states, but only transitions between an interface state and the conduction and valence band can take place. Interface states are usually continuously distributed across the band gap. The reason for this continuous distribution in the case of the dangling bond conditions are statistical variations of the bond angles and the distances to the nearest neighbouring atoms of defects[57]. The surface recombination rate U_s is thus given by:

$$U_s = \int_{E_v}^{E_c} \frac{(n_s p_s - n_i^2) v_{th} D_{it}(E)}{(n_s + n_1(E)) \sigma_p^{-1}(E) + (p_s + p_1(E)) \sigma_n^{-1}(E)} dE. \tag{3.17}$$

Where D_{it} is the density of surface/interface states within the band gap and v_{th} the thermal velocity with $v_{th} = 1.0 \times 10^7$ cm/s. The Temperature is set to T = 300 K. σ_n and σ_p are the characteristic capture cross-sections for electrons and holes. It should be noted that the interface state density D_{it}, the capture cross sections and the densities n_1 and p_1 are energy-dependent parameters. For simplicity, simulation calculations often assume that the surface recombination takes place via a

state with a fixed energy level. The fundamental surface recombination veloci-
ties for electrons and holes S_{n0} and S_{p0}, which describe the surface recombination
without band bending, can be calculated with the following equation:

$$S_{p0/n0} = \int_{E_v}^{E_c} v_{\text{th}} D_{\text{it}}(E) \sigma_{p0/n0}(E) \, dE. \tag{3.18}$$

Furthermore, with the surface recombination rate U_s, the effective surface recom-
bination velocity S_{eff} can be determined by the following equation:

$$S_{\text{eff}} = \frac{U_s}{\Delta n}. \tag{3.19}$$

U_s can be determined numerically with the extended Shockley-Read-Hall for-
malism. This formalism was proposed by Grove and Fitzgerald[58] and was later
developed further by Girisch et al.[59]. Aberle et al. used the extended Shockley-
Read-Hall formalism for the first time to address the injection dependence of sil-
icon surfaces passivated with SiO_2[60]. Ψ_s is numerically determined with the
iterative process of Girisch et al.[59]. It is assumed that in the overall system
charge neutrality must be assured. The total charge consists of the charge in the
silicon Q_{Si}, the charge in the interface states Q_{it} and the fixed charge Q_f within
the dielectric passivation layer. A band diagram of the physical situation of the
band bending in the surface space charge region of a semiconductor, as well as
all important parameters are shown schematically in Figure 3.8. The charges Q_{Si}
and Q_{it} depend both on the band bending Ψ_s and on the quasi-Fermi-potentials
of electrons and holes, while Q_f is assumed to be constant:

$$Q_{\text{Si}}(\Psi_s, \Phi_n, \Phi_p) + Q_{\text{it}}(\Psi_s, \Phi_n, \Phi_p) + Q_f = 0. \tag{3.20}$$

For the approximation of flat quasi-Fermi levels in the space-charge region, the
analytical integration of the one-dimensional Poisson equation provides the re-
lationship between the electric field strength and the potential $\Psi(x)$. Using the
Gaussian law, the total charge Q_{Si} induced in the silicon can then be calculated as
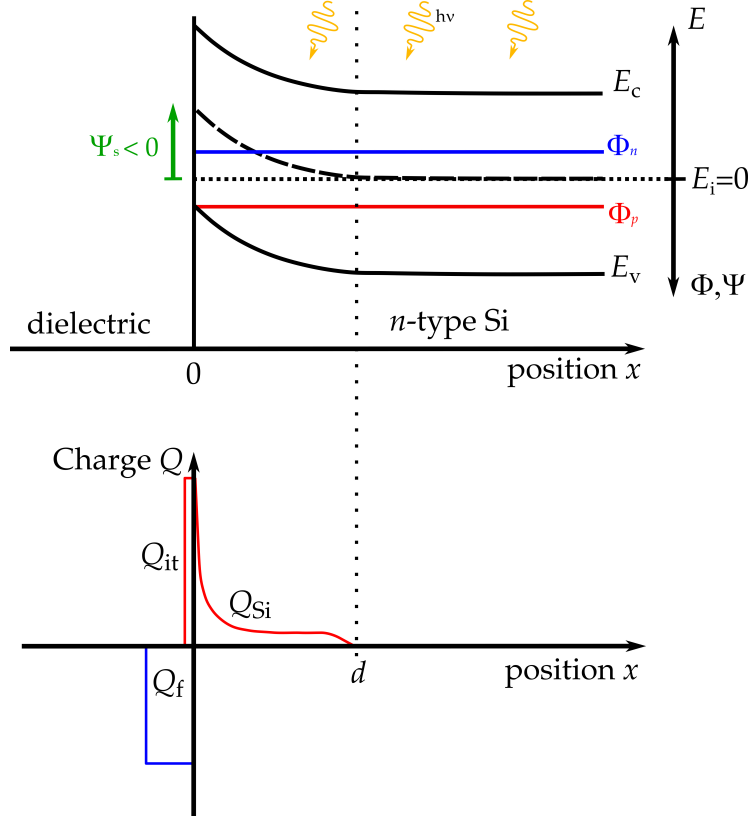
Figure 3.8: Energy band diagram of the physical situation of the band bending at the surface of an illuminated semiconductor at V_{oc} conditions, with the corresponding charge distribution of Q_f, Q_{Si}, and Q_{it}.

a function of Ψ_s using the expression[58]:

$$
Q_{Si} = \left[\frac{2kTn_i^2 \epsilon_0 \epsilon_{Si}}{q^2} \left[\exp\left(\frac{q(\Phi_p - \Psi_s)}{k_B T} \right) \right. \right.
$$
$$
- \exp\left(\frac{q\Phi_p}{k_B T} \right) + \exp\left(\frac{q(\Psi_s - \Phi_n)}{k_B T} \right) \tag{3.21}
$$
$$
\left. \left. - \exp\left(\frac{-q\Phi_n}{k_B T} \right) + \frac{q\Psi_s(N_A - N_D)}{n_i} \right] \right]^{-\frac{1}{2}}.
$$

U_s at a given injection level Δn is now calculated as described below. First, using Equation (3.12), the quasi-Fermi potentials Φ_n and Φ_p are calculated. In the next step, the iterative procedure by Girisch et al.[59] determines the surface potential Ψ_s. For this purpose, a starting value for Ψ_s is assumed and using Equations (3.20) and (3.21), the charge densities Q_{Si} and Q_{it} are determined. Then it is verified whether the sum of the charges $Q_{Si} + Q_{it} + Q_f$ is smaller than a given limit value. If this is not the case, Ψ_s will be slightly varied and the sum of the

charges is calculated again. If the sum is below the specified limit, the selected Ψ_s is used for the further calculations. Now, using Equations (3.13) and (3.14), the electron and hole concentrations n_s and p_s at the interface are calculated. Using Equation (3.17), the surface recombination rate U_s at a given band bending Ψ_s within the surface charge space region is obtained. With the surface recombination rate U_s, the effective surface recombination velocity S_{eff} can be determined by using Equation (3.19). S_{eff} values are shown in Figure 3.9 in dependence of Q_f for different Δn values and Figure 3.10 shows S_{eff} as a function of Δn for different Q_f values. S_{eff} increases with increasing Q_f and reaches a maximum at
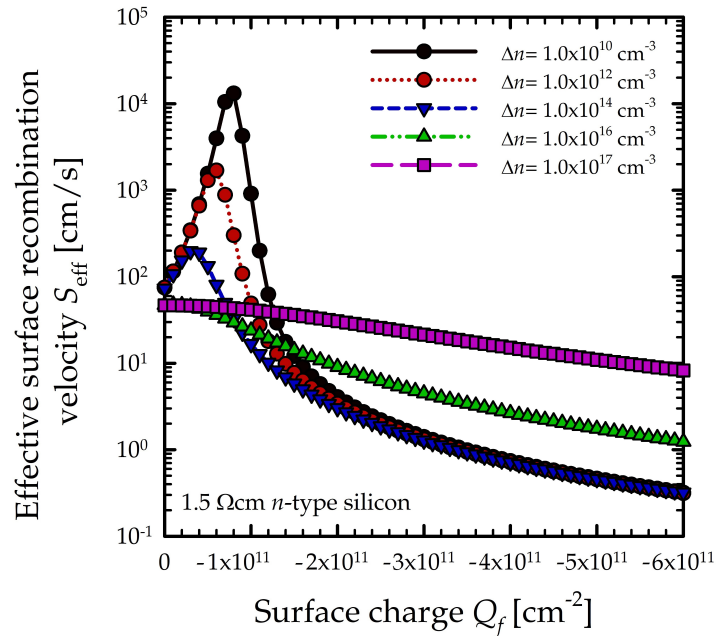

Figure 3.9: Calculated values for the effective surface recombination velocity S_{eff} as a function of the negative surface charge Q_f of an *n*-type silicon wafer with doping concentration of $N_D = 3.2 \times 10^{15}\,\text{cm}^{-3}$.

$Q_f = -1.0 \times 10^{11}\,\text{cm}^{-2}$ for a fixed Δn value of $1.0 \times 10^{10}\,\text{cm}^{-3}$, and decreases again to higher Q_f values. While under flat band conditions the surface recombination is mainly determined by the capture of the minorities (holes in *n*-type silicon) in interface states, with increasing Q_f the concentration of electrons in *n*-type silicon at the surface is slightly decreased (depletion) and the concentration of the minorities increases. Since the minorities determine the recombination process, S_{eff} increases with increasing Q_f. As Q_f increases, the density of the electrons at the interface decreases and the density of the holes increases further, until the surface is in inversion. This results in the decrease of S_{eff} with increasing Q_f. Figure 3.10 shows for $Q_f = -3.0 \times 10^{10}\,\text{cm}^{-2}$ an increase in S_{eff} for low injection densities (yel-
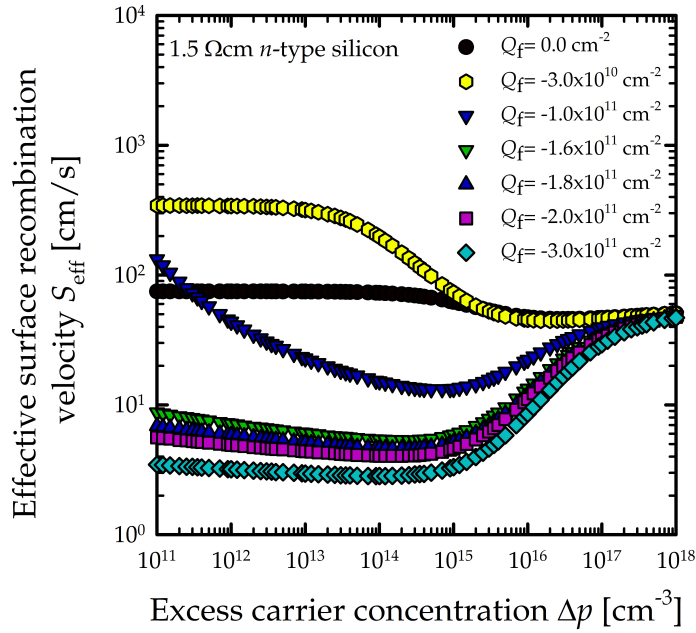
Figure 3.10: Calculated values for the effective surface recombination velocity S_{eff} as a function of the excess carrier concentration of an *n*-type silicon wafer with doping concentration of $N_D = 3.2 \times 10^{15}$ cm^{-3}.

low hexagons) compared to the case without band bending (black circles). With increasing negative Q_f values, S_{eff} decreases for low Δn values. In the case of high injection, a convergence of the curves is observed, which is a consequence of the decreasing band bending due to a strongly increased electron density at the edge of the space charge region.

3.4 Photoconductance-Based Carrier Lifetime Measurements

To estimate the passivation quality of the PEDOT:PSS/silicon junction, it is necessary to measure the carrier lifetime in the silicon wafer. A measurement method to determine the carrier lifetime is based on the photoconductance decay (PCD) method[61]. A lifetime tester (WCT-120, Sinton Instruments) is used to measure the carrier lifetime. A lifetime sample is thereby inductively coupled to a coil, which is part of an rf-bridge circuit. The conductance σ of the measured silicon wafer is a quadratic function of the output voltage V of the rf-bridge circuit. With the measured output voltage V of the rf-bridge circuit and the known quadratic function of $\sigma(V)$, the conductivity σ of any silicon sample can be determined. For

a measurement the sample is illuminated by a flash lamp, which creates excess charge carriers Δn in the sample. The excess charge carriers increase the conductance of the sample, which is monitored by the output voltage of the rf-bridge circuit. The experimental configuration is shown schematically in Figure 3.11. The conductivity σ of a silicon wafer is the sum of the basic conductivity σ_{Si} and
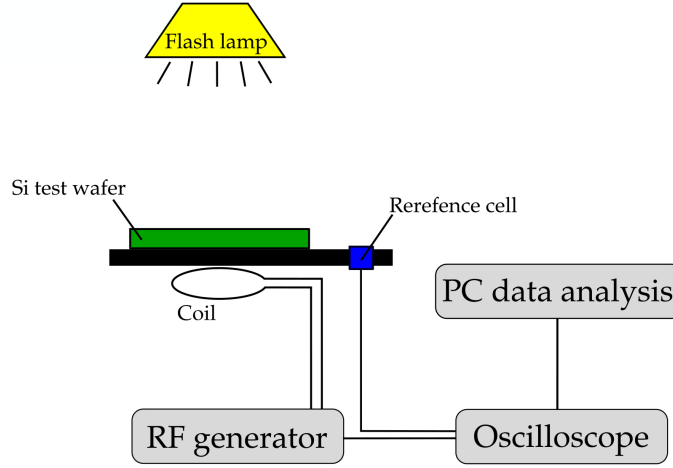

Figure 3.11: Experimental configuration for a photoconductance-based lifetime measurement. Charge carriers are generated optically by means of a flash lamp and the photoconductance is monitored inductively.

the photoconductivity $\Delta\sigma$:

$$\sigma = \sigma_{Si} + \Delta\sigma. \tag{3.22}$$

An oscilloscope is used to record the voltage of the rf-bridge circuit and thus the conductivity as a function of time. The light intensity is determined by means of a reference cell where the linear relationship between the measured short-circuit current density J_{sc} and light intensity is known. In general, the conductance of a silicon wafer is dependent on the charge carrier concentration and the charge carrier mobility:

$$\sigma = q \int_0^W (n\mu_n + p\mu_p) \, dx, \tag{3.23}$$

where q is the elementary charge, W is the thickness of the silicon wafer, n and p are the electron and hole concentrations and μ_n and μ_p are the electron and hole mobilities. The charge carrier mobilities depend on the charge carrier densities at the position x, and the charge carrier densities depend on the position x within the silicon wafer. Assuming that the photogenerated charge carriers Δn are homogeneously distributed in the sample, the photoconductance $\Delta\sigma$ is given

by:

$$\Delta\sigma \approx qW(\mu_n + \mu_p)\Delta n\,. \tag{3.24}$$

Since the illumination intensity of the sample is measured by a reference cell as a function of time, the generation rate $G(t)$ is determined from the short-circuit current I_{sc} of the reference solar cell:

$$G(t) = \frac{I_{sc}}{qW}D\,, \tag{3.25}$$

where D is a factor that corrects differences of the reflectance and transmission between the reference cell and the test sample. The light coupling into the sample, which is dependent on anti-reflex coatings or texturing of the Si surface, must be taken into account. With the time-dependent excess charge carrier concentration $\Delta n(t)$ and the generation rate $G(t)$ the charge carrier lifetime τ is calculated and the continuity equation with the recombination rate $R(t)$ and the divergence of the current density $\vec{\nabla}\vec{J}$ in this particular case reaches:

$$\frac{\partial \Delta n}{\partial t} = G(t) - R(t) + \frac{1}{q}\vec{\nabla}\vec{J}. \tag{3.26}$$

However, since the photogeneration and thus also the charge carrier concentration is very homogeneous, the last term can be neglected. The recombination rate can also be written as $R = \Delta n/\tau$. This can be used to formulate an equation for τ[62]:

$$\tau = \frac{\Delta n}{G - \frac{\partial \Delta n}{\partial t}}\,. \tag{3.27}$$

There are two different measuring modes depending on the time length of the excitation flash. If a light flash with a decay time in the range of milliseconds, which is very long compared to the decay time of Δn, quasi-steady-state (QSS) conditions are present in the sample. With $\frac{\partial \Delta n}{\partial t} \approx 0$, this results in combination with Equation (3.27) for the effective lifetime in:

$$\tau = \frac{\Delta n}{G}\,, \tag{3.28}$$

for the Quasi-steady-state photoconductance (QSSPC) measurement. If a very short excitation flash, much shorter than the samples carrier lifetime τ, is used, transient conditions are present in the sample. As the lifetime τ of the excess carrier concentration Δn exceeds the decay time of the flash, the generation rate

G is zero after the flash. Equation (3.27) is then simplified to:

$$\tau = -\frac{\Delta n}{\frac{\partial \Delta n}{\partial t}}.$$

(3.29)

This method is named "Photoconductance Decay" (PCD) method and is normally applied to measure long lifetimes.

3.5 Depletion Region Modulation (DRM)

Measurements of the photoconductance versus the illumination intensity can be used to determine the effective lifetime τ_{eff} of Si wafers. It is well known that carrier trapping[63] may cause the measured apparent effective excess carrier lifetime τ_{app} to be larger than the actual lifetime τ_{eff}. However, overestimation of the actual carrier lifetime is not only caused by trapping, but also by the presence of a junction, which leads to a depletion region in the sample. Excess charge carriers may accumulate at the edge of the depletion region, reducing the width of the depletion region. The width of the depletion region decreases with increasing light intensity. This effect is also called Depletion Region Modulation (DRM). Under illumination, the presence of a depletion region within a sample leads to the appearance of additional excess carrier densities Δn_{DRM} in the sample in addition to the excess carrier concentration Δn. Since surfaces coated with PEDOT:PSS can lead to an accumulation of holes up to an inversion layer on *n*-type silicon[64], it may be possible to observe the DRM effect in the photoconductance based measured lifetime on silicon samples coated with PEDOT:PSS. A band diagram of the physical situation of the band bending at the surface of a semiconductor with a negative surface charge Q_{f} is shown schematically in Figure 3.12. If Δn and Δn_{DRM} are of the same order of magnitude, which may be the case in low injection at injection, the additional charge carriers Δn_{DRM} leads to an overestimation in the measured carrier lifetime[65, 66]. As already shown in Equation (3.24), the excess charge carrier concentration Δn in silicon is related to the change in photoconductivity $\Delta \sigma$. The change in photoconductivity is equal to the conductivity of silicon under illumination σ_{light} minus the conductivity without excess charge carrier concentration σ_{dark}, i.e. without illumination:

$$\Delta n = \frac{\sigma_{\text{light}} - \sigma_{\text{dark}}}{qW(\mu_n + \mu_p)}.$$
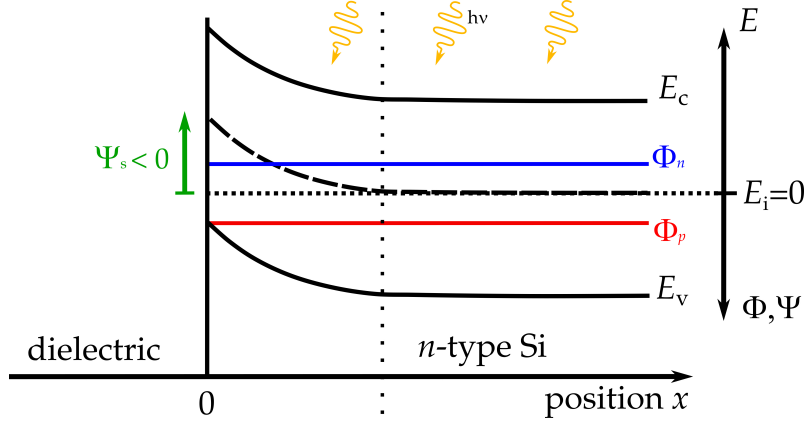
(3.30)

Figure 3.12: Energy band diagram of the physical situation of the band bending at the surface of illuminated n-type silicon at V_{oc} conditions with negative charge Q_f on the surface.

The conductivity is composed of the fraction of the conductivity without band bending σ_{fb} plus the conductivity induced by band bending σ_{bb}[65]:

$$\sigma = \sigma_{fb} + 2\sigma_{bb},\tag{3.31}$$

where σ_{fb} is given by:

$$\sigma_{fb} = qW\left[(n_0 + \Delta n)\mu_n + (p_0 + \Delta p)\mu_p\right].\tag{3.32}$$

The factor $2\sigma_{bb}$ is used here for symmetrical samples. σ_{bb} describes the deviation of the conductivity due to the band bending Ψ_s at the silicon surface and is described by solving the Poisson equation near the silicon surface[65, 66]:

$$\sigma_{bb} = \pm\sqrt{\frac{q^2\epsilon_0\epsilon_{Si}}{2k_BT}}\int_0^{\Psi_s}\frac{\left(n_0 + \Delta n\right)\left(\exp\left(\frac{q\Psi}{k_BT}\right) - 1\right)\mu_n}{\sqrt{F(\Psi,\Delta n)}}$$
$$+\frac{\left(p_0 + \Delta n\right)\left(\exp\left(\frac{-q\Psi}{k_BT}\right) - 1\right)\mu_p}{\sqrt{F(\Psi,\Delta n)}}\,d\Psi,\tag{3.33}$$

where $F(\Psi,\Delta n)$ is the auxiliary function given by:

$$F(\Psi,\Delta n) = \left(n_0 + \Delta n\right)\left(\exp\left(\frac{q\Psi}{k_BT}\right) - 1\right)$$
$$+\left(p_0 + \Delta n\right)\left(\exp\left(\frac{-q\Psi}{k_BT}\right) - 1\right) + \frac{q\Psi(N_A - N_D)}{k_BT}.\tag{3.34}$$

With the value for Ψ_s determined according to Girisch et al.[59] in Section 3.3.1 the conductivity σ_{bb} can be calculated as a function of the band bending Ψ_s at the silicon surface and the excess carrier concentration Δn in the bulk. The overall excess carrier concentration Δn_{total}, which includes the excess charge carriers due to the band bending at the silicon surface, can be calculated:

$$\Delta n_{total} = \Delta n_{fb} + 2\Delta n_{bb}, \tag{3.35}$$

where Δn_{fb} is the excess carrier concentration for flat band conditions given by:

$$\Delta n_{fb} = \frac{\sigma_{fb,light} - \sigma_{fb,dark}}{qW(\mu_n + \mu_p)}. \tag{3.36}$$

The excess carrier concentration as a function of the band bending Δn_{bb} at the surface is given by:

$$\Delta n_{bb} = \frac{\sigma_{bb,light}(\Psi_{s,light}) - \sigma_{bb,dark}(\Psi_{s,dark})}{qW(\mu_n + \mu_p)}. \tag{3.37}$$

In the case of conductivity in the dark $\Delta n = 0$. Using Equations (3.35), (3.36) and (3.37), the photoconductance based measured apparent lifetime τ_{app} as a function of the excess charge carrier concentration Δn can now numerically calculated for a silicon sample with induced band bending Ψ_s:

- For a silicon wafer, the electron and hole densities in equilibrium n_0, p_0, the thickness W, as well as the dopant concentrations N_A and N_D are known.

- The quasi-fermi potential $\Phi_n(\Delta n)$ and $\Phi_P(\Delta n)$ of electrons and holes is calculated according to Equation (3.12).

- A start parameter for the surface charge Q_f is assumed.

- In the next step, the iterative procedure of Girisch et al.[59] determines the surface potential Ψ_s. For this purpose a starting value for Ψ_s is assumed and using Equation (3.20) and (3.21) the charge density Q_{Si} is determined. Q_{it} is neglected, because in the case of PEDOT:PSS the Q_{it} of the native silicon oxide between PEDOT:PSS and silicon is an order of magnitude smaller than Q_f[60]. Next it is verified whether the sum of the charges $Q_{Si} + Q_f$ is smaller than a given limit value. If this is not the case, Ψ_s will be slightly varied and the sum of the charges is calculated again. If the sum is below the specified limit, the selected Ψ_s is used for the further calculation.

- Using Equation (3.13), the electron and hole concentrations n_s and p_s at the surfaces are calculated. Using Equation (3.17), the surface recombination rate U_s at a given band bending within the surface charge space region is obtained.

- From U_s the effective surface recombination velocity S_{eff} can now be determined using the Equation: $S_{eff} = U_s / \Delta n$, where Δn at the edge of the space charge region is used, and with $\tau_s = 2W / S_{eff}$ the lifetime is calculated.

- τ_{eff} is calculated according to Equation (3.10), where the intrinsic lifetime according to Veith-Wolf et al.[67] is used.

- The apparent lifetime τ_{app} and the calculated effective lifetime τ_{eff} are related with:

$$\tau_{app} = \frac{\Delta n_{total}}{\Delta n} \tau_{eff}. \tag{3.38}$$

Figure 3.13 shows calculated apparent lifetime curves τ_{app} in dependence of the excess carrier concentration Δn for different negative surface charges Q_f on the surface of an $1.5\,\Omega$cm n-type silicon wafer. Apparent lifetime curves for positive surfaces charges Q_f on n-type silicon are shown in Figure 3.14. The dashed lines
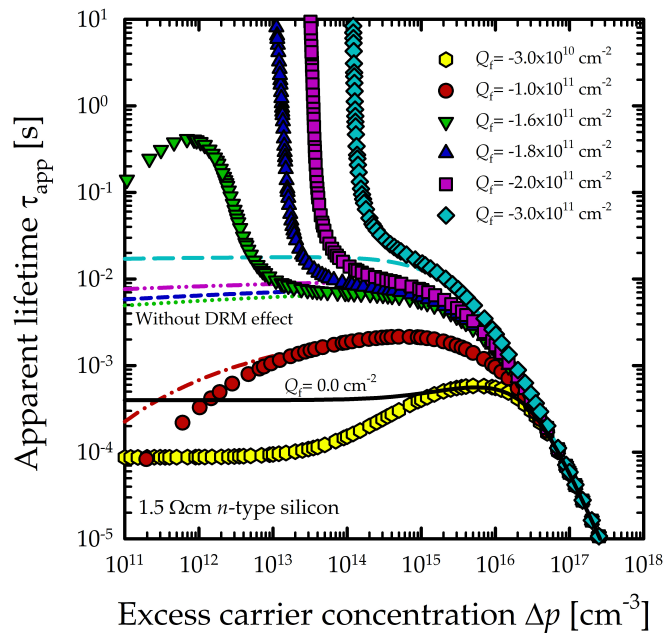
Figure 3.13: Example calculations of the apparent lifetime τ_{app} for negative Q_f values. The dashed lines indicate the model without DRM effect. The black solid line indicates the model with flat band conditions.
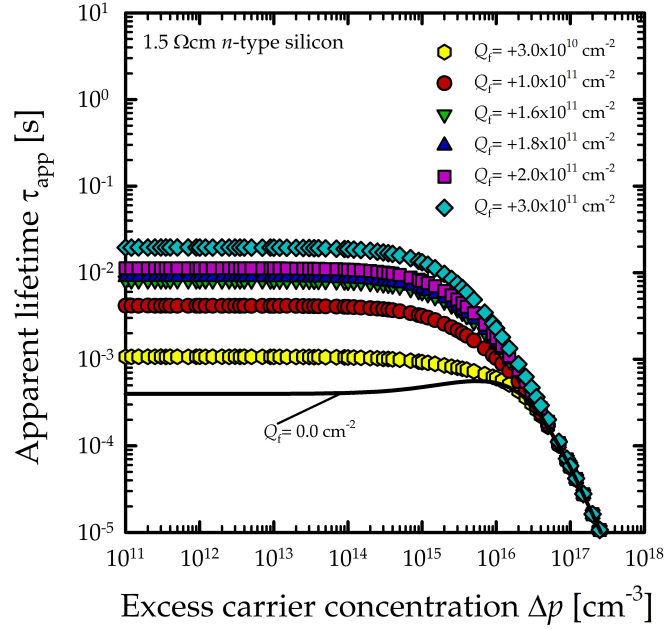
Figure 3.14: Example calculations of the apparent lifetime τ_{app} for positive Q_f values. The black solid line indicates the model with flat band conditions.

are calculations without the deviation due to the band bending at the surface, i.e. without the term σ_{bb} in Equation (3.35). We observe here the DRM effect for negative Q_f greater than $Q_f = -1.6 \times 10^{11} \, cm^{-2}$ as an increase in the apparent lifetime of τ_{app} for Δn values of $\sim 1.0 \times 10^{14} \, cm^{-3}$. For positive Q_f values, an increase of the apparent lifetime τ_{app} is observed with increasing Q_f for excess carrier concentrations below $1.0 \times 10^{16} \, cm^{-3}$. However, for positive Q_f values no DRM effect on *n*-type silicon is observed.

3.6 Specific Contact Resistance of the Ag/PEDOT:PSS/c-Si Junction

The electrical quality of ohmic contacts is usually characterized by the specific contact resistance ρ_c. However, if the contact resistance between a thin layer on a substrate and the substrate is to be characterized, it is not possible to separate the measured total resistance R_T into the specific contact resistance, the resistance due to the spreading of the current within the substrate and the remaining resistances R_0, which are determined by the conductivity of the layers, and the contact resistance of the metal contacts. However, it is possible to deter-

mine the specific contact resistance by using circular contact areas with different diameters[68, 69, 70, 71]. By using circular contact areas, the spreading resistance within the substrate can be approximated, if the thickness of the layer under investigation is much smaller than the diameter of the metal contact:

$$R_{\text{spread}} = \frac{\rho}{\pi d} \arctan\left(\frac{4W}{d}\right).$$

(3.39)

Here ρ is the resistivity of the silicon substrate, W is the thickness of the substrate and d is the diameter of the circular metal contact. The spreading resistance is then mainly determined by the resistance of the substrate and can be calculated. The contact resistance R_c is considered by the following expression:

$$R_c = \frac{4\rho_c}{\pi d^2},$$

(3.40)

where ρ_c is the specific contact resistance of the investigated junction. The residual resistances R_0 with respect to the resistance of the substrate or the contact resistance of the electrical contacts of the sample rear side are independent of the diameter of the circular metal contacts. The measured total resistance for each contact is thus composed of the spreading resistance R_{spread} in the substrate, the contact resistance R_c of the investigated junction and the residual resistances R_0:

$$R_T = \frac{\rho}{d\pi} \arctan\left(\frac{4W}{d}\right) + \frac{4\rho_c}{\pi d^2} + R_0.$$

(3.41)

If the conductivity of the substrate and the layer thickness are known, the specific contact resistivity ρ_c of the interface and the residual resistances R_0 can be determined. For this purpose, the measured total resistance is plotted against the

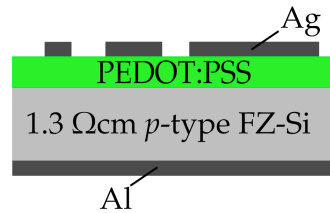Figure 3.15: Cross-section of a specific contact resistance sample

reciprocal contact diameter and the curve is fitted with equation 3.41. ρ_c and R_0 can then be determined from the fit. This method is commonly known as Cox-Strack method[68] and is applicable for different metals and substrates[72, 73]. In Figure 3.15 is a cross-section of a specific contact resistance sample shown. In this

thesis we use a silicon substrate with a resistivity of $1.3\,\Omega\text{cm}$ and a thickness of $300\,\mu\text{m}$. The thickness of the metal contacts on the front and rear side is $1\,\mu\text{m}$. The thickness of the PEDOT:PSS layer is in the order of $100\,\text{nm}$.

3.7 Optical Characterization

For the optical characterization of our samples we use a Cary 5000 (Varian) spectrophotometer. To use light of a narrow wavelength band for transmission and reflection experiments, the Cary 5000 spectrophotometer uses a Czerny-Turner monochromator. The design of the Czerny-Turner monochromator is shown in Figure 3.16. In the Czerny–Turner design[74], a broad-band illumination source

Entrance slit   Mirror

Diffraction grating

Mirror

Exit slit
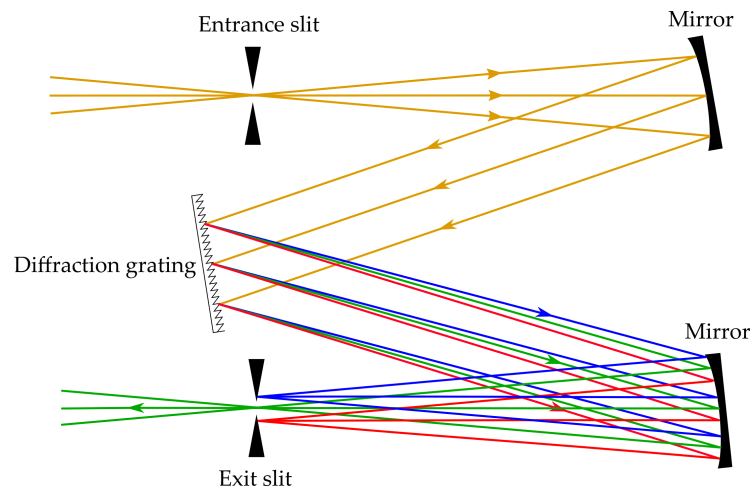
Figure 3.16: Schematic representation of a Czerny-Turner monochromator.

is focused at an entrance slit. A deuterium lamp (UV wavelength range) and a halogen tungsten lamp (for the visible and near-infrared wavelength range) are installed as light sources. The slit is placed at the effective focus of a curved mirror, which collimates the reflected light. The collimated light is diffracted from a grating and is collected by another mirror, which refocuses the light on an exit slit. The light is dispersed after the diffraction a the grating and with the exit slit the corresponding wavelength band can be selected by changing the diffraction angle of the grid. The Cary 5000 uses a so-called double Littrow monochromator. Compared to the Czerny-Turner monochromator, the double Littrow monochromator uses a single paraboloidal mirror for collimation and focusing. The double Littrow monochromator is a cascade of two monochromating systems. The wavelength band exiting through the exit slit of the first monochromator is further diffracted and selected in the second monochromator. This strongly increases resolution of the wavelength. With an integration sphere it is possible to determine

the diffuse reflectance of a sample. The integrating sphere is internally coated with Polytetrafluoroethylene (PTFE), which exhibits high near-infrared diffuse reflectance. In a transmission measurement, the sample is placed in front of the integrating sphere and the light transmitted through the sample unevenly in different directions is measured inside the integrating sphere as a function of the wavelength. For measuring the transmission of the sample, a reflection standard with known reflectance is used on the opposing side of the integration sphere. For reflection measurements the sample is clamped to the integrating sphere from the outside and the sample is illuminated from the inside of the integrating sphere. The advantage of using an integrating sphere for reflection measurements is that all backscattered light from the sample is detected. The cross section of an integration sphere and the measurement setup for transmission and reflectance measurements are shown schematically in Figure 3.17a and 3.17b.
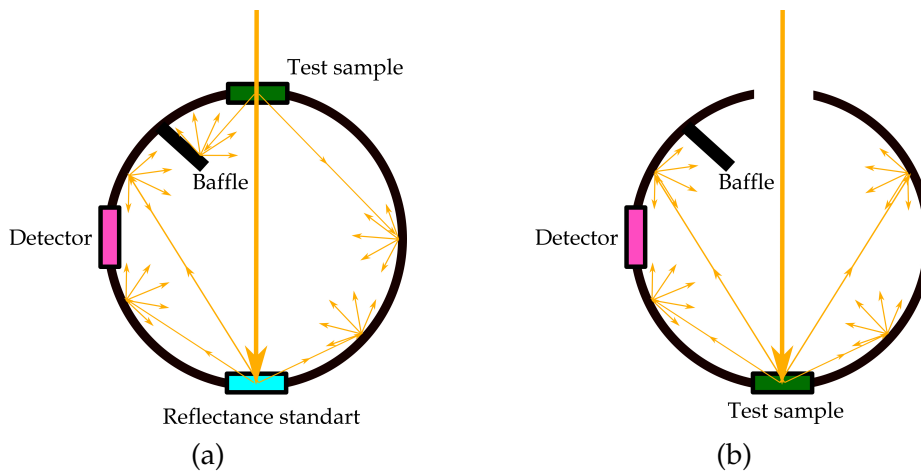
Figure 3.17: Cross section of an integration sphere with measurement setup for transmission (a) and reflectance (b) are shown.

4 Implementation of PEDOT:PSS into Silicon Solar Cells

4.1 Optimization of the Electrooptical Properties

In BackPEDOT solar cells, PEDOT:PSS is used as a hole-selective contact on the cell rear. The selectivity of PEDOT:PSS should be as high as possible, which means to provide good passivation properties for electrons and a good transport of holes. Furthermore, the optical transparency of a contact is of great importance. A selective contact should be as transparent as possible to maximize the short-circuit current of the solar cell. In this Chapter the specific contact resistance of the PEDOT:PSS/c-Si junction is examined as well as the process conditions for an optimal passivation of the silicon surface with PEDOT:PSS to determine the selectivity of PEDOT:PSS. The ideal PEDOT:PSS layer thickness to reduce parasitic absorption in PEDOT:PSS is also determined.

4.1.1 Thermal Annealing

The PEDOT:PSS layers for solar cell implementation are deposited by spin coating from an aqueous precursor dispersion with a PEDOT:PSS solid content of 2.4 weigth percent (wt.%). After the spin coating process, the thermal annealing of the PEDOT:PSS layer is of crucial importance for the resulting electrical properties[75]. The decisive quantities are the specific contact resistance ρ_{PEDOT} of the Ag/PEDOT:PSS/c-Si junction, as well as the passivation quality of the silicon surface with the PEDOT:PSS coating, which is described by the recombination current density parameter $J_{0.PEDOT}$. In order to assess the passivation quality of the PEDOT:PSS/c-Si junction, contactless lifetime samples are fabricated on 300 μm thick (100)-oriented p-type float-zone silicon (FZ-Si) wafers with a resistivity of 200 Ωcm. A cross-section of the lifetime samples is shown in Figure 4.1. The first step is the RCA cleaning of the wafer surfaces. RCA cleaning is a cleaning sequence developed by the Radio Corporation of America[76]. In the first
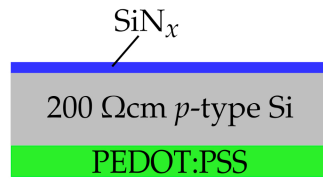
Figure 4.1: Cross-section of a lifetime sample.

step, the organic impurities and particles on the silicon surface are removed using an 80°C warm ammonia-hydrogen peroxide solution [5:1:1;$H_2O:NH_2:H_2O_2$]. During this 10 minute process a silicon oxide layer of a few nanometers is formed, which is removed in the next step by a solution of aqueous hydrofluoric acid (HF). The third step of the RCA cleaning sequence involves the removal of metallic and ionic contaminants. This step includes a 80°C warm hydrochloric acid-hydrogen peroxide solution [6:1:1 ; $H_2O:HCL:H_2O_2$]. In the fourth step, the silicon oxide formed in the third step is etched back. This again removes any remaining impurities from the silicon surface. After RCA cleaning, one wafer surface is passivated by a 100 nm thick plasma-enhanced-chemical-vapor-deposited (PECVD) SiN_x layer (Plasmalab 80 Plus, Oxford Instruments) with a refractive index n of $n = 2.4$ (at a wavelength of $\lambda = 633$ nm) at a deposition temperature of 400°C. After SiN_x deposition, the samples are dipped in 1% hydrofluoric acid (HF) for 60 seconds. Immediately after the HF dip, the PEDOT:PSS dispersion (CleviosTM, Heraeus Deutschland GmbH) is deposited by spin coating (WS-650Mz-8NPPB/UD3, Laurell Technologies). Subsequently, the PEDOT:PSS layer is annealed on a hotplate in ambient environment. Injection-dependent measurements of the effective carrier lifetime $\tau_{eff}(\Delta n)$ are performed using a Sinton Lifetime Tester (WCT-120, Sinton Instruments). The recombination current density parameter J_0, also sometimes denoted 'saturation current density', of each measured sample is extracted from the slope of the inverse lifetime $1/\tau_{eff}$ vs. the excess carrier concentration Δn curve[54] as described in Section 3.3. J_0 is extracted from the lifetime samples for different annealing temperatures and annealing durations of the PEDOT:PSS layer. For evaluation of the specific contact resistance ρ_{PEDOT} of the Ag/PEDOT:PSS/c-Si junction, p-type FZ-Si wafers with a resistivity of 1.3 Ωcm and a wafer thickness of 300 μm are used. After RCA-cleaning, the rear surface is full-area metallized by a 1 μm thick aluminum layer deposited by electron-beam evaporation (BAK 550, Balzers). After removing the native silicon oxide of the front surface using diluted HF, without undue delay PEDOT:PSS (CleviosTM, Heraeus Deutschland GmbH) is deposited by spin-coating (WS-650Mz-

8NPPB/UD3, Laurell Technologies). The coated PEDOT:PSS layer is annealed on a hotplate in ambient environment. A cross section of a specific contact resistance sample is shown in Figure 4.2a. A photograph of the circular silver contacts on top of the PEDOT:PSS layer is shown in Figure 4.2b. The diameter of the circular silver contacts range from 1 to 8 mm. Ten silver dots with a thickness of 1 μm
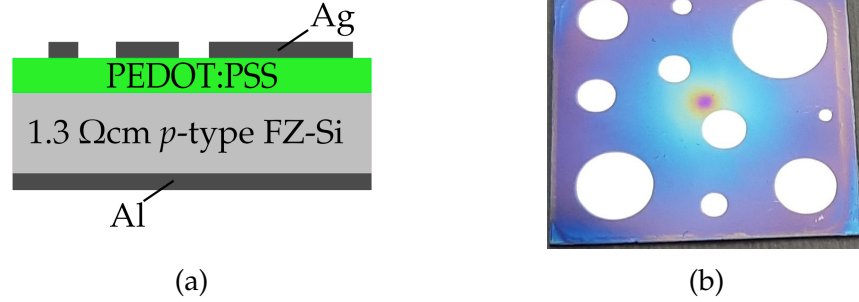

(a)   (b)

Figure 4.2: (a) Cross-section of a specific contact resistance sample. (b) Photo-
graph of a spin coated PEDOT:PSS layer on a silicon substrate with
evaporated circular silver top contacts.

and different diameters, ranging from 1 to 8 mm, are electron-beam-evaporated (BAK 550, Balzers) on top of the PEDOT:PSS layer through a shadow mask. For each single front contact dot, the current-voltage characteristic in the dark is measured using a commercial *I-V* tester (PV-Tools, Hamelin, Germany) at a temperature of 25°C. The specific contact resistance is extracted using the method of Cox and Strack, whereby the ρ_{PEDOT} values are obtained by fitting the curve of resistance versus reciprocal contact diameter[68] as described in Section 3.6. Figure 4.3a shows measured values for the recombination current density parameter $J_{0.\mathrm{PEDOT}}$ as a function of the annealing temperature ϑ. $J_{0.\mathrm{PEDOT}}$ was extracted from the measured overall J_0 values by subtraction of the $J_{0.\mathrm{SiN}}$ value of the SiN$_x$-passivated wafer surface. $J_{0.\mathrm{SiN}}$ was determined on both-sides-SiN$_x$-passivated wafers with a median value of $(16 \pm 5)\,\mathrm{fA/cm^2}$. Each data point represents the mean value of two samples equally processed. The error bars indicate the deviation from the mean value. With increasing annealing temperature, we observe a broad minimum of the $J_{0.\mathrm{PEDOT}}$ values for annealing temperature between 160 to 225°C. The best achieved $J_{0.\mathrm{PEDOT}}$ value is $J_{0.\mathrm{PEDOT}} = 60.0 \pm 2.0\,\mathrm{fA/cm^2}$ for an annealing temperature of 170°C. For temperatures above 220°C, the $J_{0.\mathrm{PEDOT}}$ values increase again. Therefore, PEDOT:PSS achieves the best passivation quality for annealing temperatures between 160 and 225°C. At higher temperatures, the passivation effect deteriorates due to the thermal instability of PEDOT:PSS at increased temperatures[8]. In any case, annealing temperatures higher than 100°C have to be applied in order to drive out the remaining water contained in the spin-

coated PEDOT:PSS layer to achieve a sufficient passivation effect[8]. Not only the

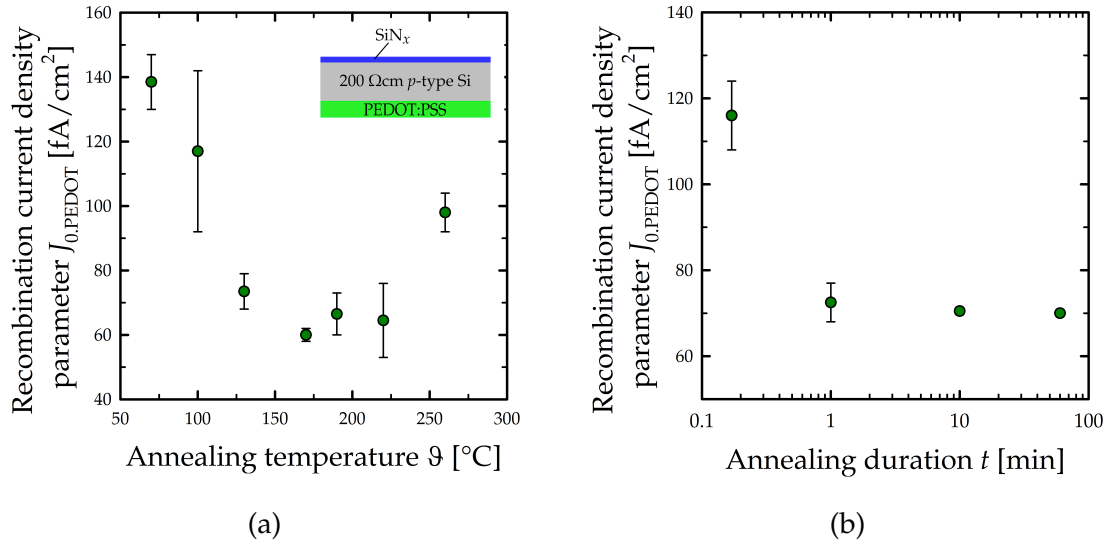(a)   (b)

Figure 4.3: (a) Recombination current density parameter $J_{0.\text{PEDOT}}$ for different PE-DOT:PSS annealing temperatures ϑ. The annealing duration is $t=10$ minutes for all samples. (b) $J_{0.\text{PEDOT}}$ for different PEDOT:PSS annealing durations t. The annealing temperature is $\vartheta=130°C$ for all samples. PEDOT:PSS is applied at a spin coating speed of $\omega = 1500\,\text{rpm}$.

choice of the optimal annealing temperature is important for a good passivation of the silicon surface with PEDOT:PSS, but also the duration of the annealing step plays a role. Figure 4.3b shows $J_{0.\text{PEDOT}}$ values in dependence of different annealing durations t. Each data point is the mean value of two equally processed samples. The error bars are calculated from the deviations of the mean values. For an annealing duration of 10 s at an annealing temperature of 130°C, which corresponds to the period, until a solid film is formed on the silicon surface, an average $J_{0.\text{PEDOT}}$ value of $116 \pm 8\,\text{fA/cm}^2$ is measured. If the annealing duration is increased to 1 min, a reduction of the $J_{0.\text{PEDOT}}$ to a value of $72.5 \pm 4.5\,\text{fA/cm}^2$ is measured. Increasing the annealing duration to 10 min does not lead to any further decrease of $J_{0.\text{PEDOT}}$. To achieve an acceptable passivation of silicon surfaces with PEDOT:PSS, an annealing duration of at least 1 min at 130°C degrees is required. Figure 4.4a shows the specific contact resistance ρ_{PEDOT} of the PEDOT:PSS/Si/Ag junction for different annealing durations at different annealing temperatures. Each data point is the mean value of two equally processed samples. The error bars are calculated from the deviations of the mean values. For an annealing duration of 130°C, the lowest value for the specific contact resistance is reached with $\rho_{\text{PEDOT}} = 22.2 \pm 4.1\,\text{m}\Omega\text{cm}^2$. For temperatures higher than 130°C, ρ_{PEDOT} increases up $430 \pm 96\,\text{m}\Omega\text{cm}^2$ for an annealing temperature
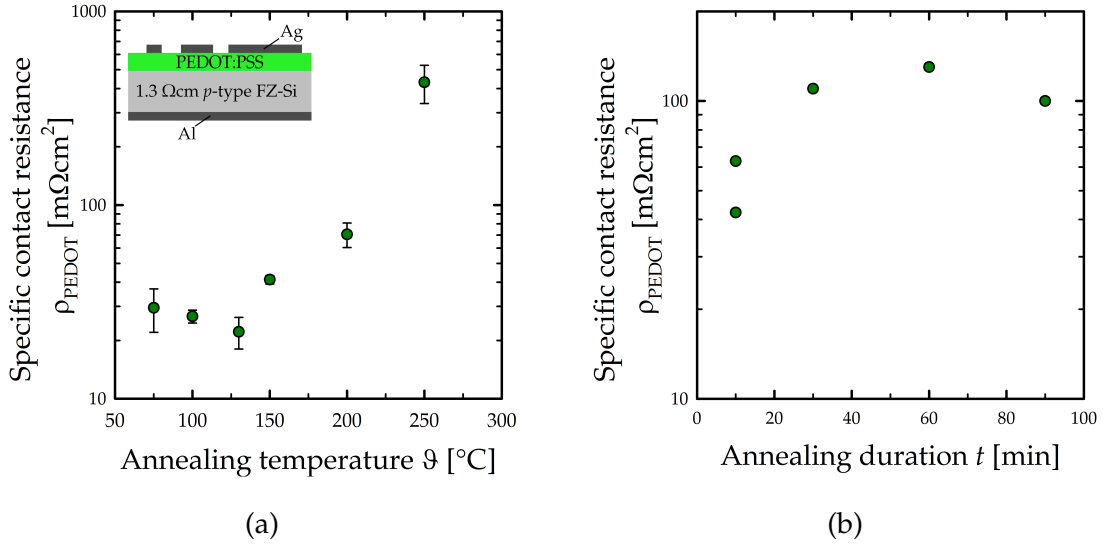
(a)   (b)

Figure 4.4: (a) Specific contact resistance ρ_{PEDOT} of the PEDOT:PSS/Si/Ag junction for different PEDOT:PSS annealing temperatures ϑ. (b) ρ_{PEDOT} for different PEDOT:PSS annealing durations t. The annealing temperature is $\vartheta=130°C$ for all samples. PEDOT:PSS is deposited at a spin coating speed of $\omega=5000\,rpm$.

of 250°C. The deterioration of ρ_{PEDOT} at high temperatures can be attributed to the thermal instability of PEDOT:PSS[8] for temperatures higher than 200°C. Figure 4.4b shows ρ_{PEDOT} for annealing durations between 10 and 90 min at a fixed annealing temperature of 130°C. For an annealing duration of 10 min ρ_{PEDOT} amounts to $42.2 \pm 1.8\,m\Omega cm^2$. If the annealing duration is increased, ρ_{PEDOT} increases to approximately $\rho_{PEDOT} \approx 120.0\,m\Omega cm^2$ for annealing durations longer 10 min. To optimize the passivation of the silicon surface as well as to minimize the specific contact resistivity of the PEDOT:PSS/Si/Ag junction we apply an annealing duration of of 10 min at 130°C. The annealing temperature of 130°C is chosen such that ρ_{PEDOT} is minimized. With the values of the specific contact resistance of the Ag/PEDOT:PSS/c-Si junction extracted by the Cox and Strack method in Figure 4.4a, and the $J_{0.PEDOT}$ values of the PEDOT:PSS/c-Si junction in Figure 4.3a, the selectivity of PEDOT:PSS can be calculated using Equation (3.6). The $J_{0.PEDOT}$ values are interpolated to the annealing temperatures investigated for the specific contact resistance samples. Figure 4.5 shows the calculated selectivity S_{10} in dependence of the annealing temperature ϑ. We observe here an increase in the selectivity with increasing annealing temperature of up to 130°C. For higher annealing temperatures, the selectivity decreases again. We report here a maximum value of the selectivity for PEDOT:PSS of 13.2 for 10 min annealing at a temperature of 130°C.
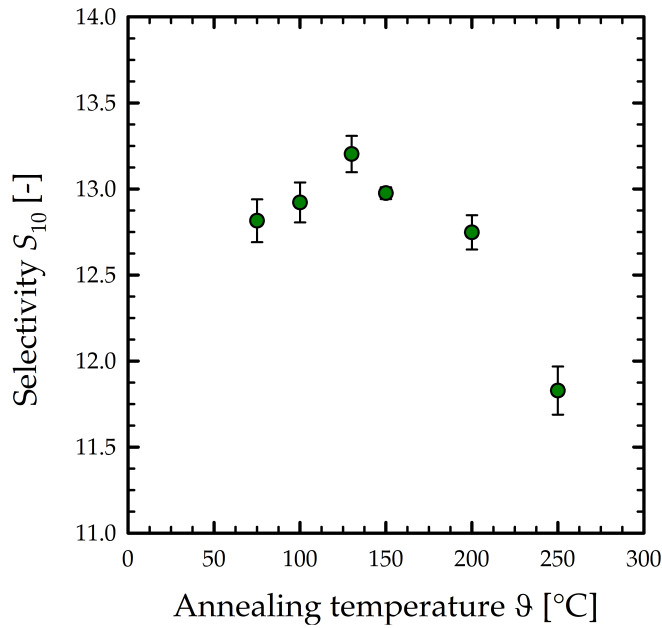
Figure 4.5: Selectivity S_{10} of deposited PEDOT:PSS on p-type FZ-Si for different annealing temperatures ϑ.

4.1.2 Impact of PEDOT:PSS Thickness

According to the results presented above, the standard annealing condition is chosen to 10 min at 130°C on a hotplate in ambient environment. It remains to be investigated which impact the thickness of the PEDOT:PSS layer has on the passivation of the silicon surface. Figure 4.6 shows the recombination current density parameter $J_{0.\text{PEDOT}}$ as a function of the PEDOT:PSS layer thickness for different solid contents in the PEDOT:PSS precursor dispersion. The PEDOT:PSS layer thickness shown in Figure 4.6 is the median value over a $2 \times 2\,\text{cm}^2$ area of a test sample. The error bars represent the deviation from the median value and are an indication of the inhomogeneity of the PEDOT:PSS layer over the entire sample. PEDOT:PSS thickness measurements were performed at 1 mm distant points over a length of 2 cm (20 data points) centered over the sample center using a profilometer (Dektak 150, Veeco). Each data point of $J_{0.\text{PEDOT}}$ represents the mean value of three samples equally processed for the PEDOT:PSS precursor dispersion with a solid content of 2.4 wt.%. For the precursor dispersions with reduced solid content, the mean value of $J_{0.\text{PEDOT}}$ was determined from two samples each. The error bars of $J_{0.\text{PEDOT}}$ indicate the deviation of the mean value. $J_{0.\text{PEDOT}}$ was extracted from the measured overall J_0 values by subtraction of the $J_{0.\text{SiN}}$ value of the SiN_x-passivated wafer surface. $J_{0.\text{SiN}}$ was determined on both-
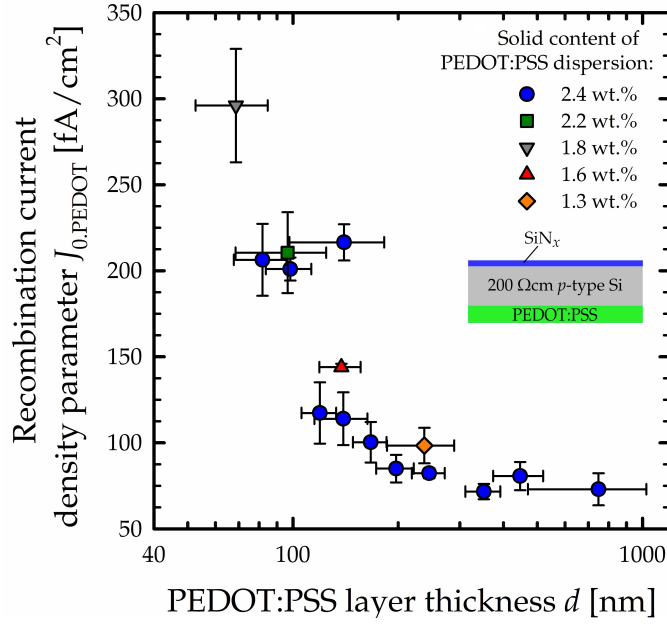
Figure 4.6: Recombination current density parameter $J_{0.\text{PEDOT}}$ as a function of the PEDOT:PSS layer thickness for different solid contents of the PEDOT:PSS precursor dispersion.

sides-SiN$_x$-passivated wafers with a median value of $(16 \pm 5)\,\text{fA}/\text{cm}^2$. For a solid content of the PEDOT:PSS precursor dispersion of 2.4 wt.%, the extracted value for the recombination current density parameter on a lifetime sample, where one silicon surface is passivated with PEDOT:PSS, is $J_{0.\text{PEDOT}} = (73.0 \pm 9.3)\,\text{fA}/\text{cm}^2$ for a PEDOT:PSS layer thickness of $d = (748 \pm 278)\,\text{nm}$. If the spin coating speed is increased, thinner PEDOT:PSS layers will result. For PEDOT:PSS layer thicknesses below 197 nm, a tendency to larger $J_{0.\text{PEDOT}}$ values is visible. In order to exclude that the increased spin coating speed for PEDOT:PSS layers with a thickness below 200 nm has a negative effect on the passivation effect, samples with reduced solid content (2.2 wt.%, 1.8 wt.%, 1.6 wt.% and 1.3 wt.%) of the PEDOT:PSS precursor dispersion and reduced spin coating speed were processed. For PEDOT:PSS film thicknesses below 200 nm, the measured $J_{0.\text{PEDOT}}$ values for the precursor dispersions with reduced solid content also increase up to values of over $200\,\text{fA}/\text{cm}^2$ for $J_{0.\text{PEDOT}}$, although these samples were prepared at lower spin coating speeds. It can therefore be excluded that the change in the solid content of the PEDOT:PSS precursor dispersion has an effect on the passivation of silicon surfaces with PEDOT:PSS. Up to now, only the passivation effect of PEDOT:PSS on planar silicon surfaces was investigated in this thesis. However, the deposition of PEDOT:PSS on random-pyramid-textured silicon surfaces is also

41

potentially relevant, e.g. if the PEDOT:PSS is deposited on the cell front[77]. It is important that the texture is homogeneous covered with PEDOT:PSS down to the deepest points between the pyramids of the texture. Inadequate coating between the pyramids leads to a decrease in the short-circuit current density J_{sc} and the open-circuit voltage V_{oc}[78, 79] of solar cells with textured silicon surfaces. Post coating of phthalic acid ester is, for example, a possibility to achieve a conformal coating of PEDOT:PSS on textured Si-surface[80]. It is also possible to round the pyramid tips and valleys of the texture by isotropic etching of pyramid structured silicon in an aqueous solution with hydrofluoric acid and nitric acid[81]. The front
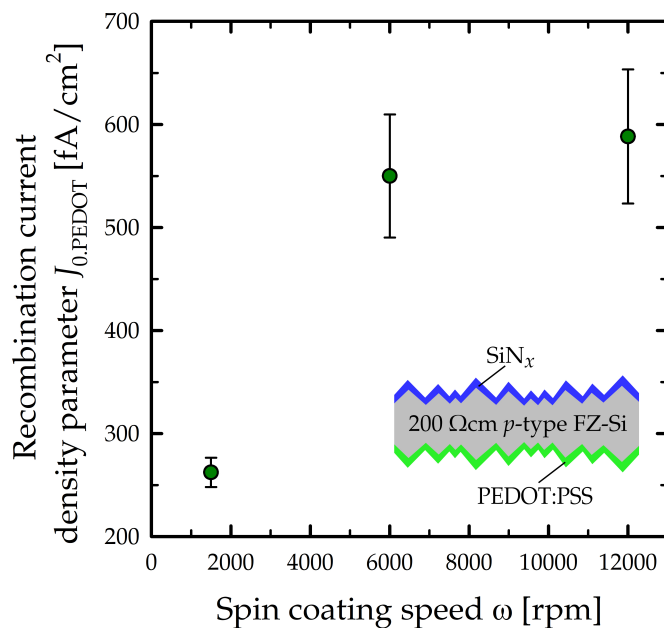
Figure 4.7: Recombination current density parameter $J_{0.PEDOT}$ as a function of the spin coating speed ω for PEDOT:PSS application on random-pyramid textured surfaces.

side of solar cells is usually textured by random pyramids to improve the light trapping and minimize reflection losses. For cost reasons, it is cheaper to simultaneously texture the front and rear of the silicon wafer. In case of a planar rear side of the wafer, it must be protected by a dielectric layer during the texturing process. The dielectric layer must then be removed for further processing. Therefore, it is important to examine the passivation properties of PEDOT:PSS on textured silicon surfaces. For the examination of the passivation properties of PEDOT:PSS on textured silicon surfaces, lifetime samples are used, which are textured by random pyramids on both sides. PEDOT:PSS is applied to the textured silicon surface by spin coating and is then annealed at a temper-

ature of 130°C for 10 min. Figure 4.7 shows median values of $J_{0.PEDOT}$, determined for three samples each. The error bars of $J_{0.PEDOT}$ indicate the deviations of the mean values. $J_{0.PEDOT}$ was extracted from the measured overall J_0 values by subtraction of the $J_{0.SiN}$ value of the textured SiN$_x$-passivated wafer surface. $J_{0.SiN}$ was determined on both-sides textured and SiN$_x$-passivated wafers with a median value of $(24 \pm 6)\,fA/cm^2$. The solid content of the PEDOT:PSS dispersion used here was 1.47 wt.%. For a spin coating speed of 1500 rpm, a measured recombination current density of $J_{0.PEDOT} = (262 \pm 14)\,fA/cm^2$ is obtained. If the spin coating speed is now increased to 12000 rpm, a median $J_{0.PEDOT}$ value of $(588 \pm 65)\,fA/cm^2$ is reached. The passivation effect of PEDOT:PSS on textured surfaces thus decreases with increasing spin coating speed or decreasing PEDOT:PSS layer thickness. The question arises whether a closed PEDOT:PSS film is formed on the textured silicon surface. To examine this, we carry out scanning electron microscopy (SEM) measurements, using a S4800, Hitachi SEM. Figure 4.8a and Figure 4.8b show SEM images of the PEDOT:PSS layer deposited at 1500 rpm and 12000 rpm. From SEM images the PEDOT:PSS thickness are esti-

| (a) | (b) |

Figure 4.8: Scanning electron microscopy (SEM) images of the textured silicon surface of the lifetime samples with PEDOT:PSS application at a spin coating speed of (a) 1500 rpm and (b) 12000 rpm.

mated on textured surfaces of 547 nm for a spin coating speed of 1500 rpm during the PEDOT:PSS application. For a spin coating speed of 12000 rpm, the thickness on the textured surface can only be roughly estimated with $d < 100$nm. This result is consistent with the passivation effect of PEDOT:PSS on planar silicon surfaces in Figure 4.6, because the passivation effect decreases with decreasing PEDOT:PSS layer thickness. However, what is noticeable in Figure 4.8a and Figure 4.8b is that the PEDOT:PSS layer deposited at 1500 rpm is not completely wetting the textured silicon surface. This can be seen from the pyramid tips, which
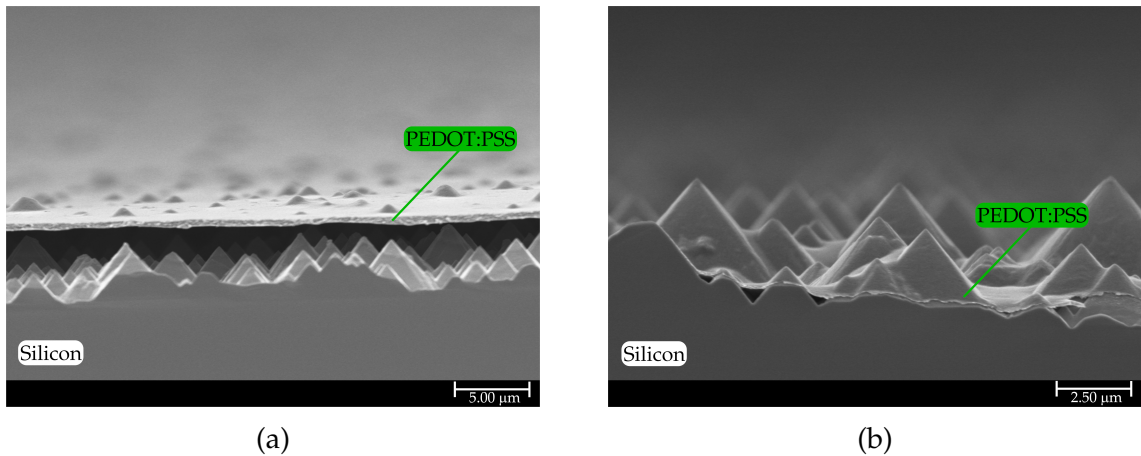
(a)   (b)
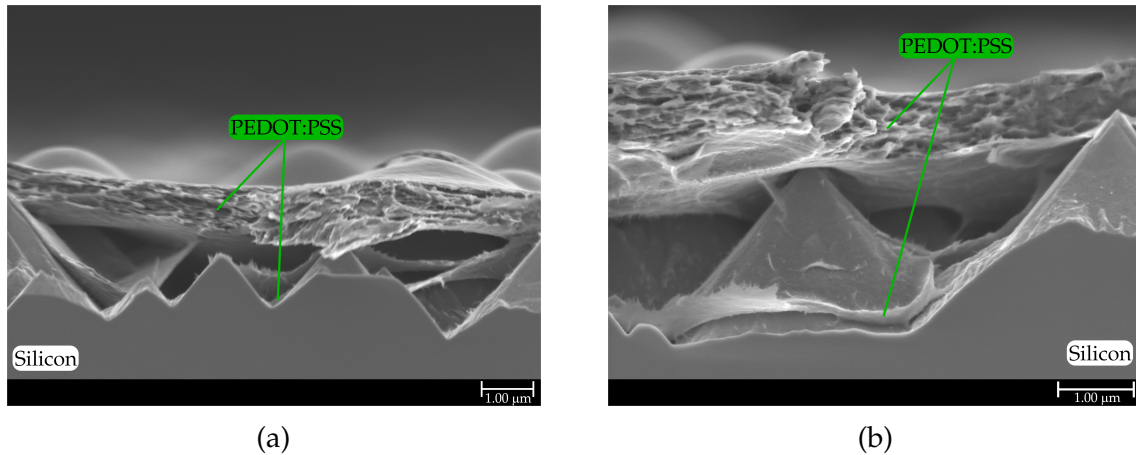
Figure 4.9: Scanning electron microscopy (SEM) images of the textured silicon surface of the lifetime samples with PEDOT:PSS application at a spin coating speed of 1500 rpm. A PEDOT:PSS dispersion with a particularly high solid content of 2.6 wt.% is used. Two different samples are shown.

are visible as an imprint in the PEDOT:PSS film. In Figure 4.8a the PEDOT:PSS rests only on the pyramid tips and is not in direct contact with the silicon surface. Since the samples are cleaved for examination in the scanning electron microscope and the PEDOT:PSS film is slightly stretchable, the PEDOT:PSS layer is slightly lifted from the surface during cleaving the sample. The depth of the imprints of the pyramid tip is a good measure of the original position of the PEDOT:PSS layer before the sample was cleaved. The fact, that the silicon surface is not wetted, cannot explain the better passivation effect in comparison to the sample from Figure 4.8b. Therefore, in the following, especially thick PEDOT:PSS layers are investigated on textured silicon surfaces. To obtain PEDOT:PSS layer thicknesses thicker than those shown in Figure 4.8a, a PEDOT:PSS dispersion with a particularly high solid content of 2.6 wt.% is used. The spin coating speed applied is 1500 rpm. The resulting PEDOT:PSS layers are shown in Figures 4.9a and 4.9b. It is noticeable that thinner organic layers are formed underneath the thick PEDOT:PSS layer, which extend into the valleys between the pyramids on the silicon surface. The silicon surface is thus covered with a very thin organic layer, although the thicker PEDOT:PSS layer only rests on the pyramid tips. It can be assumed that the thinner layer on the silicon surface is responsible for the passivation effect of PEDOT:PSS on textured surfaces. Figure 4.10a shows a SEM image of a PEDOT:PSS layer deposited on a textured silicon surface. A thinner organic is clearly visible, which is located in the valleys of the textured silicon surface. To evaluate whether this thin layer separates from the thicker
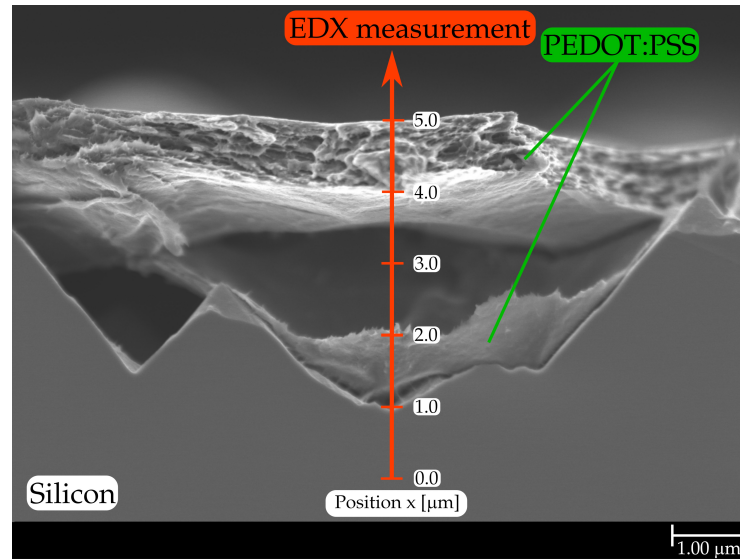
(a)
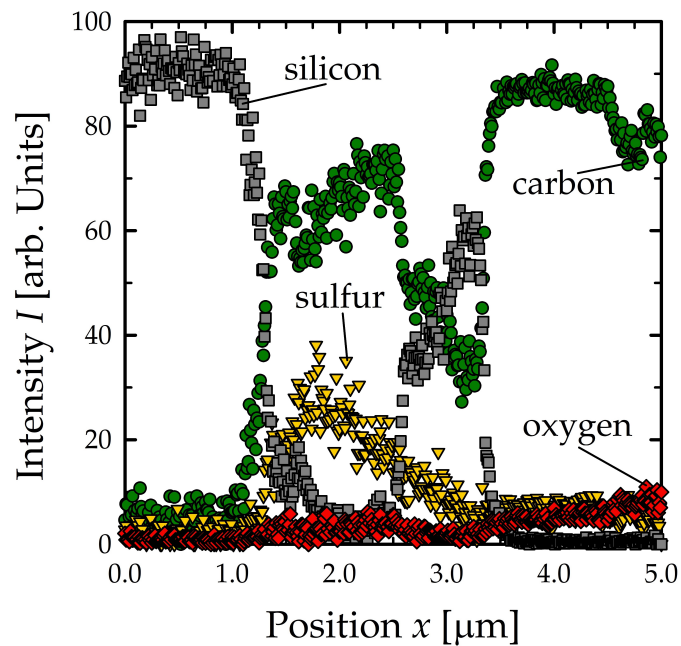
(b)

Figure 4.10: (a) Scanning electron microscopy image of the textured silicon surface of a lifetime sample passivated with PEDOT:PSS. The red line shows the area over which energy dispersive X-ray spectroscopy (EDX) measurement is performed. (b) Intensity I as a function of position x for the elements carbon (C), oxygen (O), silicon (Si) and sulfur (S) determined with a EDX measurement. The position x corresponds to the position on the red line in Figure 4.10a.

PEDOT:PSS layer, energy dispersive X-ray spectroscopy (EDX) measurements are performed. Using EDX measurements, the atomic composition of both PEDOT:PSS layers can be determined. The red line in Figure 4.10a shows the area over which the EDX measurement is performed. The result of the line scan is shown in Figure 4.10b. Shown is the intensity as a function of position x for the elements carbon (C), oxygen (O), silicon (Si) and sulfur (S). Position $x = 0.0\,\mu m$ corresponds to the bottom point of the line scan (the red line in Figure 4.10a) and position $x = 5.0\,\mu m$ the end of the line scan above the upper PEDOT:PSS layer. Between $x = 0.0\,\mu m$ and $x = 1.0\,\mu m$, approximately 90% silicon is detected. Carbon is only present with an offset of about 5%. Between $x = 1.0\,\mu m$ and $x = 3.0\,\mu m$, the signal of the near-surface organic layer is detected, whereby the signal of carbon increases from 5% to $\sim 70\%$. The sulfur content also increases up to 30%, but decreases with increasing x-position to 10% at a position of $x = 3.0\,\mu m$. Also, the oxygen content increases to $\sim 10\%$ between $x = 1.5\,\mu m$ and $x = 2.5\,\mu m$, whereas it is not detected at a position of $x < 1.0\,\mu m$. The signal of silicon reaches almost 0% at a position of $x = 2.0\,\mu m$. The behavior of the individual intensities in the range between $x = 1.0\,\mu m$ and $x = 3.0\,\mu m$ can be explained by the fact that the scanned area passes from the silicon substrate to the organic layer near the surface. This increases the signal of carbon as well as of sulfur and oxygen. Similarly, the signal of the silicon substrate decreases. Interesting is the scanned area between $x = 2.5\,\mu m$ and $x = 3.5\,\mu m$, where the signal of silicon increases from $\sim 5\%$ to $\sim 50\%$, but the signal of carbon decreases at the same rate. This can be explained by the fact that the thin organic layer coats the valleys between the silicon pyramids. While in the range between $x = 1.5\,\mu m$ and $x = 2.5\,\mu m$ both the front and the rear side of the thin organic layer are detected, at a position from $x = 2.5\,\mu m$ to $x = 3.5\,\mu m$ only the rear side of the thin layer is measured. This results in less organic material being measured, which explains the drop in carbon, sulfur and oxygen. The signal of silicon increases because the next silicon pyrmid is measured through the thin organic layer. For a scan position between $x = 3.5\,\mu m$ and $x = 5.0\,\mu m$, only the upper PEDOT:PSS layer is measured. The content of carbon increases to about 90%, while the signal of silicon disappears. Oxygen and sulfur are each detectable at about 10% in the upper PEDOT:PSS layer. On random-pyramid textured silicon surfaces, covered with PEDOT:PSS, we observe here for the first time a thin organic layer in the valleys between the pyramids of the silicon surface. The remarkable finding is that the organic layer near the surface shows an increased sulfur content compared to the thicker PEDOT:PSS layer on top. The oxygen content seems to be slightly reduced in the near-surface layer. It can be

therefore concluded, that the atomic compositions of the two organic layers are different. To verify this, the upper PEDOT:PSS layer and the thin layer near the silicon surface were measured again with a longer integration time. From the energy-dependent spectra, the composition in atomic percent for the two layers was determined. The carbon-to-oxygen and carbon-to-sulfur ratio of both layers can be determined. Figure 4.11 shows the carbon to sulfur ratio ([C:S]-ratio) (green bars), as well as the carbon to oxygen ratio ([C:O]-ratio) (blue bars) for the thin near-surface organic layer, as well as for the thicker PEDOT:PSS layer. The [C:S]-ratio is 5 for the near-surface organic layer, and 12.5 for the thicker upper PEDOT:PSS layer. This indicates that there is more sulphur in the near-surface layer than in the PEDOT:PSS layer on top. The [C:O]-ratio is 23 for the near-surface layer and 19 for the top layer. The near-surface layer thus has a slightly lower oxygen content and hence a different atomic composition than the thicker PEDOT:PSS layer. The different atomic composition suggests that the thin near-surface layer is responsible for the passivation effect of PEDOT:PSS on silicon surfaces and that an increased sulfur content has a positive impact on the surface passivation properties.
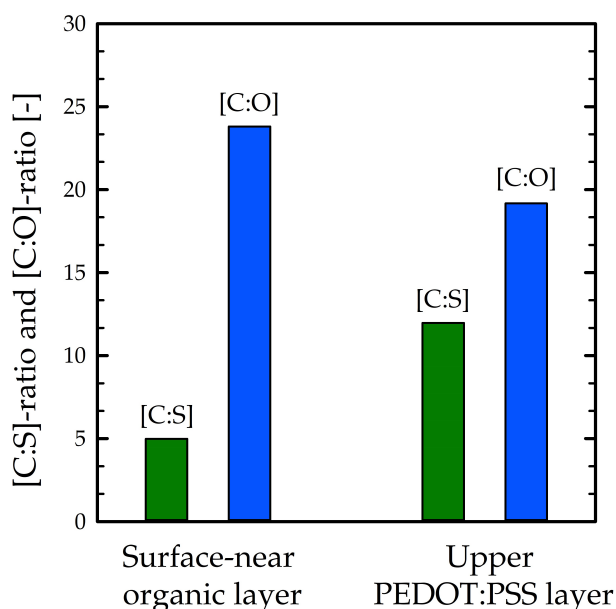

Figure 4.11: Carbon-to-sulfur ratio ([C:S]-ratio) (green bars), as well as the carbon-to-oxygen ratio ([C:O]-ratio) (blue bars) for the thin surface-near PEDOT:PSS layer and for the thicker PEDOT:PSS layer.

4.2 Optical Properties

After the determination of the optimal process parameters for the fabrication of a PEDOT:PSS layer with respect to the optimal passivation of the silicon surface and the lowest contact resistivity of the Ag/PEDOT:PSS/c-Si junction, it is now of interest to examine the optical properties in more detail in order to optimize the short-circuit current density J_{sc} on BackPEDOT solar cells. In order to determine the impact of the PEDOT:PSS layer thickness on the rear side of the solar cell on the cell short-circuit current density J_{sc}, test samples were prepared. We use 300 μm thick boron-doped p-type float zone silicon wafers with a resistivity of 1.3 Ωcm. A random-pyramid texture is formed on the front of the wafers while the rear is protected by a 100 nm plasma-enhanced-chemical-vapor-deposited SiN$_x$ (refractive index $n = 1.9$ at $\lambda = 633$ nm). Subsequently, the SiN$_x$ is removed using HF. The wafer is then cut into 2.5 x 2.5 cm^2 pieces by laser cutting and a 80 nm plasma-enhanced-chemical-vapor-deposited SiN$_x$ layer (Plasmalab 80 Plus, Oxford) (refractive index $n = 1.9$ at $\lambda = 633$ nm) is deposited on the random-pyramid-textured front side. On the rear side, the PEDOT:PSS dispersion (CleviosTM, Heraeus Deutschland GmbH) is deposited via spin-coating (WS-650Mz-8NPPB/UD3, Laurell) at 500 rpm for 10 seconds and then spin-dispersed for 30 seconds at a spin coating speed between 500 rpm and 12000 rpm. The coated PEDOT:PSS layer is annealed in ambient environment at 130°C for 10 min. Finally, the rear surface is metalized by a 1 μm thick silver layer deposited using e-beam evaporation (BAK 550, Balzers). The structure of the test samples is shown schematically in 4.12. The PEDOT:PSS layer thickness was adjusted by changing the rotational speed of the second step during the spin coating process. A higher rotational speed results in a thinner PEDOT:PSS layer. Measurements were performed with an UV-Vis-NIR spectrophotometer (Cary 5000, Varian) in the reflection mode using an integrating sphere. Figure 4.12 shows the measured hemispherical reflectance $R(\lambda)$ as a function of the wavelength for the test samples with different PEDOT:PSS layer thicknesses. The reflection spectra show a minimum at a wavelength of about 500 nm. This minimum is caused by the anti-reflection coating on the front side of the samples, which at this wavelength causes the conditions for destructive interference in the light beams reflected from the surface coated with the SiN$_x$ layers. The reason that the reflection increases to wavelengths shorter than 400 nm is due to the reflection of short-wavelength light at the surface of sample. At wavelengths between 500 nm and 1000 nm the reflection increases, which is due to the absorption coefficient of silicon, which decreases with increasing wavelength. Long-wavelength light thus penetrates
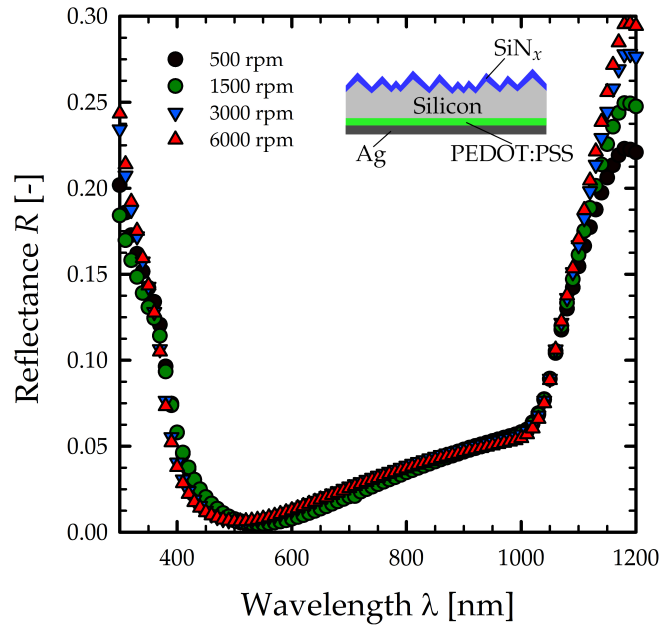
Figure 4.12: Hemispherical reflectance of test samples in which PEDOT:PSS was applied at different rotational speeds during the spin coating procedure. The PEDOT:PSS-covered rear side is fully metallized with a 1 μm thick silver layer deposited using e-beam evaporation.

deeper into the sample, while light of shorter wavelengths is absorbed relatively close to the surface. Since silicon has a band gap of 1.12 eV, which corresponds to a wavelength of 1107 nm, the probability, that light with energies smaller than the band gap energy is absorbed, is approaching zero. Long-wavelength, NIR-light with wavelengths longer than 1107 nm therefore passes through the solar cell very often until it exits through the surface. Therefore, the reflection in the wavelength range above 1000 nm increases strongly, which is called escape reflectance. A good indicator to assess the magnitude of parasitic absorption in the PEDOT:PSS layers is the escape reflectance in the long-wavelengths range. The PEDOT:PSS layer spin coated at 500 rpm shows the lowest escape reflectance. With decreasing PEDOT:PSS film thickness or increasing spin coating speed the PEDOT:PSS film becomes thinner and the escape reflectance increases. For a better comparability of the reflectance curves, only the reflectance R_{PEDOT} at a wavelength of 1200 nm is considered. Figure 4.13 shows the reflectance R_{PEDOT} at a wavelength of 1200 nm in dependence of the PEDOT:PSS layer thickness. The PEDOT:PSS layer thickness shown in Figure 4.13 is the median value over a $2 \times 2 \, \text{cm}^2$ area of a test sample. Figure 4.13 shows R_{PEDOT} as a function of the PEDOT:PSS thickness for a solid content in the PEDOT:PSS precursor dispersion of 2.4 wt.% (green circles) and 1.2 wt.% (green triangles). Layer thicknesses

Figure 4.13: Reflectance R_{PEDOT} at a wavelength of 1200 nm of test samples in dependence of the PEDOT:PSS layer thickness d. The PEDOT:PSS dispersion used has a solid content of 2.4 wt.% (green circles). To achieve PEDOT:PSS layers with a thickness of less than 77 nm the solid content was reduced to 1.2 wt.% (green triangles).

smaller than $d = 77$ nm are not possible to achieve with the PEDOT:PSS precursor dispersion due to the solid content of 2.4 wt.% in combination with the maximum possible spin coating speed of our spin coater of 12000 rpm. To achieve PEDOT:PSS layers with a thickness of less than $d = 77$ nm, the solid content of the PEDOT:PSS precursor dispersion was reduced to 1.2 wt.% by adding water. R_{PEDOT} decreases with increasing PEDOT:PSS layer thickness and saturates at a value of $R_{PEDOT} = 0.22$ for PEDOT:PSS layer thicknesses above > 1000 nm. In summary, with a PEDOT:PSS layer thickness of $d = (24 \pm 5)$ nm, a value for the reflectance at 1200 nm with $R_{PEDOT} = 0.39$ is achieved. This indicates that the thinnest possible PEDOT:PSS layer maximizes the escape reflectance and thus also the short-circuit current density of BackPEDOT solar cells. To further verify the impact of the PEDOT:PSS layer thickness, ray-tracing simulations are used to assess the impact of the PEDOT:PSS layer thickness on the solar cell rear on the short-circuit current density of the BackPEDOT solar cell. The simulations were performed using the software Sunrays[82, 83], developed by Brendel. The ray-tracing software Sunrays employs a Monte Carlo simulation. Each light ray is calculated according to the laws of geometrical optics, including wavelength-dependent, polarization-dependent and angle-dependent reflection and trans-

mission at each interface. For a periodic structure only the unit cell shown in Figure 4.15a needs to be considered. The unit cell consists of a cuboid silicon base with an edge length of 5 μm in x- and y-direction and an edge length of 300 μm in z-direction. 300 μm corresponds to the thickness of the silicon wafer. The cuboid possesses on the illuminated side a pyramid with 3.5 μm height, whose peak is exactly in the center of the ground plane. On the pyramid there is an anti-reflection coating of silicon nitride with a thickness of 80 nm and a refractive index of n=1.9 (at λ = 633 nm). On the opposite, planar side is a layer of 1 nm native silicon oxide, on top of which is a layer of PEDOT:PSS, whose thickness is varied in the simulation. On top of the PEDOT:PSS layer there is 1000 nm silver as back reflector. If a ray leaves the unit cell through a sidewall, the ray will re-enter at the symmetrical point on the opposite sidewall. In case of re-entry into the unit cell as well as when reaching an interface, the ray is randomized in the propagation direction. Sunrays uses the tabulated AM 1.5G[84] spectrum for the irradiance of the unit cell. Furthermore, Sunrays uses the wavelength-dependent refractive index $n(\lambda)$ and the wavelength-dependent extinction co-efficient $k(\lambda)$ of silicon[85], silicon nitride[85] and silver[85], and $n(\lambda)$ and $k(\lambda)$ values of PEDOT:PSS[13]. Figure 4.14 shows the reflectance R_{PEDOT} at a wavelength of 1200 nm of test samples in dependence of the PEDOT:PSS layer thickness in comparison to the simulated reflectance at a wavelength of 1200 nm. For PEDOT:PSS layer thicknesses above $d = 100$ nm the simulated reflectance R_{PEDOT} at a wavelength of 1200 nm shows a good agreement with the measured data. For PEDOT:PSS layer thicknesses less than $d = 40$ nm the simulation provides higher values for R_{PEDOT} compared to the measured values. In the simulation, PEDOT:PSS is assumed to be a perfectly homogeneous layer. This might be well approximated for thick PEDOT:PSS layers, but extremely thin PEDOT:PSS layers are optically more inhomogeneous. It is known that at the PEDOT:PSS/Si interface PSS is preferentially accumulated in the first few nm of the PEDOT:PSS layer[8]. In addition, if there is a different PEDOT:PSS ratio in thin PEDOT:PSS layers, the n and k values of PEDOT:PSS will also change, which will lead to a different optical thickness and this is not taken into account in the simulation. Figure 4.15a illustrates the simulated absorbed current density in silicon J_{Si} for different PEDOT:PSS layer thicknesses on the sample. For a PEDOT:PSS layer thickness of only $d = 10$ nm, the simulated absorbed current density in silicon provides a value of $J_{\mathrm{Si}} = (43.30 \pm 0.03)$ mA/cm^2. Witch increasing PEDOT:PSS thickness, the J_{Si} value decreases and saturates at (42.30 ± 0.03) mA/cm^2 for PEDOT:PSS thicknesses above 400 nm. Figure 4.15b shows the simulated parasitic absorbed cur-
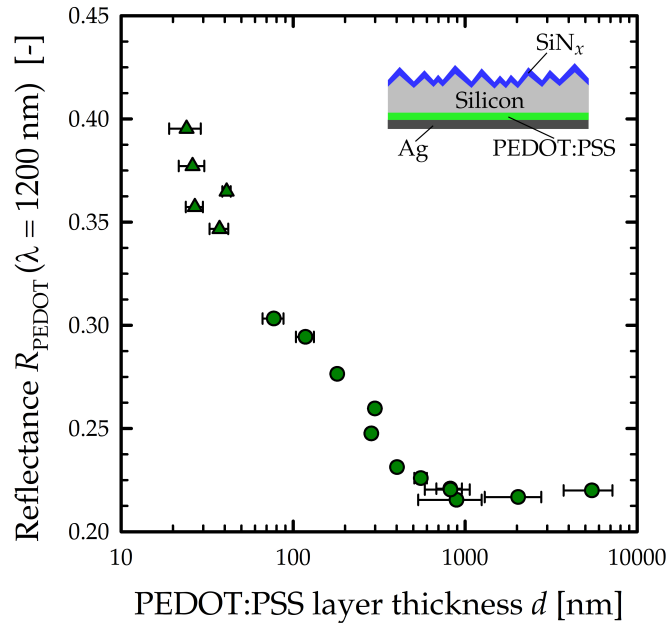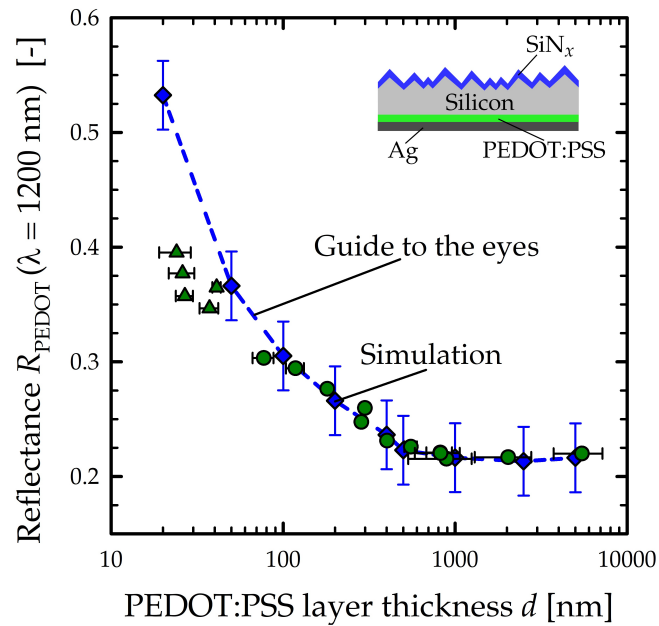
Figure 4.14: Reflectance R_{PEDOT} at a wavelength of 1200 nm of test samples in dependence of the PEDOT:PSS layer thickness d. The PEDOT:PSS dispersion used has a solid content of 2.4 wt.% (green circles) and 1.2 wt.% (green triangles). The blue diamonds show the simulated reflection at a wavelength of 1200 nm. The dashed blue line serves as a guide to the eyes.

rent density J_{PEDOT} in PEDOT:PSS in dependence of the PEDOT:PSS layer thickness on the sample. The simulated reflected current density J_{refl} is also shown in Figure 4.15b. The simulated J_{PEDOT} value is (0.50 ± 0.03) mA/cm^2 for a PEDOT:PSS thickness of $d = 10$ nm. With increasing PEDOT:PSS thickness, the value for J_{PEDOT} increases and saturates for PEDOT:PSS layer thicknesses above 300 nm at $J_{PEDOT} = (2.40 \pm 0.03)$ mA/cm^2. The simulated reflected current density J_{refl} indicates how much light is reflected at the front surface of the sample and how much light leaves the sample through the front surface after one or more passes through the sample. The simulated reflected current density decreases with increasing PEDOT:PSS thickness from a value of $J_{refl} = (2.48 \pm 0.03)$ mA/cm^2 for a PEDOT:PSS layer thickness of $d = 10$ nm to a value of $J_{refl} = (1.66 \pm 0.03)$ mA/cm^2 for a PEDOT:PSS layer thickness of $d = 400$ nm and saturates for thicker PEDOT:PSS layers. The behavior of the curves in Figure 4.15a and Figure 4.15b can be explained by the fact that PEDOT:PSS acts like a dielectric mirror[86, 87] on the rear side of the sample in combination with the metallized rear reflector. Since photons with wavelengths in the near-infrared range reach the rear of the solar cell due to the absorption behavior of silicon, the ratio of reflected and
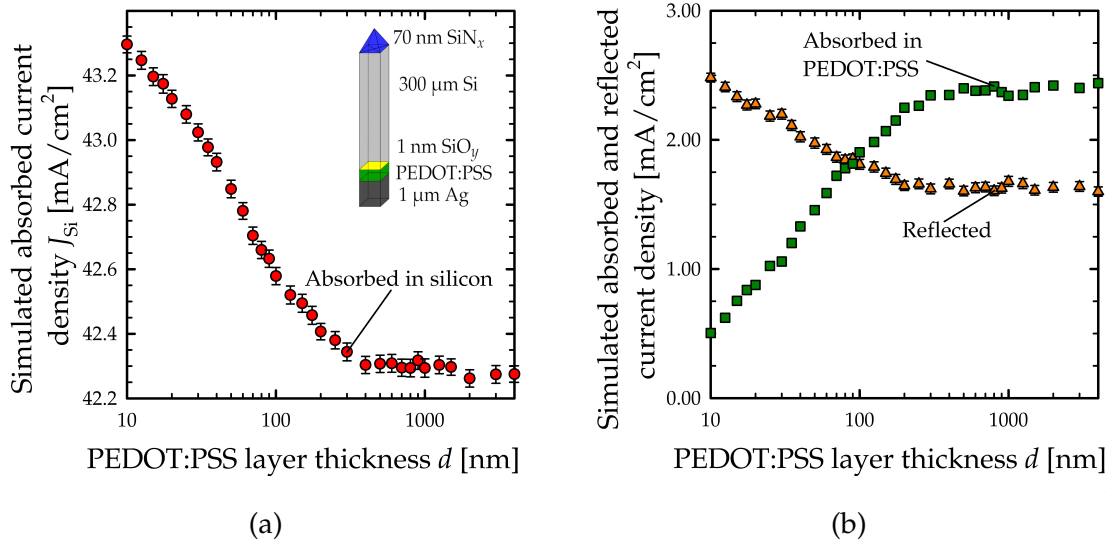
Figure 4.15: (a) Simulated Absorption in the silicon base of the unit cell J_{Si} (red circles) of a PEDOT:PSS/c-Si heterojunction solar cell in dependence of the PEDOT:PSS layer thickness d on the solar cell rear. (b) Simulated parasitic absorbed current density in PEDOT:PSS J_{PEDOT} (green squares) and the simulated reflected current density J_{refl} (orange triangles) in dependence of the PEDOT:PSS layer thickness d on the solar cell rear.

transmitted light at the Si/PEDOT:PSS/Ag junction plays a decisive role. For PEDOT:PSS layers thicker than $d = 400$ nm, all light that is transmitted through the Si/PEDOT:PSS junction is absorbed in the PEDOT:PSS layer and is therefore completely lost for the current generation in a solar cell. For PEDOT:PSS layers thinner than $d = 400$ nm not all near-infrared light is parasitically absorbed in PEDOT:PSS and a possibility of back reflection by the silver-metallized rear into the silicon base is possible. This is also shown by the fact that J_{refl} for PEDOT:PSS layer thicknesses thinner than $d = 400$ nm increases. To maximize the short-circuit current density of a BackPEDOT solar cell with PEDOT:PSS on the solar cell rear side, the thickness of the PEDOT:PSS layer should be as thin as possible.

4.3 Solar Cell Results

In order to successfully implement PEDOT:PSS in silicon solar cells on the solar cell rear (so called 'BackPEDOT solar cells'), the optimized process parameters for the fabrication of the PEDOT:PSS layer must be known. The annealing parameters for an optimal thermal annealing of the spin-coated PEDOT:PSS layer were determined in Section 4.2 of this Chapter. Thermal annealing for 10 min at 130°C on a hotplate in ambient environment is performed to improve the selectivity S_{10} of PEDOT:PSS. Our ray tracing simulations have shown a strong impact of the PEDOT:PSS layer thickness on the short-circuit current density J_{sc} of BackPEDOT solar cells. Therefore, J_{sc} can be improved by reducing the PEDOT:PSS thickness on the cell rear. However, for PEDOT:PSS layer thicknesses less than $d = 200$ nm the passivation quality of PEDOT:PSS deteriorates dramatically. As a consequence, the maximum values for J_{sc} will increase with increasing spin coating speed, but V_{oc} will decrease for thin PEDOT:PSS layers. Furthermore, we examine The series resistance R_s as well as the energy conversion efficiency η in dependence of the spin coating speed during the PEDOT:PSS application. The spin coating speed is varied to obtain different PEDOT:PSS layer thicknesses on the solar cell rear. The PEDOT:PSS film thickness for each spin coating speed is measured on test samples processed with the same parameters. The layer thickness is hereby the median value over a 2×2 cm^2 area of the test sample for each applied spin coating speed. Measurements were performed at 1 mm distant points over a length of 2 cm (20 data points) centered over the sample center using a profilometer (Dektak 150, Veeco). Different spin coating speeds

Table 4.1: Median PEDOT:PSS layer thickness *d* for different spin coating speeds ω during the PEDOT:PSS application.

Spin coating speed ω [rpm]	Median PEDOT:PSS layer thickness *d* [nm]
500 (3 samples)	1993 ± 160
1500 (21 samples)	555 ± 90
6000 (6 samples)	134 ± 10
12000 (17 samples)	64 ± 10

ω with different revolutions per minute (rpm) are used for the application of PEDOT:PSS. The determined PEDOT:PSS layer thicknesses for different spin coat-

ing speeds are summarized in Table 4.1. The deviation of the PEDOT:PSS layer thickness in Table 4.1 does not refer here to the inhomogeneity of the PEDOT:PSS layer thickness over the sample surface, but to the variation of the PEDOT:PSS layer thickness between equally processed samples. For each investigated spin coating speed during the PEDOT:PSS application a certain number of BackPE-DOT cells was fabricated. The cross-section of a BackPEDOT solar cell is shown schematically in Figure 4.16a. For the solar cell fabrication 300 µm thick 6″ (100)-

| (a) | (b) |
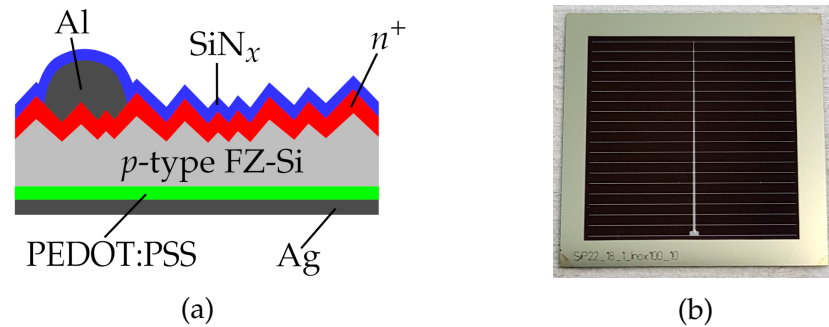
Figure 4.16: (a) Cross-section of a BackPEDOT solar cell. (b) Photograph of a BackPEDOT solar cell.

oriented p-type boron-doped float-zone silicon (FZ-Si) wafers with resistivities of 0.5 and 1.3 Ωcm are used. The first step in the solar cell manufacturing process is the RCA cleaning of the wafer. After RCA cleaning both surfaces are protected by a 200 nm thick dielectric SiO_2 layer, which is formed by high temperature oxidation in a quartz-tube furnace (TS 81004, Tempress). Alternatively, a plasma-enhanced chemical vapor deposited silicon nitride layer (PECVD) can also be used as a dielectric protective layer. Next, 2×2 cm^2 diffusion windows are opened by laser ablation (HyperRapid50, Coherent) on one wafer side. After one more RCA cleaning sequence, the silicon surface within the ablated windows is random-pyramid-textured using a KOH/isopropanol solution. Subsequently, an n$^+$ emitter with a sheet resistance in the range 92 -110 Ω/sq is formed by phosphorus in-diffusion in a quartz-tube furnace (TS 81004, Tempress) at 830°C in a POCl$_3$/O$_2$ atmosphere. The wafers are then laser-cut (CW Fiber Laser, IPG Photonics) into 2.49×2.49 cm^2 large samples, and after additional cleaning, the phosphorus silicate glass is removed in a 1% diluted hydrofluoric acid solution. An 0.24 nm thick AlO$_x$ tunneling layer is then deposited by means of plasma-assisted atomic layer deposition (FlexAL, Oxford Instruments) on the front surface. The AlO$_x$ tunneling layer provides a better passivation of the silicon surface underneath the front contacts[88] applied in the next step. An aluminum grid is deposited on the cell front through a nickel shadow mask by electron beam evapora-

tion (BAK 550, Balzers). The front surface is then coated by a surface-passivating PECVD SiN_x layer (Plasmalab 80 Plus, Oxford Instruments) with a refractive index $n = 2.4$ (at a wavelength of $\lambda = 633\,nm$) and a thickness of $6\,nm$. On top is a SiN_x anti-reflection coating with a refractive index $n = 1.9$ (at $\lambda = 633\,nm$) and a thickness of $75\,nm$ at a deposition temperature of $300°C$. Subsequently, the cells are annealed for $2\,min$ at $350°C$ in order to improve the front surface passivation and for contact formation[88]. Before depositing the PEDOT:PSS on the cell rear, the dielectric SiO_2 protection layer on the solar cell rear is removed using 40% HF. The PEDOT:PSS dispersion (CleviosTM, Heraeus Deutschland GmbH) is deposited by spin-coating (WS-650Mz-8NPPB/UD3, Laurell Technologies) and the resulting PEDOT:PSS layer is annealed in ambient environment. Finally, the rear surface is full-area metallized by a $1\,\mu m$ thick silver layer deposited using electron beam evaporation (BAK 550, Balzers). The J_{sc}-V_{oc} characteristics as well as the illuminated current-voltage (J-V) curves are measured under standard testing conditions at 1 sun and $25°C$ using a LOANA measurement system (PV-Tools, Hamelin, Germany). The series resistance R_s is determined from the measured fill factor FF, pseudo-fill factor pFF as well as the measured J_{sc} and V_{oc} values using the equation:

$$FF = pFF\left(1 - \left(\frac{R_s J_{sc}}{V_{oc}}\right)\right).$$
(4.1)

Figures 4.17 and 4.18 show the most important solar cell parameters, specifically the short-circuit current density J_{sc}, the open-circuit voltage V_{oc}, the series resistance R_s, and the energy conversion efficiency η, of the processed BackPEDOT solar cells as a function of the spin coating speed. Figure 4.17a shows the measured short-circuit current density J_{sc} of the fabricated BackPEDOT solar cells for different spin coating speeds during the deposition of the PEDOT:PSS precursor dispersion. The median, as well as the respective maximum values for J_{sc} are summarized in Table 4.2 for solar cells fabricated on 0.5-Ωcm and 1.3-Ωcm p-type FZ silicon base material. The maximum J_{sc} value of BackPEDOT cells fabricated on 0.5-Ωcm silicon base material is $38.5\,mA/cm^2$ for a spin coating speed of 1500 rpm. We observe a decrease of the maximum J_{sc} for spin coating speeds above 1500 rpm. The median J_{sc} decreases by $0.2\,mA/cm^2$ for an increase of the spin coating speed of 1500 to 12000 rpm. A decrease of the median J_{sc} and the maximum J_{sc} for spin coating speeds above 1500 rpm on solar cells on 0.5-Ωcm silicon base material is not evident from the ray tracing simulations in Figure 4.15. The solar cells on 1.3-Ωcm silicon base material provide higher J_{sc} values compared to the solar cells fabricated on 0.5-Ωcm base material, which can be attributed to the much higher bulk lifetime in the silicon material with lower

Figure 4.17: (a) Measured short-circuit current density J_{sc} of the fabricated BackPEDOT solar cells for different spin coating speeds during the application of the PEDOT:PSS precursor dispersion. (b) Measured open-circuit voltages V_{oc} of the fabricated solar cells for different spin coating speeds during the application of the PEDOT:PSS precursor dispersion. Solar cells have been fabricated on p-type FZ silicon wafers with a base resistivity of $0.5\,\Omega$cm (red triangles) and $1.3\,\Omega$cm (blue circles), respectively. The V_{oc} values of solar cells with 0.5-Ωcm, as well as with 1.3-Ωcm p-type silicon base material are summarized as a box plot for each investigated spin coating speed.

doping concentration. Lifetime measurements performed on the 0.5-Ωcm p-type FZ-Si material verified that the bulk lifetime of this material is $(0.68 \pm 0.07)\,\text{ms}$ (average value of five measured samples), whereas that of the 1.3-Ωcm material is $(1.33 \pm 0.32)\,\text{ms}$ (average value of three measured samples) at an excess carrier concentration Δn of $3 \times 10^{15}\,\text{cm}^{-3}$. The maximum and median J_{sc} values for BackPEDOT cells fabricated on 1.3-Ωcm silicon base material are also shown in Table 4.2. $38.8\,\text{mA/cm}^2$ is the best J_{sc} value achieved on a BackPEDOT solar cell with 1.3-Ωcm base material at a spin coating speed of $\omega = 12000\,\text{rpm}$. We observe tendency of the maximum and median J_{sc} to higher values with increasing spin coating speed. This result is consistent with the results of the ray-tracing simulations and the test samples shown in Figure 4.13. The measured open-circuit voltage V_{oc} for manufactured solar cells with 0.5-Ωcm and 1.3-Ωcm FZ silicon base materials are shown as a function of the spin coating speed during PEDOT:PSS deposition in Figure 4.17b. Since no relevant impact of the base material on the V_{oc} values is observable, the V_{oc} values for both base materials are summarized as a boxplot for each investigated spin coating speed. The maximum achieved

Table 4.2: Maximum and median J_{sc} values for different spin coating speeds during the deposition of the PEDOT:PSS precursor dispersion on solar cells with 0.5-Ωcm and 1.3-Ωcm base material.

Spin coating speed ω [rpm]	0.5-Ωcm base material		1.3-Ωcm base material	
	Maximum J_{sc} [mA/cm^2]	Median J_{sc} [mA/cm^2]	Maximum J_{sc} [mA/cm^2]	Median J_{sc} [mA/cm^2]
500 (3 solar cells)	38.1	37.5	–	–
1500 (21 solar cells)	38.5	37.6	38.7	38.3
6000 (6 solar cells)	38.3	38.3	38.8	38.2
12000 (17 solar cells)	38.1	37.5	38.8	38.4

Table 4.3: Maximum and median V_{oc} values of manufactured BackPEDOT cells for different spin coating speeds during the deposition of the PEDOT:PSS precursor dispersion.

Spin coating speed ω [rpm]	Maximum V_{oc} [mV]	Median V_{oc} [mV]
500 (3 solar cells)	659	659
1500 (21 solar cells)	664	654
6000 (6 solar cells)	659	656
12000 (17 solar cells)	657	654

V_{oc} values, as well as the median V_{oc} values, are shown in Table 4.3. We observe a decrease of the maximum and median V_{oc} values with increasing spin coating speed. However, there are outliers with high V_{oc} values of up to 664 mV for a spin coating speed of 1500 rpm. The reason for the decrease in V_{oc} is that with decreasing PEDOT:PSS layer thickness the recombination at the silicon/PEDOT:PSS interface increases. This was already indicated by the measured recombination current density parameter $J_{0,PEDOT}$ on lifetime samples in Figure 4.6. A spin coating speed of $\omega = 6000$ rpm corresponds to a resulting PEDOT:PSS thickness of about $d = 134 \pm 10$ nm. A saturation tendency in the V_{oc} becomes apparent for spin coating speeds below $\omega = 6000$ rpm. Thus, the measured V_{oc} values are in accordance with the $J_{0,PEDOT}$ values, which were shown in Figure 4.6. Figure

4.18a shows the measured series resistance R_s of the fabricated BackPEDOT solar cells for different spin coating speeds. The median and maximum values for

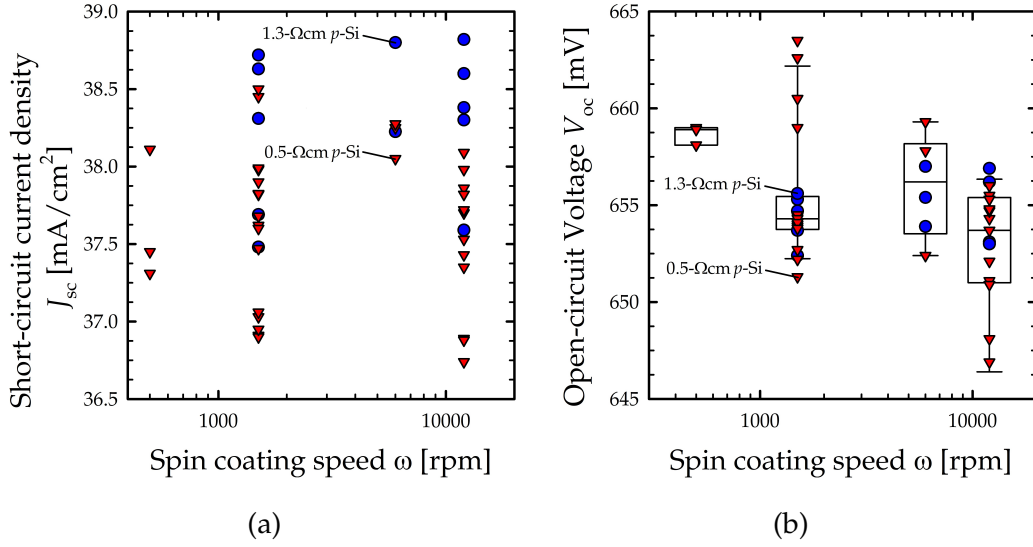Figure 4.18: (a) Measured series resistance R_s of the fabricated BackPEDOT solar cells for different spin coating speeds during the application of the PEDOT:PSS precursor dispersion. (b) Measured solar cell efficiency η of the fabricated solar cells for different spin coating speeds during the application of the PEDOT:PSS precursor dispersion. Solar cells have been fabricated on p-type silicon wafers with a base resistivity of $0.5\,\Omega$cm (red triangles) and 1.3-Ωcm (blue circles), respectively. The data of solar cells with 0.5-Ωcm-, as well as 1.3-Ωcm base material are summarized as a box plot for each investigated spin coating speed.

R_s are summarized in Table 4.4. Solar cells processed at a spin coating speed of $\omega = 500$ rpm show a median series resistance of $R_s = 1.95\,\Omega$cm^2, which is the highest series resistance of all investigated spin coating speeds. If the spin coating speed is increased, and therefore the thickness of the PEDOT:PSS layer is reduced, the median R_s value decreases to $R_s = 0.97\,\Omega$cm^2 for $\omega = 1500$ rpm and saturates for higher spin coating speeds. This indicates that thick PEDOT:PSS layers provide the largest contribution to R_s. However, we obtained the lowest achieved series resistances of $R_s = 0.55\,\Omega$cm^2 for $\omega = 12000$ rpm. The energy conversion efficiency η is shown in Figure 4.18b in dependence of the investigated spin coating speeds. The median and maximum efficiencies are also summarized in Table 4.5. The lowest energy conversion efficiency of $\eta = 18.1\%$ is obtained for solar cells where PEDOT:PSS was deposited at a spin coating speed of 500 rpm, although these solar cells show the best V_{oc} values in Figure 4.17b, but also the highest series resistance with a median of $R_s = 1.95\,\Omega$cm^2. Analogously to the decrease in

Table 4.4: Minimum and median R_s, as well as maximum and median fill factor *FF* values of manufactured BackPEDOT cells for different spin coating speeds during the deposition of the PEDOT:PSS precursor dispersion.

Spin coating speed ω [rpm]	Minimum R_s [Ωcm^2]	Median R_s [Ωcm^2]	Maximum *FF* [%]	Median *FF* [%]
500 (3 solar cells)	1.92	1.95	73.7	73.6
1500 (21 solar cells)	0.58	0.97	79.6	77.9
6000 (6 solar cells)	0.72	0.81	79.3	78.9
12000 (17 solar cells)	0.55	0.91	80.6	78.6

Table 4.5: Maximum and median η values of manufactured solar cells for different spin coating speeds during the deposition of the PEDOT:PSS precursor dispersion.

Spin coating speed ω [rpm]	Maximum η [%]	Median η [%]
500 (3 solar cells)	18.2	18.1
1500 (21 solar cells)	19.9	19.2
6000 (6 solar cells)	20.1	19.8
12000 (17 solar cells)	20.3	19.3

R_s with increasing spin coating speed, the median energy conversion efficiency increases with increasing spin coating speed. The maximum cell efficiencies also increase from 19.9% at $\omega = 1500$ rpm to 20.1% at $\omega = 6000$ rpm. The best cell efficiency of η = 20.3% was achieved at a spin coating speed of $\omega = 12000$ rpm on a solar cell with a base resistivity of 1.3 Ωcm. The median cell efficiency for spin coating speeds of $\omega = 12000$ rpm is with η = 19.3% is about 0.5% lower in comparison to $\omega = 6000$ rpm, which can be explained by the larger number of solar cells produced compared to the number of solar cells at a spin coating speed of $\omega = 6000$ rpm, because the higher number of solar cells means that the fluctuations in V_{oc}, as well as in J_{sc} and in R_s are larger. The best efficiency measured is 20.3% with PEDOT:PSS deposition at the highest applied spin coating speed of $\omega = 12000$ rpm, resulting in a 64 nm thick PEDOT:PSS layer.

4.4 Chapter Summary

In order to successfully implement PEDOT:PSS into BackPEDOT solar cells, the optimized process parameters for the fabrication of the PEDOT:PSS layer were determined. Thermal annealing for 10 min at $130°$C on a hotplate was found to improve the selectivity of PEDOT:PSS. In this thesis we showed, that the passivation of planar silicon surfaces with PEDOT:PSS exhibits a pronounced dependence of the PEDOT:PSS layer thickness. The passivation quality of PEDOT:PSS decreases with decreasing PEDOT:PSS layer thickness. On random-pyramid textured silicon surfaces covered with PEDOT:PSS we detected for the first time, a thin organic layer in the valleys between the pyramids of the silicon surface beneath the deposited PEDOT:PSS layer. We measured a different atomic composition of the thin organic layer in comparison to the PEDOT:PSS layer on top and concluded, that the thin PEDOT:PSS layer is probably responsible for the passivation of textured Si surfaces with PEDOT:PSS and that an increased sulfur content has a positive impact on the surface passivation properties. For maximizing the short-circuit current density J_{sc}, ray tracing simulations were performed, which show a dependence of the PEDOT:PSS layer thickness. We demonstrated for the first time on fabricated BackPEDOT solar cells, that J_{sc} increases with decreasing thickness of the PEDOT:PSS layer. The best achieved value for J_{sc} is $38.8 \, \text{mA}/\text{cm}^2$ for a PEDOT:PSS layer thickness of $(64 \pm 10) \, \text{nm}$. The open-circuit voltage V_{oc} decreases with increasing spin coating speed, because the passivation quality of thin PEDOT:PSS films on silicon is reduced. The highest achieved energy conversion efficiency achieved in this Chapter was 20.3% for a PEDOT:PSS layer thickness of $(64 \pm 10) \, \text{nm}$.

5 Impact of Additives to PEDOT:PSS

5.1 Screening of Additives

The previous Chapter showed that the short-circuit current densities J_{sc} of BackPE-DOT solar cells are still limited due to the parasitic absorption of the PEDOT:PSS layer on the solar cell rear. We discovered that the thickness of the PEDOT:PSS layer must be as thin as possible to minimize the parasitic absorption in PE-DOT:PSS of long-wavelength light reaching the solar cell rear. However, we have also observed that by reducing the PEDOT:PSS layer thickness, the passivation quality of PEDOT:PSS is reduced, resulting in lower open-circuit voltages V_{oc} of BackPEDOT solar cells. In this Chapter, we examine whether additives to the PEDOT:PSS can be used to improve both the short-circuit current density J_{sc} and the passivation quality. The impact of the admixture of additives on the solar cell parameters open-circuit voltage V_{oc}, short-circuit current density J_{sc}, series resistance R_s and energy conversion efficiency η of processed BackPEDOT solar cells is investigated. Additives have already been reported in the literature to increase the conductivity of PEDOT:PSS[89, 90, 91]. The addition of polyvinyl alcohol (PVA) to the PEDOT:PSS precursor dispersion has a potential to reduce the parasitic absorption in PEDOT:PSS due to its transparency in the visible as well as in the infrared wavelength range[92, 93]. Furthermore, the impact of sorbitol admixture to the PEDOT:PSS precursor dispersion is investigated. Sorbitol remains in the resulting PEDOT:PSS layer, similar to PVA, and due to its transparency in the visible and the infrared wavelength range, sorbitol might also reduce the parasitic absorption in PEDOT:PSS.

5.1.1 Polyvinyl Alcohol

Blends of PEDOT:PSS and Polyvinyl Alcohol (PVA) have already found some application fields. Among them for example, the application in ultrahigh-strain sensors with controlled conductivity[94] or even with PEDOT:PSS coated PVA fibers in conductive textiles[95]. Mixtures of PVA and PEDOT:PSS can also be used in the production of moisture sensors[96]. While PEDOT:PSS exhibits a high conductivity, processed PEDOT:PSS layers are brittle and have a high Young's elasticity module and low ductility[97], making them difficult to use in flexible devices. By mixing PEDOT:PSS and PVA, flexible and at the same time highly conductive layers can be produced[98]. PVA is a highly transparent, water-soluble and low-cost polymer and provides ductility and other mechanical enhancements, while PEDOT:PSS acts as the electrical conductor[98]. Polymer layers of a mixture of PEDOT:PSS and PVA are more transparent than PEDOT:PSS films without PVA due to the transparency of PVA[92, 93]. In order to assess the overall infrared absorption in the PEDOT:PSS layer in this thesis, transmission and reflectance measurements were performed using a Varian Cary 5000 UV-Vis spectrometer. 2.2 wt.% PVA (Sigma Aldrich, Mw 89000-98000, 99% hydrolyzed) were admixed to the PEDOT:PSS precursor dispersion and stirred overnight on a magnetic stirrer. The PEDOT:PSS dispersion has a solid content of 2.2 wt.%. The chemical structure of PVA is shown in Figure 5.1. We deposit the PEDOT:PSS:PVA layers by means of spin coating on a glass substrate and thermal anneal it at 130°C for 10 min. According to Equation (5.1), the spectral absorbance $A(\lambda)$ of the PEDOT:PSS:PVA layer at a given wavelength λ can be calculated from the known spectral reflectance $R(\lambda)$ and transmittance $T(\lambda)$:

$$A(\lambda) = 1 - R(\lambda) - T(\lambda). \tag{5.1}$$

In Figure 5.1, the calculated spectral absorbance $A(\lambda)$ for PEDOT:PSS films with addition of 2.2 wt.% PVA (blue curve) and, for comparison, without addition of PVA (red curve) to the PEDOT:PSS precursor dispersion are shown as a function of the wavelength λ. The PEDOT:PSS film thickness d of the sample with PVA admixture is with $d = 655 \pm 22$ nm, which is about three times as thick as the thickness of the PEDOT:PSS film without addition of PVA having a layer thickness of $d = 207 \pm 10$ nm. Nevertheless, the sample with PVA addition shows a significantly lower absorbance $A(\lambda)$ over the entire examined wavelength range. Figure 5.1 thus confirms the results reported in the literature that the addition of PVA to the PEDOT:PSS precursor dispersion increases the transparency of the processed

PEDOT:PSS layers[92, 93]. It can hence be assumed that the parasitic absorption in PEDOT:PSS on the rear of BackPEDOT solar cells can be effectively reduced by adding PVA to the PEDOT:PSS dispersion. We have also examined the impact of adding PVA to PEDOT:PSS on the passivation quality of PEDOT:PSS on crystalline silicon on the basis of $J_{0.PEDOT}$ values on measured lifetime samples. The results are summarized in Table 5.1. The preparation of lifetime samples is described in Section 4.1.1. $J_{0.PEDOT}$ was extracted from the measured overall J_0 values by subtraction of the $J_{0.SiN}$ value of the SiN_x-passivated wafer surface. $J_{0.SiN}$ was determined on both-sides-SiN_x-passivated wafers with a median value of $(16 \pm 5)\,fA/cm^2$. The error bars of $J_{0.PEDOT}$ indicate the deviation of the mean value. The spin coating speed is 1500 rpm with subsequent thermal annealing at 130°C for 10 min on a hotplate in ambient environment. The PEDOT:PSS dispersions with and without addition of PVA provide comparable $J_{0.PEDOT}$ values as shown in Table 5.1. The passivation quality of PEDOT:PSS seems to be unaf-
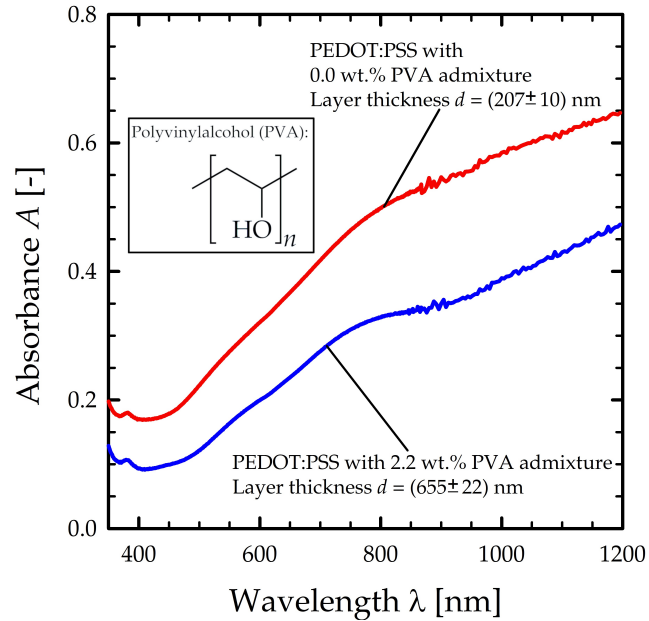
Figure 5.1: Absorbance *A* of PEDOT:PSS layers produced with and without addition of 2.2 wt.% PVA to the PEDOT:PSS precursor dispersion as a function of the wavelength λ. The PEDOT:PSS layer thicknesses *d* and the chemical structure of PVA are also shown.

fected by the addition of PVA. Since no relevant negative impact of the admixture of PVA to the PEDOT:PSS precursor dispersion on the passivation quality of PEDOT:PSS is shown, two BackPEDOT solar cells with and without PVA addition were processed. Table 5.2 summarizes the measured one-sun solar cell parameters open-circuit voltage V_{oc}, short-circuit current density J_{sc}, series resistance R_s

Table 5.1: Recombination current density parameter $J_{0.PEDOT}$ measured on lifetime samples for different PVA contents c_{PVA} of the PEDOT:PSS precursor dispersion.

PVA content of PEDOT:PSS precursor dispersion c_{PVA} [wt.%]	Recombination current density parameter $J_{0.PEDOT}$ [fA/cm^2]
0.0 (4 samples)	74 ± 10
2.2 (3 samples)	84 ± 12

Table 5.2: Solar cell parameters open-circuit voltage V_{oc}, short-circuit current density J_{sc}, series resistance R_s, fill factor FF and energy conversion efficiency η of processed BackPEDOT solar cells with and without addition of $c_{PVA} = 2.0$ wt.% PVA.

PVA content of PEDOT:PSS precursor dispersion c_{PVA} [wt.%]	J_{sc} [mA/cm^2]	V_{oc} [mV]	R_s [Ωcm^2]	FF [%]	η [%]
0.0	38.0	656	0.67	79.4	19.8
2.0	37.8	655	1.86	74.6	18.5

and energy conversion efficiency η of the fabricated BackPEDOT solar cells with and without addition of $c_{PVA} = 2.0$ wt.% PVA to the PEDOT:PSS precursor dispersion. The V_{oc} values of both solar cells are comparable. The addition of PVA does not seem to affect the passivation quality of PEDOT:PSS, as already indicated from the lifetime measurement in Table 5.1. The J_{sc} values are comparable with $J_{sc} = 38.0$ mA/cm^2 without addition of PVA and $J_{sc} = 37.8$ mA/cm^2 with addition of $c_{PVA} = 2.0$ wt.% PVA to the PEDOT:PSS precursor dispersion. To measure a positive impact of the admixture of PVA on the J_{sc} value, higher PVA contents would have to be tested. The series resistance of the solar cell with addition of PVA is $R_s = 1.86$ Ωcm^2, which is significantly higher than the series resistance of $R_s = 0.67$ Ωcm^2 for the solar cell without the addition of PVA. Since the admixture of PVA strongly changes the viscosity of PEDOT:PSS[94] it is not possible to process and simultaneously control the layer thickness by spin coating for higher PVA contents. Also, the higher series resistance indicates that solar cells with even higher PVA contents would most likely not improve with respect to the R_s

value. In summary, PVA can be used to effectively reduce the parasitic absorption in PEDOT:PSS, but to have a relevant effect on J_{sc} in BackPEDOT cells, higher PVA contents must be used, which makes the processing of the PEDOT:PSS dispersion on solar cells difficult due to the strongly increased viscosity[94].

5.1.2 Sorbitol

In the literature sorbitol, is already established as a electrical conductivity additive for PEDOT:PSS[99, 100, 101]. Sorbitol causes the PEDOT-rich clusters in the PEDOT:PSS matrix to reorganize into elongated and aligned clusters, which enhances the electrical conductivity[102, 103]. Due to the transparency of sorbitol in the wavelength range, which is relevant for solar cells, it is useful to examine whether the addition of sorbitol can reduce the parasitic absorption in PEDOT:PSS. In order to assess the overall infrared absorption in the PEDOT:PSS layer, we perform transmission and reflectance measurements using a UV-Vis spectrometer (Cary 5000, Varian). The PEDOT:PSS:sorbitol layer is processed on a glass substrate and thermally annealed at 130°C for 10 min. Figure 5.2 shows the spectral absorbance $A(\lambda)$ for a PEDOT:PSS layer without addition of sorbitol (red curve) for a PEDOT:PSS layer thickness of $d = (309 \pm 20)$ nm. The used PEDOT:PSS dispersion has a solid content of 2.2 wt.%. A minimum of the
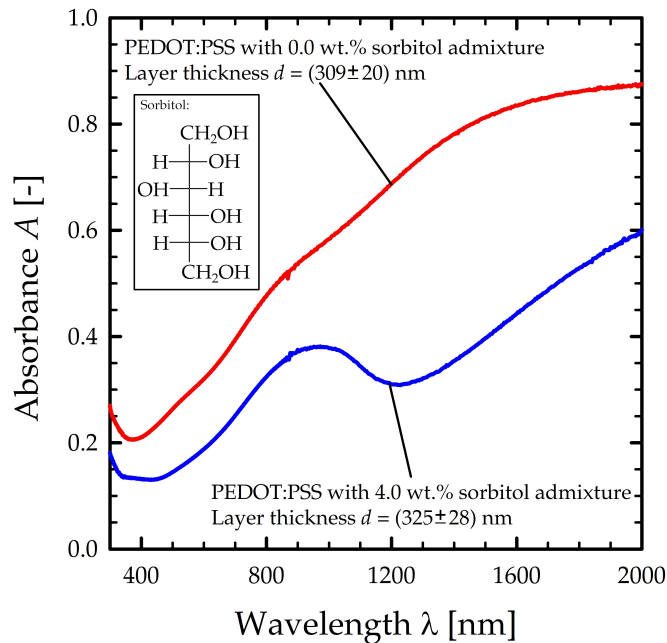

Figure 5.2: Spectral absorbance $A(\lambda)$ of PEDOT:PSS layers produced with and without addition of 4.0 wt.% sorbitol to the PEDOT:PSS precursor dispersion. The PEDOT:PSS layer thicknesses d are also shown.

spectral absorbance is visible at a wavelength of $\lambda = 394$ nm. At shorter wavelengths the absorption increases, which is caused by the excitation of charge carriers from the highest occupied energy level in the PEDOT:PSS to the lowest unoccupied energy level[104]. In the literature, optical absorption spectra measured for various applied voltages to the PEDOT:PSS film[105] show that charges are electrochemically stored in the polymer in the form of polarons or bilpolarons[106, 107, 108, 109]. A polaron is a quasi-particle which is formed due to the polarization of the crystal lattice by charged particles. The energy levels of polarons are within the band gap and transitions between the conduction band and polaron energy levels are associated with lower energies than excitation of a carrier from the valence band into the conduction band[110, 111, 112]. Thus, in the case of PEDOT:PSS, the generation of polarons for wavelengths longer than $\lambda = 400$ nm becomes visible as increased optical absorption[104]. The absorption peak of polarons in PEDOT:PSS is not a narrow peak, but a very broad maximum and can be explained by the fact that the energy level of polarons depends on the armophilic nature of the PEDOT:PSS film, the lengths distribution of the PEDOT:PSS polymer chains, and the interaction of the charge carriers. This leads to a blurring of the energy levels for polarons. Figure 5.2 also shows the spectral absorbance determined using Equation (5.1) for a PEDOT:PSS film with a thickness of $d = (325 \pm 28)$ nm with addition of $c_{\mathrm{sorb}} = 4.0$ wt.% sorbitol (blue curve). It is obvious that the absorption for all wavelengths is reduced by the addition of sorbitol at a comparable PEDOT:PSS film thickness. Sorbitol reduces the absorption of PEDOT:PSS for two different reasons. Firstly, the addition of sorbitol ensures that sorbitol remains in the PEDOT:PSS film, thus increasing the overall transparency, as sorbitol has a high transparency in the visible wavelengths range. Furthermore, the mixing of sorbitol with PEDOT:PSS ensures that the absorption bands of polarons are reduced. At a wavelength of $\lambda = 975$ nm in Figure 5.2, a maximum of absorption is visible. At a wavelength of about $\lambda = 1250$ nm in Figure 5.2, a minimum of absorption is observed, followed by increase of the absorption at wavelengths longer than $\lambda = 1250$ nm. The decrease of the polaronic band at $\lambda = 1250$ nm suggests that the addition of sorbitol enhances the doping efficiency of PSS, generating more highly doped PEDOT oligomers[113, 114, 115, 116]. It is therefore to be expected that the short-circuit current density J_{sc} on solar cells will increase by adding sorbitol to the PEDOT:PSS precursor dispersion. Of course it remains to be investigated whether the addition of sorbitol has an impact on the passivation quality of PEDOT:PSS. In Table 5.3 the measured recombination current density parameter $J_{0.\mathrm{PEDOT}}$ determined on lifetime samples for PEDOT:PSS

dispersions with and without addition of sorbitol are shown. The preparation of the lifetime samples is described in Section 4.1.1. The spin coating speed for the PEDOT:PSS application is 1500 rpm with subsequent thermal annealing at 130°C for 10 min on a hotplate in ambient environment. Our measurements hence point

Table 5.3: Recombination current density parameter $J_{0.\text{PEDOT}}$ measured on life-time samples for different sorbitol contents c_{sorb} of the PEDOT:PSS precursor dispersion.

Sorbitol content of PEDOT:PSS precursor dispersion c_{sorb} [wt.%]	Recombination current density parameter $J_{0.\text{PEDOT}}$ [fA/cm^2]
0.0 (4 samples)	74 ± 10
4.0 (2 samples)	44 ± 6

Table 5.4: Solar cell parameters open-circuit voltage V_{oc}, short-circuit current density J_{sc}, series resistance R_{s}, fill factor FF and energy conversion efficiency η of processed BackPEDOT solar cells with and without addition of sorbitol.

Sorbitol content of PEDOT:PSS precursor dispersion c_{sorb} [wt.%]	J_{sc} [mA/cm^2]	V_{oc} [mV]	R_{s} [Ωcm^2]	FF [%]	η [%]
0.0	38.0	656	0.67	79.4	19.8
4.0	38.0	658	0.66	80.3	20.1

for the first time towards a positive impact of the admixture of sorbitol to the PEDOT:PSS dispersion on the passivation quality of PEDOT:PSS. The measured cell parameters of BackPEDOT solar cells with and without addition of sorbitol to the PEDOT:PSS precursor dispersions are shown in Table 5.4. As expected from the measured $J_{0.\text{PEDOT}}$ values from Table 5.4, the solar cell with addition of $c_{\text{sorb}} = 4.0$ wt.% sorbitol shows a slightly increased V_{oc} value compared to the solar cell without sorbitol admixture. The J_{sc} value is surprisingly the same for both solar cells. The series resistance of $R_{\text{s}} = 0.66 \,\Omega$cm^2 is also comparable for both solar cells. Thus, the admixture of sorbitol seems to be more promising compared to the other additives examined in this study. We have examined in more detail

the impact of sorbitol content, layer thickness and annealing conditions in the framework of this thesis.

5.2 Optical Properties of PEDOT:PSS:Sorbitol

In Section 5.1, we demonstrated that sorbitol is a suitable additive for PEDOT:PSS, as it seems to improve the transparency of PEDOT:PSS without deteriorating the series resistance of the manufactured solar cells. In this Section, we examine the optical properties of the PEDOT:PSS layer with admixture of sorbitol to the precursor dispersion in more detail. The objective is to determine the optimal sorbitol concentration in the PEDOT:PSS precursor dispersions, as well as the optimal layer thickness of the PEDOT:PSS:sorbitol layer on the rear of the solar cell rear to maximize the short circuit current density J_{sc}. In order to assess the overall infrared absorption in the PEDOT:PSS layer, transmission and reflectance measurements are performed using a UV-Vis spectrometer (Cary 5000, Varian). According to Equation (5.1), the absorbance of PEDOT:PSS:sorbitol for a given wavelength is calculated. Table 5.5 summarizes the absorbance A at a wavelength of $\lambda = 1200$ nm for different PEDOT:PSS layer thicknesses and for different sorbitol contents c_{sorb} of the PEDOT:PSS precursor dispersion. The thickness d of the PEDOT:PSS layers deposited on glass substrates is determined by a profilometer (Dektak 150, Veeco). For a PEDOT:PSS layer without addition of sor-

Table 5.5: Absorbance A at a wavelength of $\lambda = 1200$ nm for different PEDOT:PSS layer thicknesses and for different sorbitol contents c_{sorb} of the PEDOT:PSS precursor dispersion.

Sorbitol content of PEDOT:PSS precursor dispersion c_{sorb} [wt.%]	PEDOT:PSS layer thickness d [nm]	Absorbance A at $\lambda = 1200$ nm [%]
0.0	317 ± 20	55.5
1.0	228 ± 19	36.7
2.0	266 ± 20	35.3
4.0	341 ± 28	28.4
7.7	680 ± 69	28.3
14.4	1540 ± 235	24.3

bitol in the precursor dispersion and a layer thickness of $d = (317 \pm 20)$ nm, the

absorbance A is 55.5% at a wavelength of $\lambda = 1200\,\text{nm}$. If the sorbitol content is increased to 7.7 wt.%, an absorbance of 28.3% is obtained for a layer thickness of $d = (680 \pm 69)\,\text{nm}$, although the layer thickness is twice as large as for the sample with 4.0 wt.%. The addition of sorbitol to the PEDOT:PSS precursor dispersion thus significantly increases the transparency at a wavelength of 1200 nm. Using the tabulated AM 1.5G[84] spectrum and the measured spectral absorbance $A(\lambda)$ of the PEDOT:PSS:sorbitol layer, the parasitic absorption of PEDOT:PSS can be estimated. We determine the equivalent absorbed current density $J_{\text{PEDOT:PSS}}$ in the PEDOT:PSS layer using the following equation:

$$J_{\text{PEDOT:PSS}} = \frac{q}{d} \sum_{\lambda=300}^{1200} A(\lambda)\Phi_{1.5G}(\lambda). \tag{5.2}$$

Here q is the elementary charge and $\Phi_{1.5G}(\lambda)$ is the photon flux of the AM 1.5G spectrum. Figure 5.3 shows the equivalent absorbed current density $J_{\text{PEDOT:PSS}}$ of the AM 1.5G spectrum for different sorbitol contents of the PEDOT:PSS precursor dispersion. The $J_{\text{PEDOT:PSS}}$ values are normalized with respect to the equivalent absorbed current density $J_{\text{PEDOT:PSS}}$ for a sorbitol content of the PEDOT:PSS precursor dispersion of 0.0 wt.%. The PEDOT:PSS precursor dispersion has a solid content of 2.2 wt.%. The PEDOT:PSS:sorbitol films investigated in this study are deposited on glass substrates with a spin coating speed of $\omega = 1500\,\text{rpm}$. PEDOT:PSS was then annealed for 10 min at 130°C in ambient environment. The PEDOT:PSS layers, to which different amounts of sorbitol were added to the precursor dispersion, shows reduced $J_{\text{PEDOT:PSS}}$ values and thus a significantly improved transparency. The $J_{\text{PEDOT:PSS}}$ values show a strong dependence on the sorbitol content of the precursor dispersion. Sorbitol concentrations of only $c_{\text{sorb}} = 2.1\,\text{wt.%}$ of the precursor dispersion are sufficient to reduce the absorbed current density in PEDOT:PSS by almost 50%. At a sorbitol concentration of $c_{\text{sorb}} = 7.7\,\text{wt.%}$ of the precursor dispersion, the absorbed current density in the PEDOT:PSS layer is reduced to 20 % in comparison to the PEDOT:PSS without admixture of sorbitol. With a higher sorbitol content in the precursor dispersion, the absorbed current density in PEDOT:PSS can be further reduced. As transmission measurements through a layer of PEDOT:PSS on a glass substrate do not correspond to the absorption behavior in solar cells due to the rear reflector in solar cells, reflection spectra of test samples are investigated analogously to Chapter 4.2. The test samples have the same structure as the BackPEDOT solar cells for which PEDOT:PSS is applied to the rear side. A schematic representation of the test structures is shown in Figure 5.4. The PEDOT:PSS dispersion used
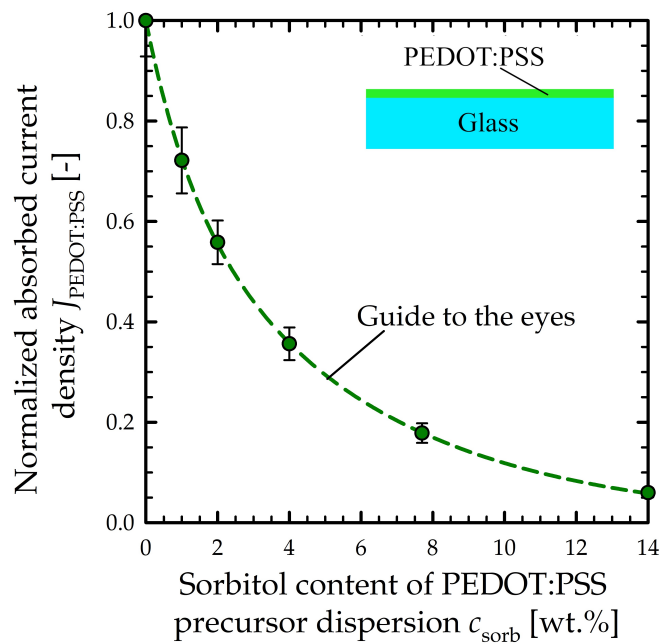
Figure 5.3: Normalized equivalent absorbed current density $J_{PEDOT:PSS}$ of the AM 1.5G spectrum of a PEDOT:PSS layer with admixture of different percentage amounts of sorbitol to the precursor dispersion. The data points have been calculated according to Equation (5.2) from transmission and reflection measurements on the shown test samples. The error bars result from the inhomogeneity of the thickness of the PEDOT:PSS layers. The dashed green line serves as a guide to the eye.

has a solid content of 2.2 wt.% and the PEDOT:PSS:sorbitol layer is annealed for 10 min at 130°C for all investigated sorbitol concentrations. For a better comparability of the reflectance curves, only the reflectance R_{PEDOT} at a wavelength of $\lambda = 1200$ nm is considered. Figure 5.4 shows the reflectance R_{PEDOT} at a wavelength of $\lambda = 1200$ nm as a function of the PEDOT:PSS layer thickness. The PEDOT:PSS layer thickness shown in Figure 5.4 is the median value over a 2×2 cm^2 area of a test sample. The error bars represent the deviation from the median value and are an indication of the inhomogeneity of the PEDOT:PSS layer over the entire sample. PEDOT:PSS thickness measurements were performed in 1 mm intervals over a length of 2 cm (20 data points) centered over the sample center using a profilometer (Dektak 150, Veeco). The reflectance R_{PEDOT} for samples without added sorbitol to the PEDOT:PSS precursor dispersion was already discussed in the previous Chapter 4.2. It was shown that the reflectance is maximized if the PEDOT:PSS layer thickness is minimized. In Figure 5.4 PEDOT:PSS layers with sorbitol concentrations up to $c_{sorb}=4.0$ wt.% provide an increased reflectance at a wavelength of $\lambda = 1200$ nm compared to PEDOT:PSS layers without addition of
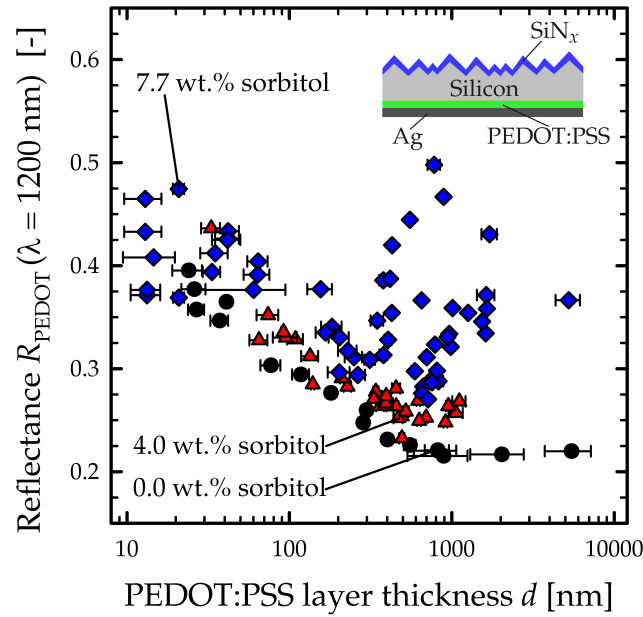
Figure 5.4: Reflectance R_{PEDOT} at a wavelength of $\lambda = 1200\,nm$ of test samples as a function of the PEDOT:PSS layer thickness d for sorbitol concentrations c_{sorb} of $c_{sorb} = 0.0\,wt.\%$ (black circles), $c_{sorb} = 4.0\,wt.\%$ (red triangles) and $c_{sorb} = 7.7\,wt.\%$ (blue diamonds) of the PEDOT:PSS precursor dispersion.

sorbitol to the PEDOT:PSS precursor dispersion. For a sorbitol concentrations of $c_{sorb} = 7.7\,wt.\%$, the measured R_{PEDOT} values for all investigated PEDOT:PSS layer thicknesses are significantly larger than without addition of sorbitol. Nevertheless, there are some data points which provide a comparable reflectance as samples without added sorbitol. A possible explanation for this would be that sorbitol is apparently incorporated in the PEDOT:PSS matrix in varying quantities. Thus, there are PEDOT:PSS layers with the same sorbitol content in the precursor dispersion, but the sorbitol content in the resulting PEDOT:PSS layer can be laterally inhomogeneous. This explains the fluctuation in reflectance when sorbitol is added at a constant PEDOT:PSS layer thickness. If by chance more sorbitol is added at the same layer thickness, the PEDOT:PSS film is more transparent, if less sorbitol is added to the PEDOT:PSS matrix, the parasitic absorption of the layer is increased. If no sorbitol is incorporated into the PEDOT:PSS layer, the same reflectance is measured as for samples without sorbitol admixture to the precursor dispersion. The fluctuations to higher reflectance values become larger if the sorbitol content of the PEDOT:PSS precursor dispersion is higher. It is noticeable in Figure 5.4 that the variations in the measured reflectance values R_{PEDOT} for PEDOT:PSS layer thicknesses greater than $d = 300\,nm$ and at a sor-

bitol concentration of $c_{sorb} = 7.7$ wt.% become quite large. If the PEDOT:PSS layer is thicker, it is more likely that there are areas where sorbitol could accumulate which are optically highly transparent. This large scattering of the data towards high reflectance values for thick PEDOT:PSS layer thicknesses is not observable for a lower sorbitol concentrations of $c_{sorb} = 4.0$ wt.%. The scattering could therefore be explained by the formation of *sorbitol domains*, i.e. areas where a very high amount of sorbitol is incorporated in the PEDOT:PSS matrix. These domains occur preferentially in thick PEDOT:PSS:sorbitol layers with large sorbitol contents of the PEDOT:PSS precursor dispersion. Figure 5.5 shows a optical microscopy image of a PEDOT:PSS layer with a sorbitol addition of $c_{sorb} = 7.7$ wt.% to the PEDOT:PSS precursor dispersion. Two different morphologies appear on
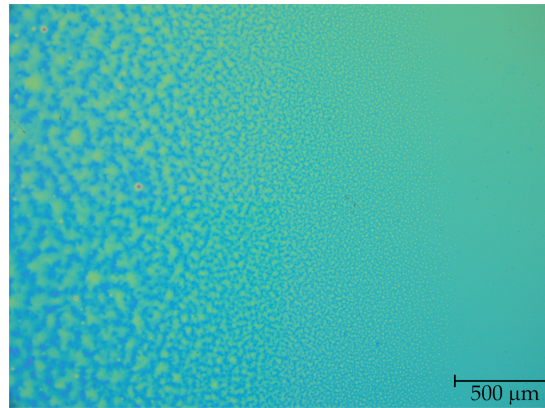
Figure 5.5: Optical microscopy image of the surface of a PEDOT:PSS layer with addition of $c_{sorb} = 7.7$ wt.% sorbitol to the PEDOT:PSS precursor dispersion.

the surface of the PEDOT:PSS layer. On the right side of the optical microscopy image, a relatively homogeneous PEDOT:PSS surface can be seen. In the middle of the image, there are some small islands formation, which have a slightly different layer thickness and therefore can be easily distinguished in the light microscopy image due to the interference effects of the light within the PEDOT:PSS film. The islands formed become larger towards the left side of the image. We assume, that the microscopy image shows a boundary region between a PEDOT:PSS:sorbitol domain with high sorbitol content in the formed islands and a PEDOT:PSS:sorbitol domain with homogenously distributed sorbitol of lower content. It is possible that the core of these morphological islands consists of a sorbitol cluster. The left part of the image in Figure 5.5 will probably have more sorbitol in the PEDOT:PSS:sorbitol matrix than the right part of the image, which could show up as a sorbitol gradient from left to right. To confirm this assumption, we have performed reflectance and transmittance measurements on differ-

ent areas of the sample. Figure 5.6a shows the absorbance of the PEDOT:PSS film as a function of the wavelength. The PEDOT:PSS:sorbitol layer was processed on a silicon substrate and was thermally annealed on a hotplate in ambient environment at 130°C for 10 min. The absorbance was calculated using Equation (5.1). Figure 5.6b shows the areas of the sample surfaces where the absorbance and transmittance measurements were performed. The absorbance of the two sam-

(a)

(b)
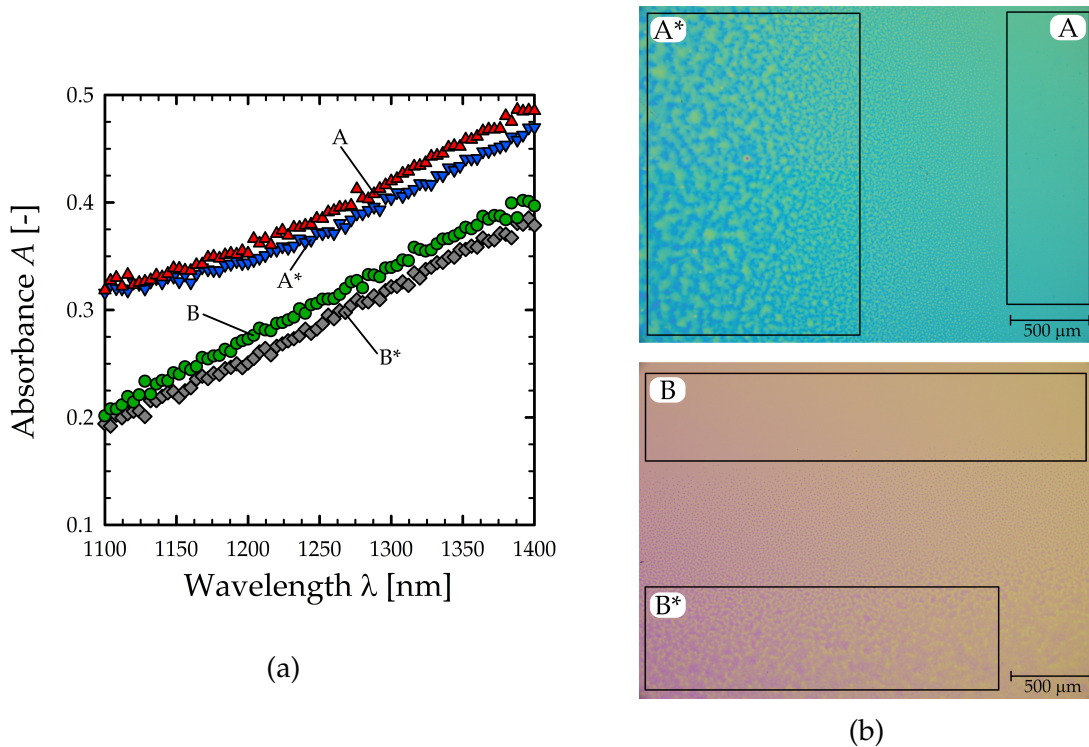
Figure 5.6: (a) Absorbance *A* of PEDOT:PSS layers at different locations on sample A (location A and A*) and on sample B (location B and B*) (b) The optical microscopy image on top shows the PEDOT:PSS surface of sample A. The locations A and A*, where absorbance and transmittance measurements were performed, are indicated in boxes. At the bottom the same is shown for sample B.

ples is slightly different, as the two samples have different PEDOT:PSS:sorbitol layer thicknesses. The absorbance measured in area A is slightly higher for all wavelengths than the absorbance measured in the location A*. The location A* was chosen so that it lies within the range that shows a pronounced island morphology. The same measurement was verified on another sample with a different PEDOT:PSS:sorbitol thickness. The measurement was carried out at location B and is within the homogeneous area of the sample. Another measurement was carried out in location B*. Location B* is again in the area of the island morphology. Here, the measurement in location B* shows also reduced absorbance in comparison to location B. From this result it can be concluded that areas of the

PEDOT:PSS:sorbitol film which show the island morphology have an increased transparency for wavelengths of the investigated wavelengths range. It can be assumed that sorbitol is present and enriched in these areas. Figure 5.7a shows a light microscopy image of a PEDOT:PSS film with admixture of $c_{sorb} = 7.7 \, \text{wt.\%}$ sorbitol to the PEDOT:PSS precursor dispersion. The image shows the island

(a) (b)
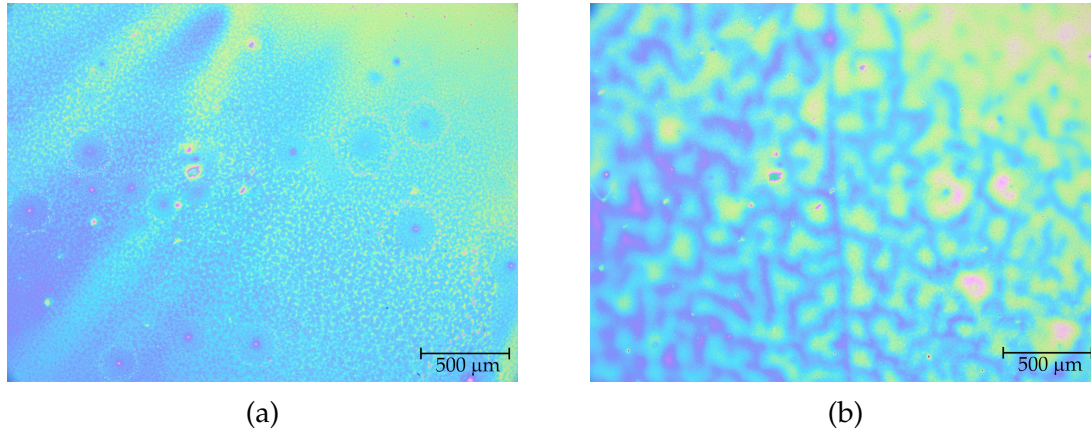
Figure 5.7: Optical microscopy images of the PEDOT:PSS surface of a sample processed with addition of 7.7 wt.% sorbitol in the PEDOT:PSS precursor dispersion. (a) Optical microscopy image of the PEDOT:PSS surface. (b) Optical microscopy image of the PEDOT:PSS surface after exposure to high air humidity. The position and magnification are exactly the same as in picture (a).

morphology of a PEDOT:PSS:sorbitol layer. We assume, that the areas of changed layer thickness are accumulations of sorbitol or sorbitol clusters within the PEDOT:PSS layer. To verify this hypothesis, the sample is briefly exposed to a very high humidity and then examined again under the optical microscope. Figure 5.7b shows the sample surface of the PEDOT:PSS film after exposure to high humidity at the exact same place and magnification. The resulting image is completely different. Due to the hygroscopic properties of sorbitol [117] water from the humidity seems to migrate into the PEDOT:PSS:sorbitol film and binds to the sorbitol. The island-shaped areas thus swell and become larger. In summary, we conclude that sorbitol accumulates in sorbitol clusters within the PEDOT:PSS layer when a high content of sorbitol is admixed. The domains with particularly high sorbitol contents occur preferably in thick PEDOT:PSS:sorbitol layers.

5.3 Electrical Properties of PEDOT:PSS:Sorbitol

In Section 4.1.1 of this thesis, the optimal annealing conditions for PEDOT:PSS without addition of sorbitol to the precursor dispersion were examined. The opti-

mal PEDOT:PSS annealing conditions were determined for a layer of PEDOT:PSS without addition of sorbitol to be 10 min at 130°C. It remains to be investigated, which impact the addition of sorbitol to the PEDOT:PSS precursor dispersion has on the specific contact resistance of the Ag/PEDOT:PSS:sorbitol/c-Si junction as well as on the passivation quality of PEDOT:PSS on the c-Si surface. The sample preparation is described in Section 4.1.1 and the Cox and Strack method is described in detail in Section 3.6. Specific contact resistances extracted by the Cox and Strack method[68] are shown in Figure 5.8 for PEDOT:PSS films with 7.7 wt% sorbitol admixture to the precursor dispersion for different annealing durations in ambient environment at temperatures of 130°C and 190°C, respectively. The PEDOT:PSS application is performed with a spin coating procedure of 10 s at a spin coating speed of 500 rpm and 30 s at 5000 rpm. The extracted values of the specific contact resistance for the Ag/PEDOT:PSS:sorbitol/c-Si junction scatter over a broad range between 56.3 and 607 mΩcm^2 for the admixture of 7.7 wt.% of sorbitol to the PEDOT:PSS precursor dispersion. No clear dependence on the annealing temperature and the annealing duration is visible. The best overall value for the specific contact resistance of 56.3 mΩcm^2 is obtained for an annealing duration of $t = 90$ min at an annealing temperature of 130°C. In Section 5.1.2 it was shown that sorbitol has a positive effect on the passivation quality of PEDOT:PSS on c-Si surfaces. The correlation between the sorbitol content of the PEDOT:PSS precursor dispersion and the passivation quality is investigated in this Section. Figure 5.9 shows a box plot of the measured recombination current density parameter $J_{0.\text{PEDOT}}$ of the PEDOT:PSS/c-Si interface as a function of the sorbitol content added to the PEDOT:PSS precursor dispersion. The $J_{0.\text{SiN}}$ value of (16 ± 5) fA/cm^2 of the SiN$_x$-passivated silicon surface was subtracted from the measured J_0 value to account only for recombination at the PEDOT:PSS/c-Si interface. Table 5.6 shows the PEDOT:PSS layer thicknesses and the total sheet resistance R_{sheet} of the lifetime samples shown in Figure 5.9. Mean PEDOT:PSS layer thicknesses measured using a profilometer (Dektak 150, Veeco) and total sheet resistances of the lifetime samples measured using a Sinton lifetime tester (WCT-120, Sinton Instruments). The PEDOT:PSS layers were spin-coated at 500 rpm for 10 s followed by 1500 rpm for 30 s. The PEDOT:PSS layer thickness measurements were performed in 1 mm steps over a length of 2 cm (20 data points) centered in the sample center. The error bars result from the deviation of the mean value. The thickness of the PEDOT:PSS layers was limited to $(d > 900$ nm$)$ so that the surface passivation of the lifetime samples is in saturation and small variations in the PEDOT:PSS layer thickness have no negative impact on the passivation
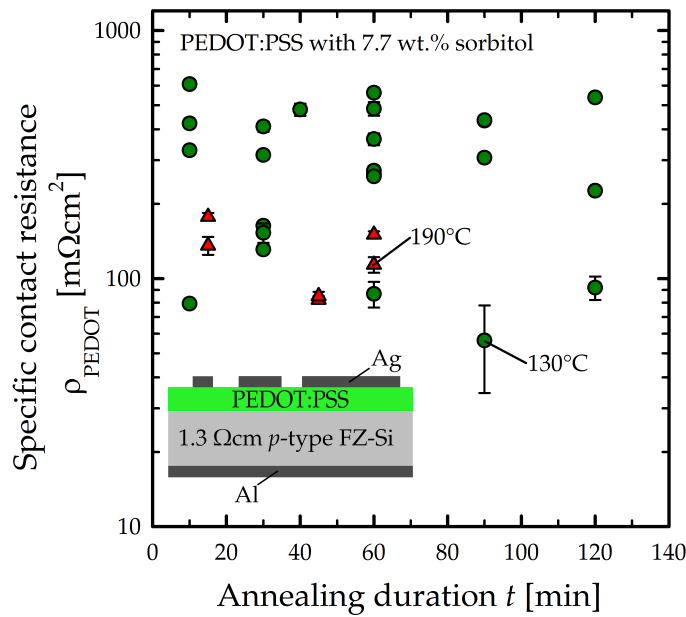
Figure 5.8: Specific contact resistance ρ_{PEDOT} of the Ag/PEDOT:PSS/c-Si junction extracted by the Cox and Strack method as a function of the PEDOT:PSS annealing duration in ambient environment at a temperature of 130°C (green circles) and 190°C (red triangles). The PEDOT:PSS precursor dispersion was mixed with 7.7 wt.% sorbitol. The error bars result from the precision of the fit of the measurement data during the evaluation according to Cox and Strack.

quality. For the PEDOT:PSS layer without addition of sorbitol to the precursor dispersion a sheet resistance of $R_{\text{sheet}} = 2269\,\Omega/\square$ is measured. If some sorbitol is added, the sheet resistance for a sorbitol addition of $c_{\text{sorb}} = 2.0\,\text{wt.\%}$ is reduced to $124\,\Omega/\square$ For higher sorbitol concentrations, the sheet resistance saturates between 60 and $80\,\Omega/\square$. The reduction of the sheet resistance by adding more than 1.0 wt.% sorbitol agrees well with the behavior reported in the literature that sorbitol serves as a conductivity-increasing additive[99, 100]. As can been seen from Figure 5.9 increasing sorbitol content results in a decreasing $J_{0.\text{PEDOT}}$. $J_{0.\text{PEDOT}}$ decreases from $86\,\text{fA/cm}^2$ for $c_{\text{sorb}} = 0.0\,\text{wt.\%}$ to $38\,\text{fA/cm}^2$ for $c_{\text{sorb}} = 7.7\,\text{wt.\%}$, which means that the recombination at the PEDOT:PSS/c-Si interface is more than halved by adding 7.7 wt.% of sorbitol to the precursor solution. According to the results, a saturation in $J_{0.\text{PEDOT}}$ for sorbitol concentrations above 5 wt.% of approximately $50\,\text{fA/cm}^2$ can be observed. Nardes et al.[118] have shown that the addition of sorbitol reduces the work function of PEDOT:PSS for sorbitol concentration of 5 wt.%, and for higher sorbitol concentrations a saturation in the work function occurs. The positive impact of sorbitol on the passivation
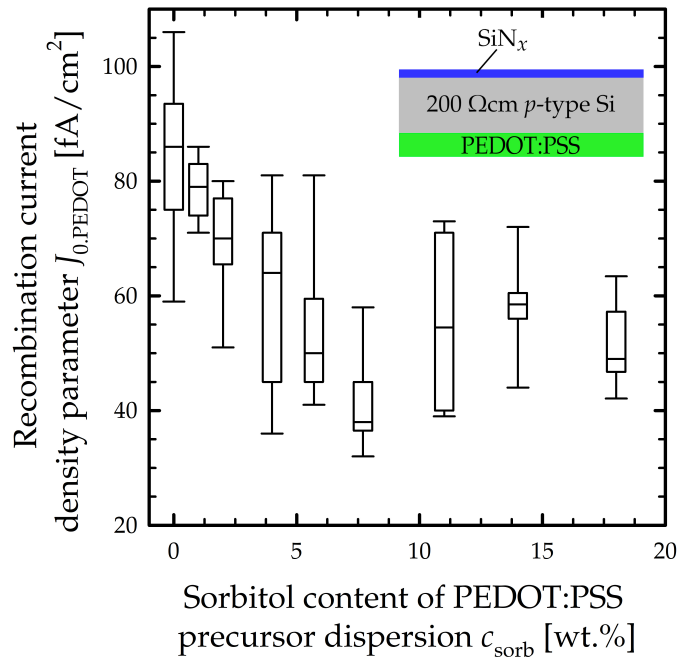
Figure 5.9: Box plot of the recombination current density parameter $J_{0.PEDOT}$ of the PEDOT:PSS/c-Si interface as a function of the sorbitol content of the PEDOT:PSS precursor dispersion. PEDOT:PSS was applied to 9 test samples for each sorbitol concentration.

properties of PEDOT:PSS on c-Si might be due to a change in the electronic band structure of the organic compound. It is well known from the literature that the addition of sorbitol to the PEDOT:PSS precursor dispersion reduces the work function of the PEDOT:PSS with increasing sorbitol content[118, 119, 120, 121]. Our results clearly prove that adding sorbitol to the PEDOT:PSS precursor solution significantly improves the c-Si surface passivation quality for the first time. Of course, not only the sorbitol content of the PEDOT:PSS precursor dispersion can be chosen as a free parameter, but also the annealing duration of the PEDOT:PSS:sorbitol layer. With respect to the $J_{0.PEDOT}$ values, the sorbitol concentration is chosen so that the improvement of the passivation quality by adding sorbitol is in saturation. Thus, a sorbitol content of 7.7 wt.% is chosen and in the following Section the $J_{0.PEDOT}$ values are examined as a function of the annealing duration. The PEDOT:PSS application is performed with a spin coating procedure of 10 s at a spin coating speed of 500 rpm and 30 s at 5000 rpm. Figure 5.10a shows a box plot of the PEDOT:PSS layer thickness without admixture of sorbitol to the PEDOT:PSS precursor dispersion as a function of the sample annealing duration in ambient environment at 130°C. A box represents the PEDOT:PSS layer thicknesses over a $2 \times 2\,cm^2$ area of a test sample. The median value of the PEDOT:PSS film thickness is approximately 136 nm for all annealing

Table 5.6: Mean PEDOT:PSS layer thicknesses and total sheet resistances of lifetime samples for PEDOT:PSS application at a maximum spin coating speed of $\omega = 1500\,\mathrm{rpm}$.

Sorbitol content in the PEDOT:PSS precursor dispersion c_{sorb} [wt.%]	PEDOT:PSS layer thickness d [nm]	Total sheet resistance $R_{\mathrm{sheet}}\,[\Omega/\square]$
0.0	1674 ± 343	2269 ± 293
1.0	978 ± 123	1851 ± 304
2.0	1070 ± 125	124 ± 53.3
4.0	1623 ± 240	67.3 ± 42.6
5.7	2137 ± 237	61.5 ± 24.2
7.7	2087 ± 322	60.2 ± 17.8
11.0	1033 ± 47	99.2 ± 13.2
14.0	1766 ± 52	76.6 ± 5.3
18.0	1936 ± 81	79.6 ± 6.0

durations. There is no change in the layer thickness with increasing annealing duration observable. The mean $J_{0.\mathrm{PEDOT}}$ value for an annealing duration of 10 min is $75\,\mathrm{fA/cm^2}$. Towards longer annealing durations, the $J_{0.\mathrm{PEDOT}}$ values increase. This indicates a degradation of the passivation quality of the PEDOT:PSS. After an annealing duration of 60 min, the PEDOT:PSS passivation provides a $J_{0.\mathrm{PEDOT}}$ value of only $107\,\mathrm{fA/cm^2}$. For annealing durations longer than 60 min, $J_{0.\mathrm{PEDOT}}$ saturates at $J_{0.\mathrm{PEDOT}} = (100 \pm 10)\,\mathrm{fA/cm^2}$. Figure 5.10b shows a box plot of the PEDOT:PSS layer thickness with 7.7 wt.% admixture of sorbitol to the PEDOT:PSS precursor dispersion as a function of the sample annealing duration in ambient environment at 130°C. After an annealing duration of $t = 10\,\mathrm{min}$ at 130°C, a median value of $d = 423\,\mathrm{nm}$ for the PEDOT:PSS layer thickness was determined. With increasing annealing duration, the PEDOT:PSS layer thickness decreases. After $t = 30\,\mathrm{min}$ at 130°C, the PEDOT:PSS layer thickness is reduced to $d = 308\,\mathrm{nm}$ and for 60 min annealing, a median value of $d = 201\,\mathrm{nm}$ is reached. This seems to be the saturation value for the layer thickness of the PEDOT:PSS. The reduction in layer thickness can probably be attributed to evaporation of residual water in the PEDOT:PSS:sorbitol film due to the hygroscopic properties of sorbitol[117]. Figure 5.10b also shows the measured recombination current density parameter $J_{0.\mathrm{PEDOT}}$ of the PEDOT:PSS/c-Si interface as a function of the annealing duration of the PEDOT:PSS layer in ambient environment at a temperature of 130°C.
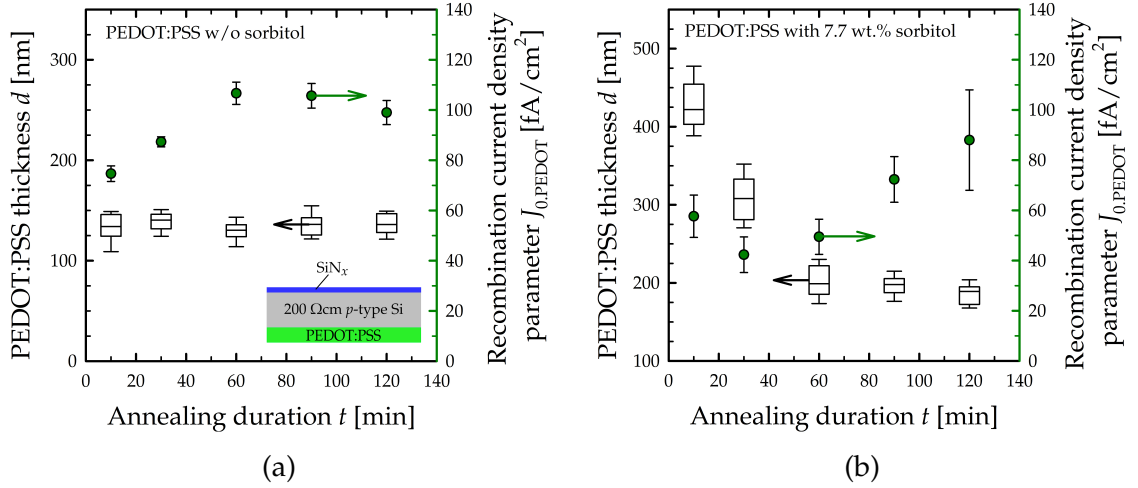
Figure 5.10: Box plot of the PEDOT:PSS layer thickness and average values of the recombination current density parameter $J_{0.PEDOT}$ of the PEDOT:PSS/c-Si interface (green circles) as a function of the sample annealing duration in ambient environment at 130°C for (a) PEDOT:PSS without sorbitol admixture and (b) with 7.7 wt.% sorbitol admixture to the PEDOT:PSS precursor dispersion.

For silicon surfaces passivated with PEDOT:PSS and an annealing duration of the PEDOT:PSS layer of $t = 10$ min, the determined $J_{0.PEDOT}$ value is 58 fA/cm². For longer annealing durations, a decrease in $J_{0.PEDOT}$ and thus an improvement in the passivation quality of PEDOT:PSS:sorbitol is observed. The $J_{0.PEDOT}$ values decrease for an annealing duration of $t = 30$ min to a mean $J_{0.PEDOT}$ value of 42 fA/cm² and to 50 fA/cm² after 60 min annealing. For even longer annealing durations, the $J_{0.PEDOT}$ values increase again up to 72 fA/cm² and 88 fA/cm² for annealing durations of 90 min and 120 min, respectively. We conclude that for an improvement of the passivation of c-Si by PEDOT:PSS:sorbitol, there exists an optimal annealing duration at 130°C between 30 and 60 min. Figure 5.10b also shows that the improvement of the passivation only terminates after the reduction of the layer thickness of the PEDOT:PSS film has stopped. Probably the evaporation of residual water from the organic film at annealing durations between 10 and 60 min leads to an improvement of the passivation quality. Due to the hygroscopic properties of sorbitol[117] in PEDOT:PSS more water is retained in PEDOT:PSS than without the addition of sorbitol. In the literature it has been reported that the evaporation of water from PEDOT:PSS has an impact on the work function, which in this case could explain the improved passivation quality of PEDOT:PSS:sorbitol during longer annealing durations[122]. After the evaporation of a major portion of residual water from the PEDOT:PSS film, a degradation of
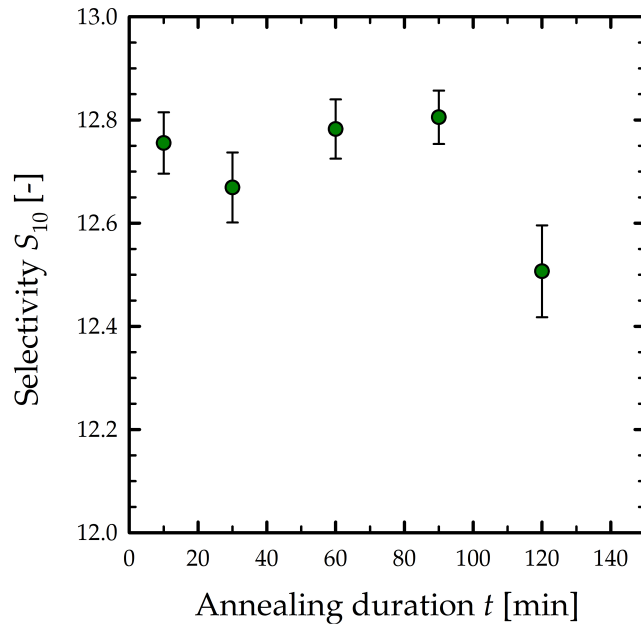
Figure 5.11: Selectivity S_{10} of PEDOT:PSS:sorbitol on c-Si for different annealing durations t.

the passivation is observed for annealing durations longer than $t \approx 60$ min, as can been seen in Figure 5.10a. With the values of the specific contact resistance of the Ag/PEDOT:PSS:sorbitol/c-Si junction extracted by the Cox and Strack method in Figure 5.8, and the $J_{0.PEDOT}$ values of the PEDOT:PSS:sorbitol/c-Si interface in Figure 5.10b, the selectivity of PEDOT:PSS:sorbitol can be calculated using Equation (3.6). Figure 5.11 shows the calculated selectivity S_{10} in dependence of the annealing duration t. We observe here a tendency towards higher selectivities with increasing annealing duration of up to 90 min. For annealing durations longer than 90 min, the selectivity decreases. We report here a maximum value of the selectivity for PEDOT:PSS:sorbitol of 12.8 for an annealing duration of 90 min.

5.4 Solar Cell Results

In this Section, BackPEDOT solar cells with PEDOT:PSS:sorbitol layers of comparable thicknesses for sorbitol concentrations of the precursor dispersion from 0.0 to 7.7 wt.% are fabricated. For the silicon base of the solar cells, wafers with a base resistivity of 0.5 Ωcm and 1.3 Ωcm, respectively, are used. In the second part of this Section, the annealing duration is adjusted to verify whether the cell parameters of BackPEDOT solar cells with 7.7 wt.% sorbitol in the precursor dispersion can be further improved due to the excellent passivation properties. We

demonstrate furthermore, that the series resistance of BackPEDOT solar cells induced by the high sorbitol contents can be reduced by increasing the annealing duration and the maximum cell efficiency can therefore be significantly increased.

5.4.1 Impact of Sorbitol Content of the PEDOT:PSS Precursor Dispersion on Solar Cell Parameters

In the previous Sections, it was demonstrated that the addition of sorbitol to the PEDOT:PSS precursor dispersion increases the transparency of the PEDOT:PSS layer in the long wavelength range. Furthermore, we showed for the first time that also the passivation quality of PEDOT:PSS on silicon surfaces improves by adding sorbitol. On the solar cell level, it hence can be expected that the admixture of sorbitol leads to increased short-circuit current densities J_{sc} as well as to improved open-circuit voltages V_{oc}. BackPEDOT solar cells solar cells with an area of $2 \times 2\,\text{cm}^2$ were manufactured in this work according to the process flow shown in Section 4.3. The PEDOT:PSS precursor dispersion is mixed with different contents of sorbitol and stirred overnight on a magnetic stirrer. The PEDOT:PSS application is performed with a spin coating procedure of 10 s at a spin coating speed of 500 rpm and 30 s at 12000 rpm. The PEDOT:PSS:sorbitol layer is then annealed at 130°C for 10 min on a hotplate in ambient environment. Table

Table 5.7: Mean PEDOT:PSS:sorbitol layer thicknesses d and total sheet resistances R_{sheet} for PEDOT:PSS:sorbitol application at a spin coating speed of $\omega = 12000$ rpm.

Sorbitol content in the PEDOT:PSS precursor dispersion c_{sorb} [wt.%]	PEDOT:PSS layer thickness d [nm]	Total sheet resistance $R_{sheet}[\Omega/\square]$
0.0 (6 solar cells)	181 ± 60	2518 ± 252
1.0 (7 solar cells)	140 ± 36	2056 ± 201
2.0 (6 solar cells)	146 ± 32	2083 ± 268
4.0 (7 solar cells)	162 ± 41	435 ± 46
5.7 (9 solar cells)	163 ± 39	304 ± 35
7.7 (7 solar cells)	184 ± 55	274 ± 28

5.7 shows the PEDOT:PSS:sorbitol layer thicknesses d as a function of the sorbitol concentration c_{sorb} of the precursor dispersion. The PEDOT:PSS:sorbitol layer

thickness is the median value over a $2 \times 2\,\mathrm{cm}^2$ area of a test sample. The error bars represent the deviation from the median value and are an indication of the inhomogeneity of the PEDOT:PSS:sorbitol layer over the entire sample. PEDOT:PSS thickness measurements were performed at 1 mm intervals over a length of 2 cm (20 data points) centered over the sample center using a profilometer (Dektak 150, Veeco). The measured layer thicknesses are in the range of 140 to 180 nm and are therefore comparable for the different sorbitol contents of the PEDOT:PSS precursor dispersion. Table 5.7 also shows the measured sheet resistances R_{sheet} for the PEDOT:PSS:sorbitol layers. It is noticeable that the sheet resistances for PE-DOT:PSS:sorbitol films for sorbitol concentrations of less than 4.0 wt.% are over $2000\,\Omega/\square$. If the sorbitol concentration is further increased, the sheet resistance decreases to below $500\,\Omega/\square$. This again shows that sorbitol serves as a conductivity additive in PEDOT:PSS[99, 100]. The J_{sc}-V_{oc} characteristics of the solar cells as well as the illuminated current-voltage (J-V) curves are measured under standard testing conditions at 1 sun and 25°C using a LOANA measurement system (LOANA, PV-Tools Hamelin). The series resistance R_{s} is determined from the measured fill factor FF, pseudo-fill factor pFF as well as the measured J_{sc} and V_{oc} values using the equation:

$$FF = pFF \left(1 - \left(\frac{R_{\mathrm{s}} J_{\mathrm{sc}}}{V_{\mathrm{oc}}} \right) \right). \tag{5.3}$$

Figure 5.12a shows the measured J_{sc} values of each processed BackPEDOT solar cell as a function of the sorbitol concentration c_{sorb} of the PEDOT:PSS precursor dispersion. The median parameters of the solar cells with $0.5\,\Omega$cm and $1.3\,\Omega$cm base resistivity are shown in Table 5.7. It is immediately apparent, that solar cells on 1.3-Ωcm base material provide higher J_{sc} values compared to solar cells fabricated on 0.5-Ωcm base material, which can be attributed to the much higher bulk lifetime in the silicon material with lower doping concentration. Lifetime measurements performed on the 0.5-Ωcm p-type FZ-Si material verified that the bulk lifetime of this material is (0.68 ± 0.07) ms (average value of five measured samples), whereas that of the 1.3-Ωcm material is (1.33 ± 0.32) ms (average value of three measured samples) at an excess carrier concentration Δn of $3\cdot10^{15}\,\mathrm{cm}^3$. For both base materials, the addition of sorbitol to PEDOT:PSS is positively affecting the J_{sc} value. For the 0.5-Ωcm material, the median J_{sc} increases by $0.9\,\mathrm{mA/cm}^2$ by adding a sorbitol concentration of $c_{\mathrm{sorb}} = 4.0$ wt.% to the PEDOT:PSS precursor dispersion. At higher sorbitol contents of $c_{\mathrm{sorb}} = 7.7$ wt.%, the median J_{sc} value increases even by $1.1\,\mathrm{mA/cm}^2$ compared to the reference solar cells without addi-
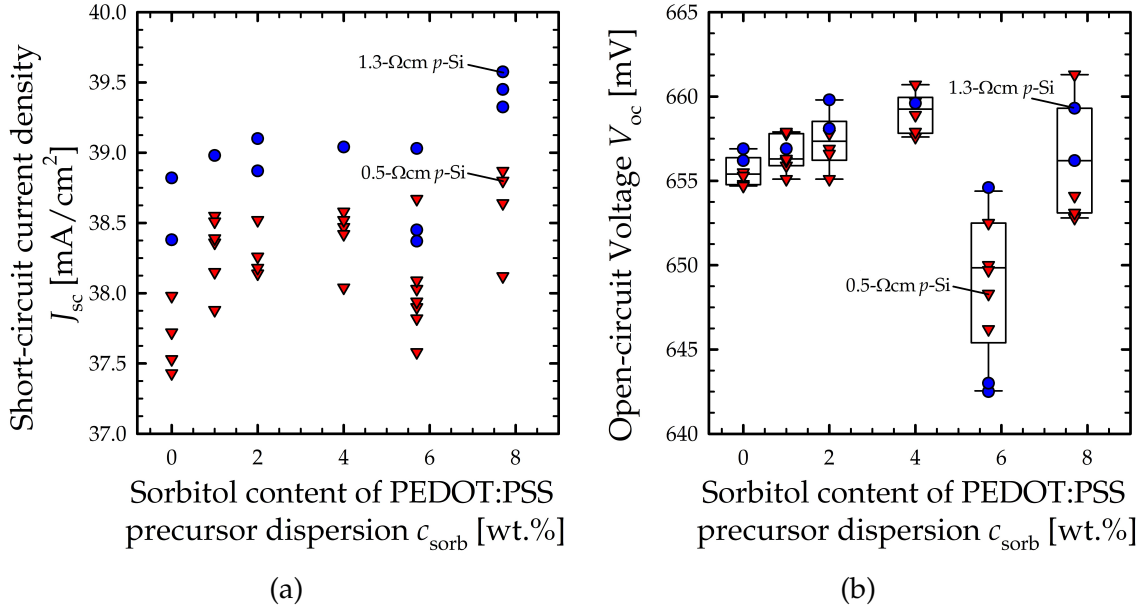
Figure 5.12: (a) Measured short-circuit current density J_{sc} of the fabricated BackPEDOT solar cells for different sorbitol contents of the PEDOT:PSS precursor dispersion. (b) Measured open-circuit voltages V_{oc} of the fabricated solar cells for different sorbitol contents of the PEDOT:PSS precursor dispersion. Solar cells have been fabricated on p-type silicon wafers with a base resistivity of 0.5 Ωcm (red triangles) and 1.3 Ωcm (blue circles), respectively. The V_{oc} values of solar cells with 0.5-Ωcm, as well as with 1.3-Ωcm base material are summarized as a box plot for each investigated sorbitol content of the precursor dispersion.

tion of sorbitol. For the BackPEDOT cells fabricated on the 1.3-Ωcm p-type FZ-Si material, the median J_{sc} increases by $0.9\,\mathrm{mA/cm^2}$ for a sorbitol concentration of 7.7 wt.% compared to the reference without sorbitol. In this cell batch, the highest measured J_{sc} on a BackPEDOT solar cell with a base resistivity of 1.3 Ωcm is $39.6\,\mathrm{mA/cm^2}$ for a sorbitol content of $c_{sorb} = 7.7$ wt.% of the PEDOT:PSS precursor dispersion. The addition of sorbitol to the PEDOT:PSS precursor dispersion effectively reduces the parasitic absorption losses in BackPEDOT solar cells. As can be seen from Figure 5.12b and Table 5.9, the V_{oc} value increases from a median value of 657 mV to 661 mV by adding 4.0 wt.% of sorbitol to the PEDOT:PSS precursor dispersion. At a sorbitol concentration of $c_{sorb} = 5.7$ wt.%, the median V_{oc} value decreases to 650 mV. While the improvement in V_{oc} by the admixture of up to 4.0 wt.% of sorbitol is in good agreement with the lifetime study shown in Figure 5.9, the reduced V_{oc} value at $c_{sorb} = 5.7$ wt.% is unexpected, but seems to be reproducible, as it was observed in all eight cell batches processed within this work. While the PEDOT:PSS:sorbitol dispersions are prepared the

Table 5.8: Maximum and median J_{sc} values for different sorbitol contents of the PEDOT:PSS precursor dispersion of solar cells with 0.5-Ωcm and 1.3-Ωcm base material.

Sorbitol content in the PEDOT:PSS precursor dispersion c_{sorb} [wt.%]	0.5-Ωcm base material		1.3-Ωcm base material	
	Maximum J_{sc} [mA/cm^2]	Median J_{sc} [mA/cm^2]	Maximum J_{sc} [mA/cm^2]	Median J_{sc} [mA/cm^2]
0.0 (6 solar cells)	38.0	37.6	38.8	38.6
1.0 (7 solar cells)	38.6	38.4	39.0	39.0
2.0 (6 solar cells)	38.5	38.2	39.1	39.0
4.0 (7 solar cells)	38.6	38.5	39.0	39.0
5.7 (9 solar cells)	38.7	37.9	39.0	38.5
7.7 (7 solar cells)	38.9	38.7	39.6	39.5

Table 5.9: Maximum and median V_{oc} values of manufactured solar cells for different sorbitol contents of the PEDOT:PSS precursor dispersion.

Sorbitol content in the PEDOT:PSS precursor dispersion c_{sorb} [wt.%]	Maximum V_{oc} [mV]	Median V_{oc} [mV]
0.0 (6 solar cells)	657	655
1.0 (7 solar cells)	658	656
2.0 (6 solar cells)	660	657
4.0 (7 solar cells)	661	659
5.7 (9 solar cells)	655	650
7.7 (7 solar cells)	661	656

day before application and stirred overnight on a magnetic stirrer, the dispersion with a sorbitol content of $c_{sorb} = 5.7$ wt.% was stored at reduced room temperature for a slightly longer period and was reused after renewed stirring on the magnetic stirrer. This could explain the lower median V_{oc} value for this sorbitol content. Increasing the sorbitol content further to $c_{sorb} = 7.7$ wt.% increases the

median V_{oc} approximately back to the state without sorbitol admixture. Nevertheless, the maximum V_{oc} value of a single cell of $V_{oc} = 661$ mV was achieved on an 0.5-Ωcm cell with 7.7 wt.% sorbitol admixture. From the experimental results obtained on 42 processed BackPEDOT cells it can be hence concluded that the admixture of sorbitol has a positive impact on the passivation quality of the PEDPOT:PSS/c-Si junction, although not too much of sorbitol should be added. Figure 5.13 shows the measured change in the internal quantum effi-
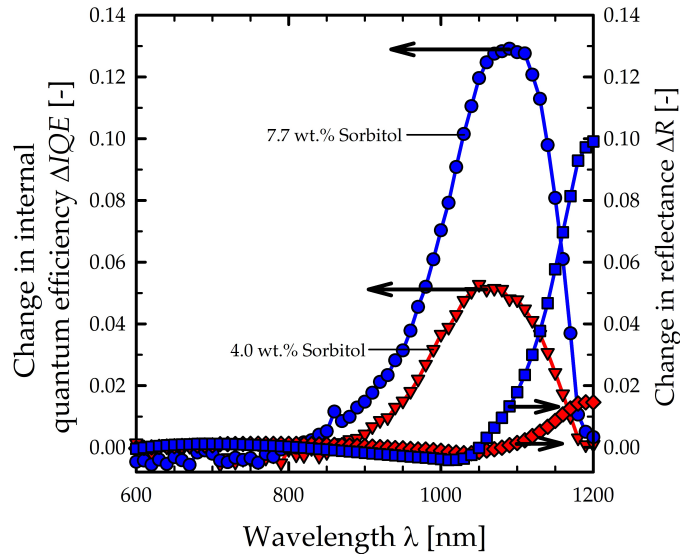
Figure 5.13: Measured change in the internal quantum efficiency (ΔIQE) (blue circles and red triangles) and change in reflectance (blue squares and red diamonds) of exemplary BackPEDOT solar cells by adding 4.0 wt.% (red symbols) and 7.7 wt.% (blue symbols) sorbitol compared to a BackPEDOT solar cell without sorbitol.

ciencies ΔIQE and the change in the reflectance spectra ΔR using the LOANA measurement system (LOANA, PV-Tools) of two exemplary BackPEDOT solar cells for sorbitol contents in the precursor dispersion of 4.0 and 7.7 wt.%, respectively, in comparison to a solar cell without sorbitol in the precursor dispersion. The solar cells have a p-type c-Si base with a resistivity of 0.5 Ωcm and the PEDOT:PSS was spin-coated at 500 rpm for 10 s and subsequently at 12000 rpm for 30 s. The long-wavelength reflectance above $\lambda = 1000$ nm is clearly increased by adding the sorbitol to the PEDOT:PSS precursor dispersion in comparison to the solar cell without admixture of sorbitol, which is attributed to the reduced parasitic absorption in the PEDOT:PSS layer. Moreover, ΔIQE is improved in the long-wavelengths range above $\lambda = 800$ nm for the solar cells with sorbitol addition, which is attributed to the improvement in the rear passivation of the BackPEDOT cell and in the improved light trapping due to the reduced parasitic

absorption within the PEDOT:PSS layer. Figure 5.14a and Table 5.10 illustrate the series resistance R_s of the fabricated BackPEDOT solar cells as a function of the sorbitol content in the PEDOT:PSS precursor dispersion. Up to a sorbitol con-

(a)   (b)
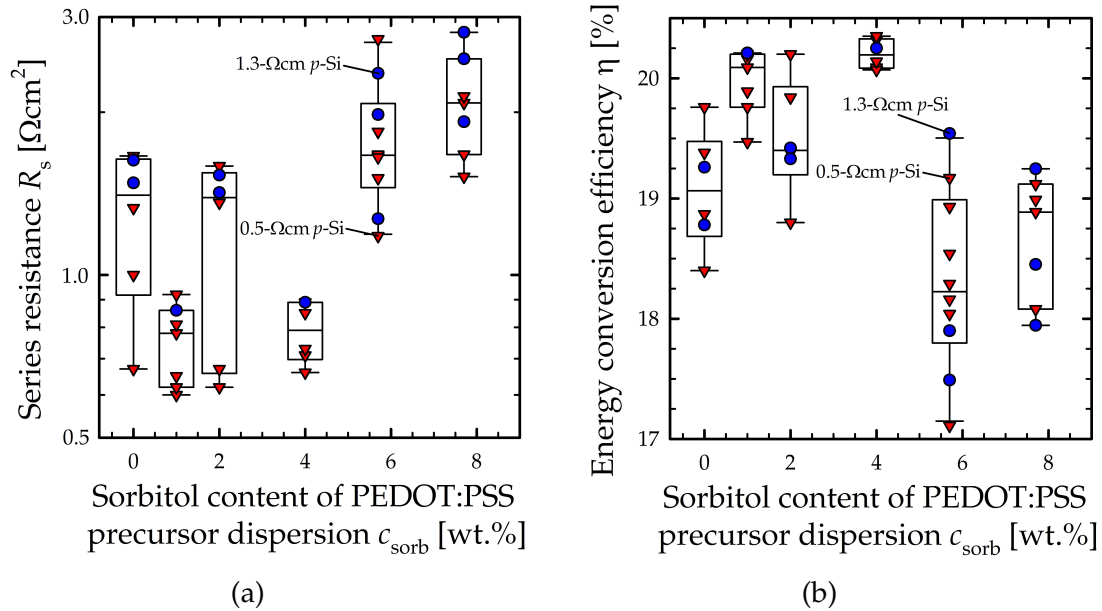
Figure 5.14: (a) Measured series resistance R_s of the fabricated BackPEDOT so-
lar cells for different sorbitol contents of the PEDOT:PSS precursor
dispersion. (b) Measured solar cell efficiency η of the fabricated so-
lar cells for different sorbitol contents of the PEDOT:PSS precursor
dispersion. Solar cells have been fabricated on *p*-type silicon wafers
with a base resistivity of 0.5 Ωcm (red triangles) and 1.3 Ωcm (blue
circles), respectively. The data of solar cells with 0.5-Ωcm, as well as
1.3-Ωcm base material are summarized as a box plot for each sorbitol
content of the precursor dispersion.

(a)   (b)   (c)

Figure 5.15: Light microscopy images of the metallized rear of a solar cell for dif-
ferent sorbitol contens of the PEDOT:PSS precursor dispersion. (a)
0.0 wt.% sorbitol, (b) 4.0 wt.% sorbitol and (c) 7.7 wt.% sorbitol was
added to the precursor dispersion.

Table 5.10: Minimum and median R_s, as well as maximum and median fill factor *FF* values of manufactured solar cells for different sorbitol contents of the PEDOT:PSS precursor dispersion.

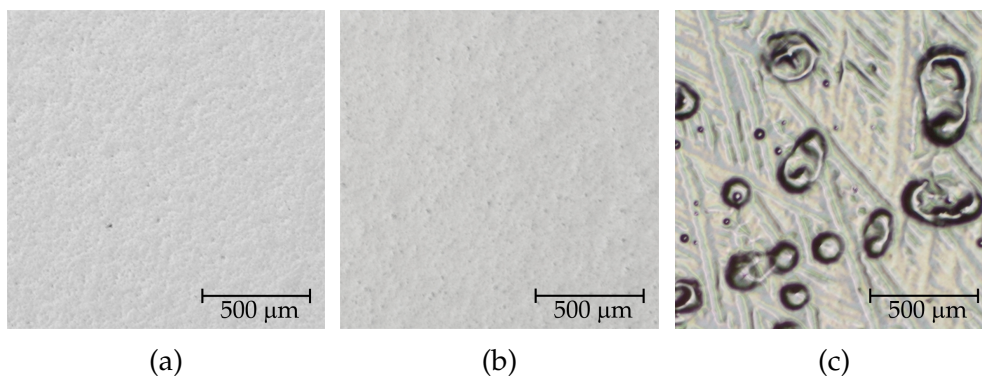| Sorbitol content in the PEDOT:PSS precursor dispersion c_{sorb} [wt.%]	Minimum R_s [Ωcm^2]	Median R_s [Ωcm^2]	Maximum *FF* [%]	Median *FF* [%]
0.0 (6 solar cells)	0.67	1.41	79.4	76.2
1.0 (7 solar cells)	0.60	0.78	80.7	79.5
2.0 (6 solar cells)	0.62	1.39	80.6	76.1
4.0 (7 solar cells)	0.66	0.79	80.3	79.6
5.7 (9 solar cells)	2.73	1.67	77.8	74.4
7.7 (7 solar cells)	2.81	2.08	75.3	73.6

centration of $c_{sorb} = 4.0$ wt.% the best R_s values remain at a constantly low level of approximately 0.6 to 1.0 Ωcm^2. However, there are also outliers with increased series resistance up to values around 1.50 Ωcm^2. At higher sorbitol contents, R_s shows a pronounced increase with increasing sorbitol content. Median R_s values are $R_s = 1.67$ Ωcm^2 for a sorbitol content of $c_{sorb} = 5.7$ wt.% and $R_s = 2.08$ Ωcm^2 for a sorbitol content of $c_{sorb} = 7.7$ wt.%. We attribute the increase in the R_s values for sorbitol contents greater than 4.0 wt.% to a degradation of the solar cell back contact due to the high thermal energy of the electron beam evaporation in combination with a presumably remaining sorbitol content in the PEDOT:PSS layer. Optical microscopy images of the metallized cell rear for the different sorbitol concentrations are shown in Figure 5.15. In the cell manufacturing process, the rear side of the solar cells is metallized by means of electron beam evaporation. Silver is evaporated at a rate of less than 1 nm/s on the solar cell rear. During metallization, water, which is bound by sorbitol due to its hygroscopic properties[117], seems to evaporate due to the heat input. This can be seen as bubble formation of the silver layer on top of the PEDOT:PSS:sorbitol layer. This phenomenon is called blistering. Figure 5.15c shows blistering of the metal layer. It is therefore also conceivable that blistering may occur within the PEDOT:PSS layer, which makes the PEDOT:PSS layer more porous and thus also changes the electrical properties. The charge carrier transport could be affected by the changed morphology which could explain the increase in R_s of the solar cells with high sorbitol contents. The blistering depends on the sorbitol content of the PEDOT:PSS

Table 5.11: Maximum and median η values of manufactured solar cells for different sorbitol contents of the PEDOT:PSS precursor dispersion.

Sorbitol content in the PEDOT:PSS precursor dispersion c_{sorb} [wt.%]	Maximum η [%]	Median η [%]
0.0 (6 solar cells)	19.8	19.1
1.0 (7 solar cells)	20.2	20.1
2.0 (6 solar cells)	20.2	19.4
4.0 (7 solar cells)	20.4	20.2
5.7 (9 solar cells)	19.5	18.2
7.7 (7 solar cells)	19.3	18.9

precursor dispersion. While for PEDOT:PSS layers without sorbitol addition no blistering was observed, for a sorbitol content of $c_{\text{sorb}} = 7.7$ wt.%, blistering was clearly observed, as shown in Figure 5.15. In addition to blistering, a kind of elongated crystal growth or structuring of the metallized PEDOT:PSS surface can be observed. No blistering is observed at lower sorbitol contents, but the metallized rear of the sample with $c_{\text{sorb}} = 4.0$ wt.% sorbitol in Figure 5.15b seems to be a little more coarse-pored than the sample without sorbitol. The amount of sorbitol remaining in the PEDOT:PSS layer is probably higher for sorbitol contents greater 4.0 wt.% than for lower sorbitol concentrations. Therefore, we observe an increase in R_{s} only at high sorbitol concentrations. The best R_{s} value realized on a solar cell processed in this study is $R_{\text{s}} = 0.6\,\Omega\text{cm}^2$ for a sorbitol concentration of $c_{\text{sorb}} = 1.0$ wt.%, which led to an energy conversion efficiency of $\eta = 20.2\%$. The achieved energy conversion efficiencies of all fabricated BackPEDOT solar cells as a function of the sorbitol concentration are shown in Figure 5.14b and in Table 5.11. For BackPEDOT solar cells manufactured with the PEDOT:PSS dispersion without addition of sorbitol, the efficiencies range from 18.4 to 19.7%. By adding a sorbitol content to the precursor dispersion of up to $c_{\text{sorb}} = 4.0$ wt.%, higher cell efficiencies of up to $\eta = 20.4\%$ are achieved. If a sorbitol content of more than 4.0 wt.% is added to the precursor dispersion, the cell efficiencies decrease and range from 17.9% to 19.3% at a sorbitol content of $c_{\text{sorb}} = 7.7$ wt.%. The decrease in the solar cell efficiency with increasing sorbitol content for $c_{\text{sorb}} > 4.0$ wt.% is attributed to the increasing R_{s} value. The best efficiency in Figure 5.14b is $\eta = 20.4\%$ with a sorbitol content in the precursor dispersion of $c_{\text{sorb}} = 4.0$ wt.%.

The illuminated *J–V* curve and the J_{sc}– V_{oc} curve of the best solar cell of this
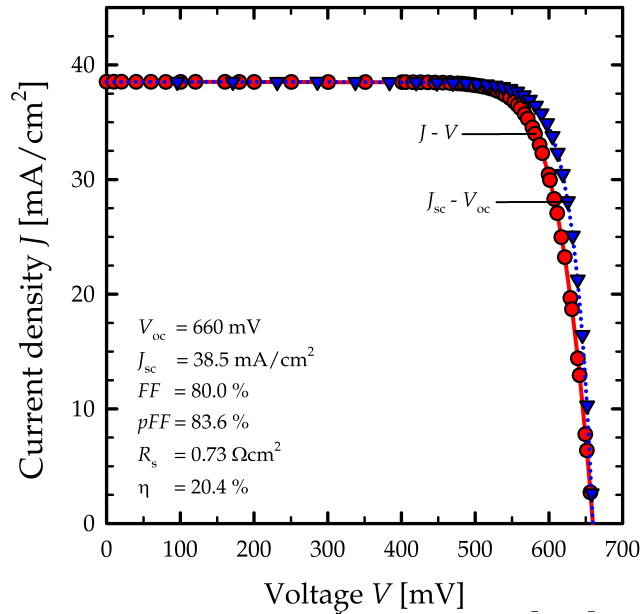
Figure 5.16: Illuminated *J–V* curve (red circles) and J_{sc}– V_{oc} curve (blue triangles) of the 20.4% efficiency BackPEDOT cell with 4.0 wt.% admixture of sorbitol to the PEDOT:PSS precursor dispersion. The corresponding solar cell parameters are also shown.

study with the corresponding solar cell parameters is shown in Figure 5.16. The best BackPEDOT solar cell provides a open-circuit voltage of $V_{oc} = 660$ mV and a short-circuit current density of $J_{sc} = 38.5$ mA/cm^2. A good fill factor of $FF = 80.0\%$ is achieved due to the low series resistance of $R_s = 0.73$ Ωcm^2. This combination of cell parameters leads to an efficiency of $\eta = 20.4\%$. The short-circuit current density of $J_{sc} = 38.5$ mA/cm^2 achieved on this cell seems relatively low and higher J_{sc} values up to 39.6 mA/cm^2 were achieved on the 1.3-Ωcm *p*-Si base material, featuring a much higher bulk lifetime compared to the 0.5-Ωcm base material. Hence, there seems to be a strong contribution of the bulk recombination in the 20.4% efficiency cell, bulk material with higher lifetimes can be used for further efficiency improvement.

5.4.2 Impact of Annealing Duration

In Section 5.4.1 we showed, that in order to achieve the highest possible J_{sc} values, a high sorbitol admixture of $c_{sorb} = 7.7$ wt.% is necessary. However, a high sorbitol addition increases the probability that the series resistance of the solar cell

will deteriorate significantly. In Figure 5.8, the specific contact resistance ρ_{PEDOT} of the c-Si/PEDOT:PSS:sorbitol/Ag junction was examined for a sorbitol concentration of $c_{sorb} = 7.7$ wt.% as a function of different annealing durations at 130°C. It was shown, that longer annealing durations can have a positive effect on the contact resistance of the c-Si/PEDOT:PSS:sorbitol/Ag junction. This aspect will be further examined in this Section. BackPEDOT solar cells with 1.3-Ωcm p-type FZ-Si base are fabricated. 7.7wt.% sorbitol is added to the PEDOT:PSS precursor dispersion and the PEDOT:PSS:sorbitol layer is then annealed for various periods of time on a hotplate at 130°C in ambient environment. The J_{sc} values of the manufactured solar cells are shown in Figure 5.17a and in Table 5.12 for different annealing durations. The median J_{sc} values are within a range between 37.6 and 38.4 mA/cm^2 for all investigated annealing durations. Hence, we con-

(a) (b)

Figure 5.17: (a) Measured short-circuit current density J_{sc} of the fabricated BackPEDOT solar cells for different annealing durations. (b) Measured open-circuit voltages V_{oc} of the fabricated solar cells for different annealing durations. The J_{sc} and V_{oc} values are summarized as a box plot for each investigated annealing duration. 7.7 wt.% sorbitol is admixed to the PEDOT:PSS precursor dispersion and the annealing temperature is set to 130°C.

clude that there is no relevant dependence of the J_{sc} values on the annealing duration. The extended annealing time should here not affect the parasitic absorption in the PEDOT:PSS:sorbitol layer. The best short-circuit current density value achieved in Figure 5.17a is $J_{sc} = 39.6$ mA/cm^2. Measured V_{oc} values for different annealing durations of the fabricated solar cells are shown in Figure 5.17b. The median parameters and the best achieved values of the solar cells are shown in

Table 5.12: Maximum and median J_{sc}, as well as maximum and V_{oc} values of solar cells for different annealing durations at 130°C in ambient environment.

Annealing duration t [min]	Maximum J_{sc} [mA/cm^2]	Median J_{sc} [mA/cm^2]	Maximum V_{oc} [mV]	Median V_{oc} [mV]
10 (38 solar cells)	39.6	38.1	662	655
30 (9 solar cells)	39.4	38.5	661	658
45 (6 solar cells)	38.2	37.8	664	660
60 (36 solar cells)	38.9	37.6	667	654
90 (5 solar cells)	39.5	38.4	659	650
120 (8 solar cells)	38.8	38.2	657	644

Table 5.12. For an annealing duration of $t = 10$ min, the median open-circuit voltage is $V_{oc} = 655$ mV. For longer annealing durations up to 45 min the median V_{oc} value increases to $V_{oc} = 660$ mV. If the annealing time is extended even further, the median open-circuit voltage decreases again to $V_{oc} = 654$ mV for an annealing duration of $t = 60$ min and for an annealing duration of 120 min only a median V_{oc} value of 644 mV is reached. An increase in V_{oc} for annealing durations up to 45 min and a subsequent decrease in V_{oc} for longer annealing durations is consistent with the results of the lifetime samples in Figure 5.10b. Nevertheless, the best achieved open-circuit voltage here is $V_{oc} = 667$ mV for an annealing duration of t = 60 min. Figure 5.18a shows a boxplot of the series resistance R_s of the fabricated BackPEDOT solar cells as a function of the annealing duration t in ambient environment at a temperature of 130°C. The median parameters and the best achieved values of R_s are shown in Table 5.13. The median R_s values range between 1.07 and 2.22 Ωcm^2 for all investigated annealing durations. The median R_s values for annealing durations of 45, 60 and 90 min are close to 1.00 Ωcm^2, while the median R_s values for all other annealing durations are close to 2.00 Ωcm^2. However, the minimum R_s values achieved are below 1.00 Ωcm^2 for all annealing durations. The best achieved R_s value is $R_s = 0.62$ Ωcm^2 for an annealing duration of $t = 60$ min. A possible advantage of the longer annealing duration is also consistent with the specific contact resistance measurements in Figure 4.4a, which show a minimum value of the specific contact resistance for an annealing duration of $t = 90$ min. The achieved efficiencies of the fabricated BackPEDOT solar cells as a function of the annealing duration are shown in Fig-
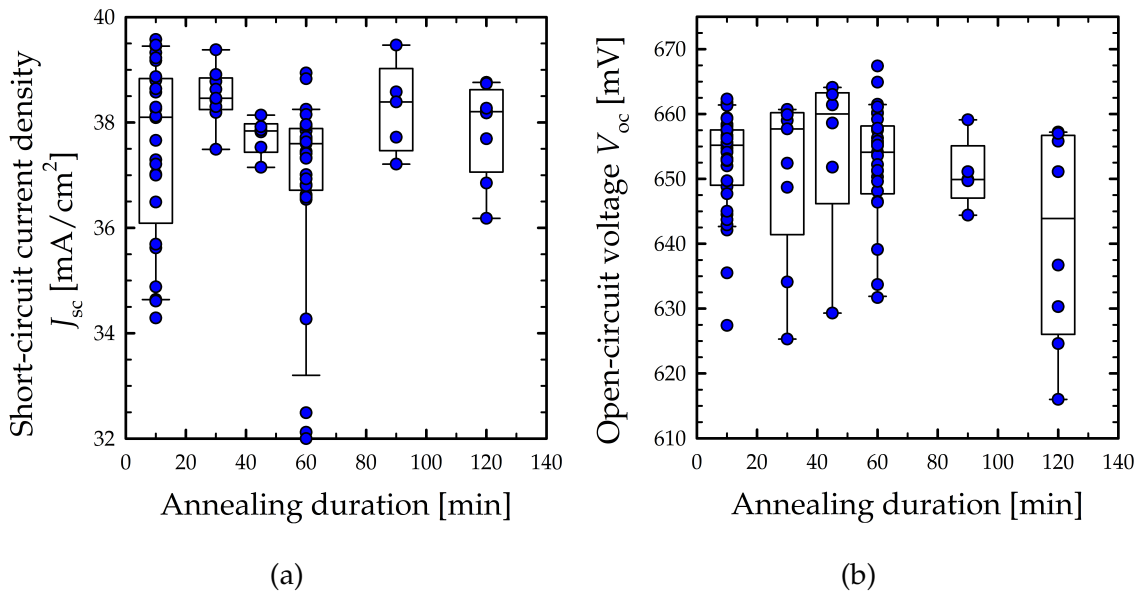
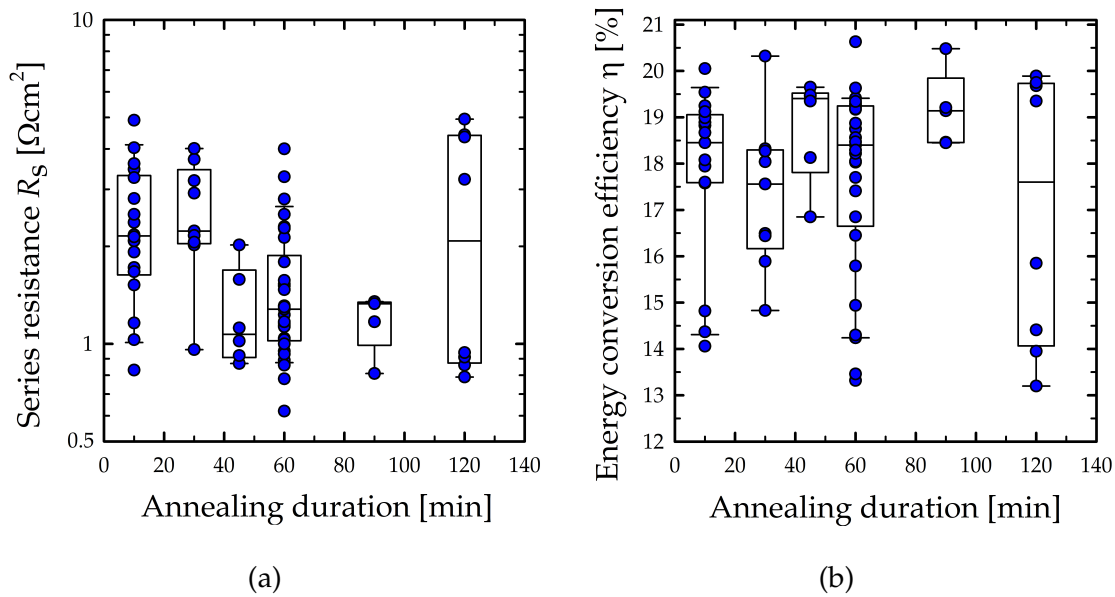(a)   (b)

Figure 5.18: (a) Measured series resistance R_s of the fabricated BackPEDOT so-
lar cells for different annealing durations. (b) Measured solar cell
efficiency η of the fabricated solar cells for different annealing dura-
tions. The R_s and η values are summarized as a box plot for each
investigated annealing duration. 7.7 wt.% sorbitol is admixed to the
PEDOT:PSS precursor dispersion and the annealing temperature is
set to 130°C.

ure 5.18b and Table 5.14. The best efficiencies achieved for each annealing dura-
tion increase from η = 20.1% for an annealing duration of t = 10 min to η = 20.6%
for an annealing duration of t = 60 min. With longer annealing durations, the
maximum achieved efficiencies decrease again to 19.9% for an annealing dura-
tion of t = 120 min. The best median efficiency of η = 19.4% is achieved for an
annealing duration of t = 45 min. However, the best single solar cell provides an
efficiency of η = 20.6% for a annealing duration of t = 60 min. Note that this is
the highest efficiency obtained for a silicon solar cell with PEDOT:PSS as selec-
tive contact. The illuminated $J–V$ curve and the J_{sc}– V_{oc} curve of the champion
solar cell including the corresponding solar cell parameters is shown in Figure
5.19. Our champion BackPEDOT solar cell fabricated with an annealing duration
of t = 60 min provides an open-circuit voltage of V_{oc} = 660 mV and a short-circuit
current density of J_{sc} = 38.9 mA/cm^2. A good fill factor of FF = 80.3% is achieved
due to a series resistance of only R_s = 0.62 Ωcm^2. This combination of cell pa-
rameters leads to the highest efficiency achieved so far for any solar cell with
PEDOT:PSS/c-Si of η = 20.6%. We have checked that the parameters J_{sc}, V_{oc} and
R_s are completely independently of each other by means of correlation of plots. It
is therefore possible to measure the maximum values for each individual param-

Table 5.13: Minimum and median R_s, as well as maximum and median fill factor *FF* values of solar cells for different annealing durations at 130°C in ambient environment.

Annealing duration t [min]	Minimum R_s [Ωcm^2]	Median R_s [Ωcm^2]	Maximum *FF* [%]	Median *FF* [%]
10 (38 solar cells)	0.83	2.16	78.6	72.5
30 (9 solar cells)	0.96	2.23	78.3	70.9
45 (6 solar cells)	0.92	1.07	79.0	77.3
60 (36 solar cells)	0.62	1.28	80.3	75.5
90 (5 solar cells)	0.81	1.33	78.7	76.4
120 (8 solar cells)	0.79	2.08	78.7	71.6

Table 5.14: Maximum and median η values of solar cells for different annealing durations at 130°C in ambient environment.

Annealing duration t [min]	Maximum η [%]	Median η [%]
10 (38 solar cells)	20.1	18.5
30 (9 solar cells)	20.3	17.6
45 (6 solar cells)	19.7	19.4
60 (36 solar cells)	20.6	18.4
90 (5 solar cells)	20.5	19.1
120 (8 solar cells)	19.9	17.6

eter on one solar cell and combine these values. The maximum values achieved in this thesis according to Table 5.12, 5.13 and 5.14 are a open-circuit voltage of $V_{oc} = 667$ mV, a short-circuit current density $J_{sc} = 39.6$ mA/cm^2 and a fill factor of $FF = 80.3\%$. The corresponding efficiency potential is now calculated using the equation,

$$\eta_{max} = \frac{V_{oc,max}\ J_{sc,max}\ FF_{max}}{P_{in}}, \tag{5.4}$$

to estimate the realistic efficiency potential of our BackPEDOT approach, where P_{in} is $P_{in} = 100$ mW/cm^2. According to Equation (5.4) with the given maximum values for J_{sc}, V_{oc} and the fill factor *FF* a maximum attainable energy conversion efficiency for BackPEDOT solar cells with admixture of $c_{sorb} = 7.7$ wt.% sorbitol

The figure shows a graph with Current density J [mA/cm^2] on the y-axis (0 to 40) and Voltage V [mV] on the x-axis (0 to 700). Two curves are labeled J-V and J_{sc}-V_{oc}. Parameters shown:

V_{oc} = 660 mV
J_{sc} = 38.9 mA/cm^2
FF = 80.3 %
pFF = 83.7 %
R_s = 0.62 Ωcm^2
η = 20.6 %
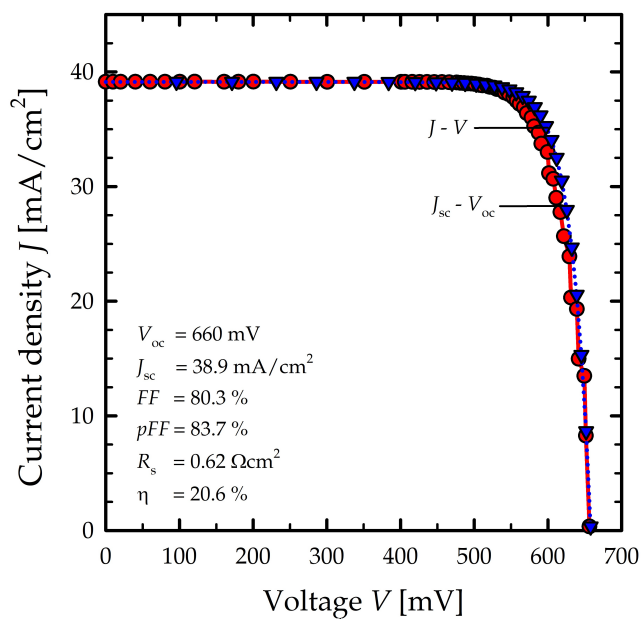
Figure 5.19: Illuminated J–V curve (red circles) and J_{sc}–V_{oc} curve (blue triangles) of our champion BackPEDOT solar cell with 7.7 wt.% admixture of sorbitol to the PEDOT:PSS precursor dispersion and an annealing duration of 60 min at 130°C in ambient environment. The corresponding solar cell parameters are also shown.

to the PEDOT:PSS precursor dispersion of $\eta_{max} = 21.2\%$ is determined, which demonstrates the efficiency potential of our developed BackPEDOT cell.

5.5 Chapter Summary

In this Chapter, we have investigated the impact of additives to the PEDOT:PSS dispersion on the transparency of PEDOT:PSS as well as on the solar cell parameters of BackPEDOT solar cells. Sorbitol was found to be the most promising additive, since the transparency of PEDOT:PSS is significantly improved, while the series resistance of BackPEDOT solar cells remains unaffected. We have shown here for the first time that the recombination current density parameter $J_{0.PEDOT}$ and thus the recombination at the PEDOT:PSS/c-Si junction is effectively suppressed by the addition of sorbitol. We determined the specific contact resistance of the Ag/PEDOT:PSS:sorbitol/c-Si junction in dependence of the sample annealing duration and report here for the first time, that a longer annealing duration of 90 min leads to a reduced specific contact resistance. On BackPEDOT solar cells, the highest achieved J_{sc} value is 39.6 mA/cm^2 for a sorbitol concentration of the PEDOT:PSS precursor dispersion of 7.7 wt.%, which is 0.8 mA/cm^2 higher than the best achieved J_{sc} value without sorbitol admixture. Due to the improvement in the surface passivation quality of PEDOT:PSS with sorbitol admixture, we observe an increase in V_{oc} by 4.0 mV on BackPEDOT solar cells. The highest V_{oc} value of a single solar cell was 667 mV for an annealing duration of 60 min. The lowest R_s of 0.62 Ωcm^2 of a single solar cell was obtained for an annealing duration of 60 min and corresponds to a fill factor of $FF = 80.3\%$. The best energy conversion efficiency of 20.6% of a single solar cell was achieved for an annealing duration of 60 min, which is the highest efficiency ever achieved with PEDOT:PSS on silicon.

6 Depletion Region Modulation Effect at the PEDOT:PSS/c-Si Junction

Depletion region modulation (DRM) is an effect observed in photoconductance based lifetime measurements (Section 3.4) and is caused by a modulation of the depletion region width of the measured silicon sample. The effect is observed in silicon samples with a depletion region, e.g. due to fixed charges within a surface-passivating dielectric layer or due to a *p-n* junction. In this Chapter, we examine whether the DRM effect is also observable on PEDOT:PSS/c-Si junctions and what information can be extracted from it. We fabricate silicon lifetime samples on 300 μm thick (100)-oriented *p*-type FZ-Si wafers with a resistivity of 1.3 Ωcm and on 300 μm thick *n*-type CZ-Si wafers with a resistivity of 1.5 Ωcm. A cross-section of the lifetime samples is shown in Figure 6.1. After RCA cleaning, a 10 nm thick AlO$_x$ layer is deposited by means of plasma-assisted atomic layer deposition (FlexAL, Oxford Instruments) on one wafer surface of the *p*-type silicon wafer. One wafer surface of the *n*-type silicon wafer is passivated by a 100 nm thick plasma-enhanced-chemical-vapor-deposited (PECVD) SiN$_y$ layer (Plasmalab 80 Plus, Oxford Instruments) with a refractive index *n* of $n = 2.4$ (at a wavelength of $\lambda = 633$ nm) at a deposition temperature of 400°C, which is also used on the *p*-type wafer as an AlO$_x$ capping layer. The *p*-type wafers are thermally annealed on a hotplate at 425°C for 15 min to activate the AlO$_x$ passivation. Then, the samples are dipped in 1% hydrofluoric acid (HF) for 60 seconds. Immediately after the HF dip, the PEDOT:PSS dispersion (CleviosTM, Heraeus Deutschland GmbH) is deposited by spin coating (WS-650Mz-8NPPB/UD3, Laurell Technologies). The PEDOT:PSS application is performed with a spin coating procedure of 10 s at a spin coating speed of 500 rpm and 30 s at 1500 rpm. Subsequently, the PEDOT:PSS layer is annealed on a hotplate for 10 min at 130°C in ambient environment. Injection-dependent measurements of the carrier lifetime are performed using a Sinton Lifetime Tester (WCT-120, Sinton Instruments). In

Figure 6.1, apparent lifetime τ_{app} curves in dependence of the excess carrier concentration Δn (for p-type silicon) or Δp (for n-type silicon), obtained by quasi steady-state (QSSPC) photoconductance technique, are shown. The apparent
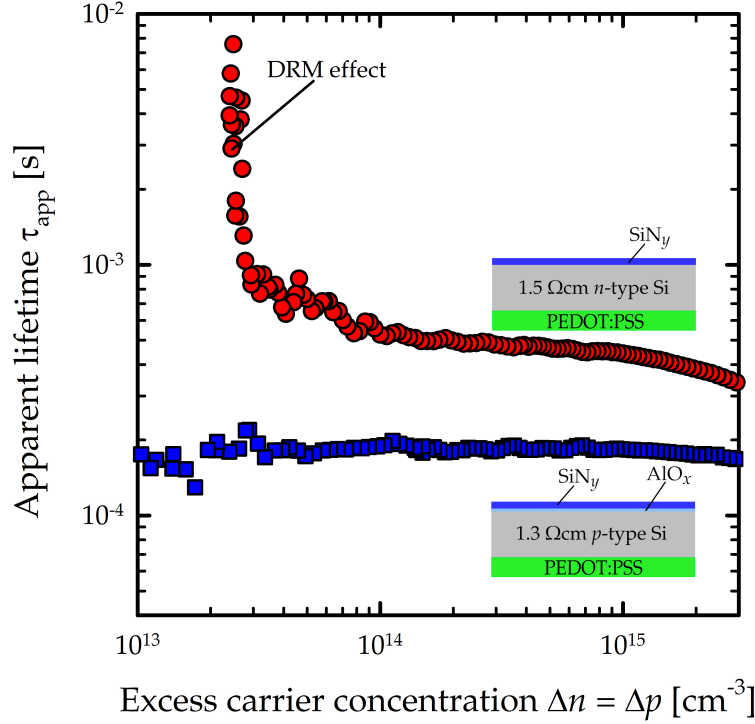

Figure 6.1: Apparent lifetime curves of 1.5-Ωcm n-type-Si wafers passivated with PEDOT:PSS and SiN$_y$ (red circles) and 1.3-Ωcm p-type-Si passivated with PEDOT:PSS and an AlO$_x$/SiN$_y$ layer stack (blue squares).

lifetime τ_{app} of the p-type silicon wafer in Figure 6.1 is approximately constant over the investigated Δn range. In contrast, the 1.5-Ωcm n-type Si wafer shows a strong increase in the apparent lifetime τ_{app} for decreasing Δp values below $\sim 10^{14}\,\mathrm{cm}^{-3}$. We attribute this steep increase in lifetime in low injection densities to the DRM effect. PEDOT:PSS, due to its work function of $5.2\,\mathrm{eV}$[75], induces a band bending in the n-type silicon which causes an accumulation of the minority carriers at the surface and thus creates a depletion region at the PEDOT:PSS/n-Si junction. In order to model the observed lifetime increase in low injection densities, we treat the PEDOT:PSS layer in the same way as a passivating dielectric layer with a fixed negative charge density, resulting in the same kind of depletion region at the silicon surface. In our model, we not only include the change in photoconductance during quasi steady-state measurements, but also the change in the additional conductance caused by the depletion region modulation at the PEDOT:PSS/n-Si junction. A detailed description of our model can be found

in Section 3.5. By fitting the measured apparent lifetime curves $\tau_{\mathrm{app}}(\Delta p)$ with the simulated apparent lifetimes, we are able to determine the band bending Ψ_{s} induced by PEDOT:PSS at the interface in n-type silicon. Figure 6.2 shows exemplary measured lifetime curves for n-type silicon wafers with PEDOT:PSS/n-Si junction as a function of Δp. The measured apparent lifetime τ_{app} of a reference silicon wafer passivated on both sides with SiN$_y$ is also shown in Figure 6.2. The
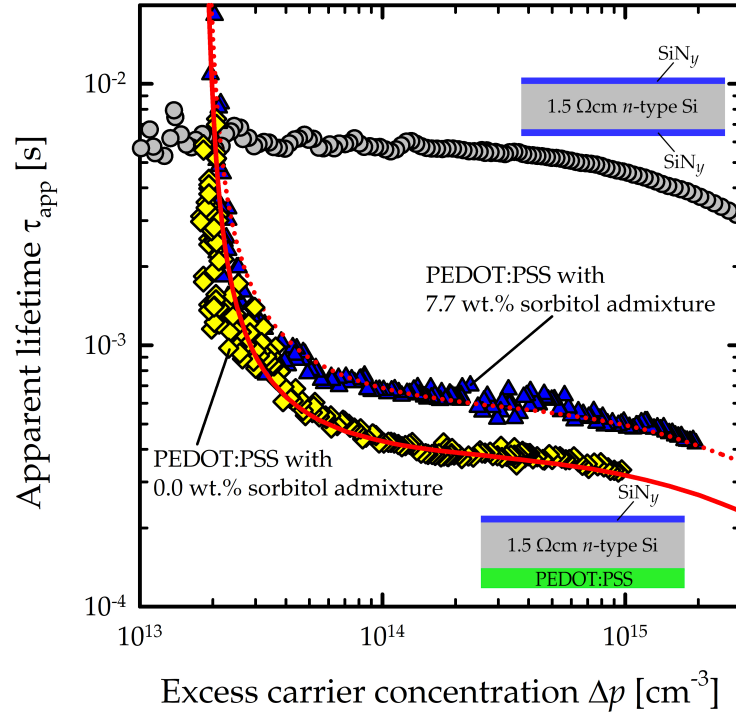
Figure 6.2: Experimental (symbols) and fitted (lines) apparent lifetime curves of 1.5-Ωcm n-type-Si wafers passivated with PEDOT:PSS and SiN$_y$. The resulting interface parameters are shown in Table 6.1.

apparent lifetime in Figure 6.2 of the n-type silicon wafer passivated on both sides with SiN$_y$ shows no DRM effect. The apparent lifetime curves for the n-type silicon wafers with PEDOT:PSS/n-Si junction clearly show the DRM effect for Δp values below $\sim 10^{14}$ cm^{-3}. We examine here a PEDOT:PSS dispersion without and with 7.7 wt.% sorbitol addition. The addition of 7.7 wt.% sorbitol to the PEDOT:PSS precursor dispersion leads to a higher apparent lifetime for Δp values larger than $\sim 4 \times 10^{13}$ cm^{-3}. In Chapter 5.3, the addition of sorbitol to the PEDOT:PSS precursor dispersion already showed a positive impact on the passivation quality of p-type silicon surfaces with PEDOT:PSS. The fact that the addition of sorbitol improves the passivation quality of PEDOT:PSS is confirmed here on n-type silicon. For excess carrier densities below $\sim 4 \times 10^{13}$ cm^{-3}, however, there

is no difference in DRM-affected $\tau_{app}(\Delta p)$ lifetime curves, if sorbitol is added. With a simulation of the $\tau_{app}(\Delta p)$ dependence as explained in Section 3.5 and a fit of our experimental data shown in Figure 6.2 (red lines), we can determine the band bending Ψ_s in the *n*-type silicon samples and the surface recombination velocity parameter $S_{p0} = S_{n0}$ of the PEDOT:PSS/*n*-Si junction. A fit was performed for four samples without sorbitol addition and for 7.7 wt.% sorbitol addition. The averaged values of the band bending Ψ_s and the S_{p0} values are summarized in Table 6.1. The uncertainties indicates the deviation from the mean values. Due to the sign convention, a band bending Ψ_s, which leads to an accumulation of holes, is described as negative. Based on modeling the DRM effect we have, for the first

Table 6.1: Interface parameters Ψ_s and $S_{p0} = S_{n0}$, determined by fitting the experimental data shown in Figure 6.2.

Sorbitol content of PEDOT:PSS dispersion c_{sorb} [wt.%]	Band bending in 1.5-Ωcm *n*-type silicon Ψ_s [meV]	Surface recombination velocity parameter $S_{p0} = S_{n0}$ [cm s^{-1}]
0.0 (4 samples)	$-(720 \pm 9)$	$2.2 \times 10^3 \pm 0.2 \times 10^2$
7.7 (4 samples)	$-(714 \pm 6)$	$1.5 \times 10^3 \pm 0.1 \times 10^2$

time, extracted the band bending Ψ_s induced by PEDOT:PSS on *n*-type silicon. Figure 6.3 shows the electronic band structure in an *n*-type silicon wafer with a doping concentration of $N_D = 3.2 \times 10^{15}$ cm^{-3}. Our extracted value for the band bending Ψ_s, based on modeling the DRM effect, is shown in green. The Fermi energy of intrinsic silicon E_i (grey), the band gap of silicon E_g (orange) and the Fermi energy E_f according to Equation (3.12) (blue) are also shown. Jäckle et al. had determined the band bending Ψ_s on PEDOT:PSS coated *n*-type silicon for a doping concentration of 1.5×10^{15} cm^{-3}, which is in the same order of magnitude as the doping concentration of the *n*-type wafers used in this study (3.2×10^{15} cm^{-3}), Jäckle et al. determined a value of Ψ_s of -712 meV[64] and -690 meV[123] for the PEDOT:PSS/*n*-Si junction by means of capacitance-voltage (C-V) measurements. Wan et al.[124] also reported a band bending of -716 meV at the PEDOT:PSS/*n*-Si junction measured by C-V measurements. Wang et al.[125] report a band bending for the PEDOT:PSS/*n*-Si junction of -710 meV determined by X-ray photoelectron spectroscopy (XPS) and ultraviolet photoelectron spectroscopy (UPS). Within the range of the measurement uncertainties, the band bending Ψ_s determined by our newly introduced methodology based on the DRM effect is in
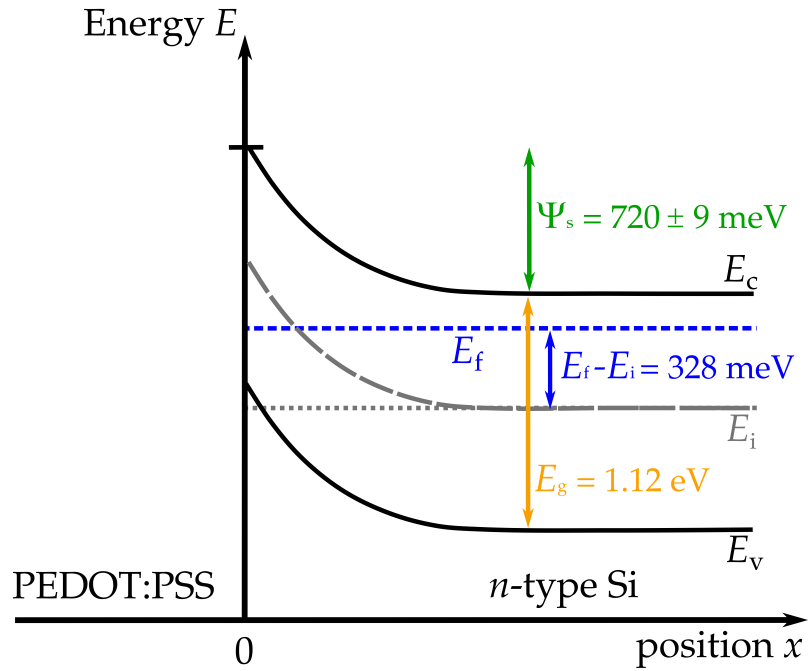
Figure 6.3: Schematic of the electronic band structure in an n-type silicon wafer with a doping concentration of N_D=3.2×10^{15} cm^{-3}. Our extracted value for the band bending Ψ_s, based on modeling the DRM effect, is shown in green.

excellent agreement with the Ψ_s values reported in the literature. Interestingly, within the measurement uncertainty, we do not observe any impact of sorbitol admixture to PEDOT:PSS on Ψ_s. However, the addition of sorbitol improves the chemical interface passivation, as demonstrated by a reduction of the S_{p0} value by 31%.

6.1 Chapter Summary

In this Chapter, we have shown that lifetime curves obtained from quasi-steady-state photoconductance (QSSPC) measurements on n-type silicon wafers, coated with PEDOT:PSS, show a drastic increase in the measured apparent lifetime with decreasing injection density Δn. We attribute this increase to the depletion region modulation (DRM) effect, known from silicon wafers passivated by dielectric layers with fixed charges and p-n-junctions[64]. Injection-dependent lifetime curves $\tau_{\mathrm{app}}(\Delta p)$ of PEDOT:PSS coated p-type silicon wafers did not show any DRM effect. We have modelled the $\tau_{\mathrm{app}}(\Delta p)$ curves including the DRM effect at the PEDOT:PSS/n-Si junction. By modelling the measured $\tau_{\mathrm{app}}(\Delta p)$ curves, we have determined the band bending Ψ_{s} induced by PEDOT:PSS on silicon. The determined value for the band bending Ψ_{s} of $-(720 \pm 9)\,\mathrm{meV}$ is in good agreement with values reported in the literature for the PEDOT:PSS/c-Si junction obtained from capacitance-voltage (C-V) measurements, X-ray photoelectron spectroscopy (XPS) and ultraviolet photoelectron spectroscopy (UPS). Our newly introduced methodology to determine Ψ_{s} from injection dependent lifetime measurements was hence shown to be well suitable. We also examined the impact of adding sorbitol to the PEDOT:PSS dispersion on the DRM effect. Within the measurement uncertainty we do not observe any impact of the sorbitol admixture to PEDOT:PSS on the band bending Ψ_{s}. The surface recombination velocity parameter, however, decreased significantly by the admixture of sorbitol. Hence, we conclude that the admixture of sorbitol to PEDOT:PSS improves the chemical interface passivation of the PEDOT:PSS/c-Si junction, but leaves the band bending within the silicon bulk unchanged.

7 Summary

In this thesis, we have successfully implemented PEDOT:PSS into BackPEDOT solar cells. We showed, that the passivation of planar silicon surfaces with PEDOT:PSS exhibits a pronounced dependence of the PEDOT:PSS layer thickness. The passivation quality of PEDOT:PSS decreases with decreasing PEDOT:PSS layer thickness. On fabricated BackPEDOT solar cells, we demonstrated that J_{sc} increases with decreasing thickness of the PEDOT:PSS layer, but the open-circuit voltage V_{oc} decreases due to the detoriation of the passivation quality of thin PEDOT:PSS films on c-Si. On random-pyramid textured silicon surfaces covered with PEDOT:PSS we detected for the first time, a thin organic layer in the valleys between the pyramids of the silicon surface beneath the deposited PEDOT:PSS layer. We measured a different atomic composition of the thin organic layer in comparison to the PEDOT:PSS layer on top and concluded, that the thin PEDOT:PSS layer is probably responsible for the passivation of textured Si surfaces with PEDOT:PSS and that an increased sulfur content has a positive impact on the surface passivation properties. In addition, we have examined the impact of additives to the PEDOT:PSS dispersion on the transparency of PEDOT:PSS as well as on the solar cell parameters of BackPEDOT solar cells. Sorbitol was found to be the most promising additive, since the transparency of PEDOT:PSS is significantly improved, while the series resistance of BackPEDOT solar cells remains unaffected. We have shown here for the first time that the recombination current density parameter $J_{0,PEDOT}$ and thus the recombination at the PEDOT:PSS/c-Si interface is effectively suppressed by the addition of sorbitol. On BackPEDOT solar cells, the highest achieved J_{sc} value is 39.6 mA/cm^2 for a sorbitol concentration of the PEDOT:PSS precursor dispersion of 7.7 wt.%, which is 0.8 mA/cm^2 higher than the best achieved J_{sc} value without sorbitol admixture. Due to the improvement in the surface passivation quality of PEDOT:PSS with sorbitol admixture, we observe an increase in V_{oc} by 4.0 mV on BackPEDOT solar cells. The best V_{oc} of a single solar cell was 667 mV and the highest energy conversion efficiency of 20.6% of a single solar cell was achieved for an annealing duration of 60 min, which is the highest efficiency ever achieved with PEDOT:PSS on silicon. In ad-

dition, we have shown that lifetime curves obtained from quasi-steady-state photoconductance (QSSPC) measurements on n-type silicon wafers, coated with PEDOT:PSS, show a drastic increase in the measured apparent lifetime with decreasing injection density Δn. We attribute this increase to the depletion region modulation (DRM) effect. We have modelled the $\tau_{\mathrm{app}}(\Delta p)$ curves including the DRM effect at the PEDOT:PSS/n-Si junction. By modelling the measured $\tau_{\mathrm{app}}(\Delta p)$ curves, we have determined the band bending Ψ_{s} induced by PEDOT:PSS on silicon. The determined value for the band bending Ψ_{s} of $-(720 \pm 9)\,\mathrm{meV}$ is in good agreement with values reported in the literature for the PEDOT:PSS/c-Si junction applying other measurement techniques. Our newly introduced methodology to determine Ψ_{s} from injection dependent lifetime measurements was hence shown to be well suitable. We also examined the impact of adding sorbitol to the PEDOT:PSS dispersion on the DRM effect. Within the measurement uncertainty, we do not observe any impact of sorbitol admixture to PEDOT:PSS on the band bending Ψ_{s}. The surface recombination velocity parameter, however, decreased significantly by the admixture of sorbitol. Hence, we conclude that the admixture of sorbitol to PEDOT:PSS improves the chemical interface passivation of the PEDOT:PSS/c-Si junction, but leaves the band bending within the silicon bulk unchanged.

Bibliography

[1] M. Lucibella, "Bell labs demonstrates the first practical silicon solar cell," *American Physical Society NEWS*, vol. 18, no. 4, p. 2, 2009.

[2] H. Hannebauer, T. Dullweber, U. Baumann, T. Falcon, and R. Brendel, "21.2%-efficient fineline-printed PERC solar cell with 5 busbar front grid," *Physica Status Solidi-Rapid Research Letters*, vol. 8, no. 8, 2014.

[3] W. Deng, F. Ye, R. Liu, Y. Li, H. Chen, Z. Xiong, Y. Yang, Y. Chen, Y. Wang, P. P. Altermatt, Z. Feng, and P. J. Verlinden, "22.61% efficient fully screen printed PERC solar cell," *Proceedings of 44th IEEE Photovoltaic Specialist Conference (PVSC), Washington*, pp. 2220–2226, 2017.

[4] T. G. Allen, J. Bullock, X. Yang, A. Javey, and S. D. Wolf, "Passivating contacts for crystalline silicon solar cells," *Nature Energy*, vol. 4, pp. 914–928, 2019.

[5] K. Yamamoto, K. Yoshikawa, H. Uzu, and D. Adachi, "High-efficiency heterojunction crystalline Si solar cells," *Japanese Journal of Applied Physics*, vol. 57, no. 08RB20, pp. 1–8, 2018.

[6] J. Schmidt, R. Peibst, and R. Brendel, "Surface passivation of crystalline silicon solar cells: present and future," *Solar Energy Materials and Solar Cells*, vol. 187, pp. 39–54, 2018.

[7] J. Meyer, S. Hamwi, M. Kröger, W. Kowalsky, T. Riedl, and A. Kahn, "Transition metal oxides for organic electronics: energetics, device physics and applications," *Advanced Materials*, vol. 24, pp. 5408–5427, 2012.

[8] A. Elschner, S. Kirchmeyer, W. Lövenich, U. Merker, and K. Reuter, *PEDOT: Principles and Applications of an Intrinsically Conductive Polymer*. Boca Raton, FL: CRC Press. p.113,-158, 2011.

[9] S. Avasthi, S. Lee, Y. L. Loo, and J. C. Sturm, "Role of majority and minority carrier barriers silicon/organic hybrid heterojunction solar cells," *Advanced Materials*, vol. 23, no. 48, pp. 5762–5766, 2011.

[10] L. He, C. Jiang, H. Wan, D. Lai, and Rusli, "High efficiency planar Si/organic heterojunction hybrid solar cells," *Applied Physics Letters*, vol. 100, no. 7, p. 073503, 2012.

[11] J. Schmidt, V. Titova, and D. Zielke, "Organic-silicon heterojunction solar cells: Open-circuit voltage potential and stability," *Applied Physics Letters*, vol. 103, no. 18:183901, 2013.

[12] S. Avasthi, K. A. Nagamatsu, J. Jhaveril, W. E. McClain, G. Man, A. Kahn, J. Schwartzl, S. Wagner, and J. C. Sturm, "Double-heterojunction crystalline silicon solar cell fabricated at 250°C with 12.9% efficiency," *IEEE Journal of Photovoltaics*, vol. 3, no. 1, pp. 330–335, 2013.

[13] D. Zielke, A. Pazidis, F. Werner, and J. Schmidt, "Organic-silicon heterojunction solar cells on *n*-type silicon wafers: The BackPEDOT concept," *Solar Energy Materials and Solar Cells*, vol. 131, pp. 110–116, 2014.

[14] D. Zielke, C. Niehaves, W. Lövenich, A. Elschner, M. Hörteis, and J. Schmidt, "Organic-silicon solar cells exceeding 20% efficiency," *Energy Procedia*, vol. 77, pp. 331–339, 2015.

[15] R. Gogolin, D. Zielke, A. Descoeudres, M. Despeisse, C. Ballif, and J. Schmidt, "Demonstrating the high V_{oc} potential of PEDOT:PSS/c-Si heterojunctions on solar cells," *Energy Procedia*, vol. 124, p. 593–597, 2017.

[16] Y. Zhang, R. Liu, S. Lee, and B. Sun, "The role of a LiF layer on the performance of poly(3,4-ethylenedioxythiophene):poly(styrene sulfonate)/Si organic-inorganic hybrid solar cells," *Applied Physics Letters*, vol. 108, no. 8:083514, 2014.

[17] M. Pietsch, S. Jäckle, and S. H. Christiansen, "Interface investigation of planar hybrid *n*-Si/PEDOT:PSS solar cells with open circuit voltages up to 645 mV and η of 12.6%," *Applied Physics A*, vol. 115, no. 4, p. 1109–1113, 2014.

[18] H. Wen, H. Cai, Y.Du, X. Dai, Y. Sun, J.Ni, J. Li, D. Zhang, and J. Zhang, "Improving the organic/Si heterojunction hybrid solar cell property by optimizing PEDOT:PSS film and with amorphous silicon as back surface field," *Applied Physics A*, vol. 123, no. 14, 2017.

[19] K. A. Nagamatsu, "12% efficient silicon/PEDOT:PSS heterojunction solar cell fabricated at $< 100°C$," *IEEE Journal of Photovoltaics*, vol. 4, no. 1, pp. 260–264, 2014.

[20] D. Zielke, R. Gogolin, M. U. Halbich, C. Marquardt, W. Lövenich, R. Sauer, and J. Schmidt, "Large-area PEDOT:PSS/c-Si heterojunction solar cells with screen-printed metal contacts," *Sol RRL*, vol. 2, no. 3:1700191, 2018.

[21] M. Schwoerer and H. C. Wolf, *Organische Molekulare Festkörper*, vol. 1. Berlin, Germany: Wiley-VCH. p.101-112, May 2005.

[22] M. Härtel, G. Kossmehl, G. Manecke, W. Wille, D. Wöhrle, and D. Zerpner, "Struktur und elektrische leitfähigkeit von polymeren organischen halbleitern," *Macromolecular Materials and Engineering*, vol. 29, no. 1, pp. 307–347, 1973.

[23] M. A. Fox and J. K. Whitesell, *Organische Chemie.* Berlin, Germany: Spektrum Akademischer Verlag. p. 81, 1995.

[24] E. Riedel, *Allgemeine und Anorganische Chemie*, vol. 10. de Gruyter, Berlin, New York. p.78-81, May 1994.

[25] C. Hamann, J. Heim, and H. Burghardt, *Organische Leiter, Halbleiter und Photoleiter.* Berlin, Germany: Wissenschaftliche Taschenbücher Band 252. Akademie-Verlag, 1980. p.58.

[26] H. Bässler, "Charge transport in disordered organic photoconductors a monte carlo simulation study," *Physica Status Solidi B*, vol. 175, no. 1, pp. 15–56, 1993.

[27] C. Hamann, J. Heim, and H. Burghardt, *Organische Leiter, Halbleiter und Photoleiter.* Berlin, Germany: Wissenschaftliche Taschenbücher Band 252. Akademie-Verlag. p.62, 1980.

[28] "Neue polythiophene, verfahren zu ihrer herstellung und ihre verwendung." F. Jonas, G. Heywang and W. Schmidtberg, Deutschland Patent DE 3813589, 1988-04-22.

[29] A. Elschner, S. Kirchmeyer, W. Lövenich, U. Merker, and K. Reuter, *PEDOT:Principles and Applications of an Intrinsically Conductive Polymer.* Boca Raton, FL: CRC Press. p.144,-150, 2011.

[30] U. Land, E. Müller, and N. N. und J. Dual, "Microscopical investigations of PEDOT:PSS thin films," *Advanced Functional Materials*, vol. 19, no. 8, pp. 1215–1220, 2009.

[31] A. M. Nardes, M. Kemerink, and R. A. J. Janssen, "Microscopic understanding of the anisotropic conductivity of PEDOT:PSS thin films," *Advanced Materials*, vol. 19, no. 9, pp. 1196–1200, 2007.

[32] A. Elschner, S. Kirchmeyer, W. Lövenich, U. Merker, and K. Reuter, *PEDOT:Principles and Applications of an Intrinsically Conductive Polymer*. Boca Raton, FL: CRC Press. p.194,-198, 2011.

[33] A. Elschner, S. Kirchmeyer, W. Lövenich, U. Merker, and K. Reuter, *PEDOT:Principles and Applications of an Intrinsically Conductive Polymer*. Boca Raton, FL: CRC Press. p.238-244, 2011.

[34] R. Brendel and R. Peibst, "Contact selectivity and efficiency in crystalline silicon photovoltaics," *IEEE Journal of Photovoltaics*, vol. 6, no. 6, pp. 1413–1420, 2016.

[35] J. Schmidt, R. Brendel, and R. Peibst, "Surface passivation of crystalline silicon solar cells: Present and future," *Solar Energy Materials and Solar Cells*, vol. 187, pp. 29–54, 2018.

[36] R. Brendel, M. Rienäcker, and R. Peibst, "A quantitative measure for the carrier selectivity of contacts to solar cells," *Proceedings 32nd European Photovolt. Solar Energy Conference, Munich, Germany*, pp. 447–451, 2016.

[37] M. J. Kerr and A. Cuevas, "Very low bulk and surface recombination in oxidized silicon wafers," *Semiconductor Science and Technology*, vol. 17, no. 1, pp. 35–38, 2001.

[38] M. J. Kerr, J. Schmidt, A. Cuevas, and J. H. Bultman, "Surface recombination velocity of phosphorus-diffused silicon solar cell emitters passivated with plasma enhanced chemical vapor deposited silicon nitride and thermal silicon oxide," *Journal of Applied Physics*, vol. 89, no. 7, pp. 3821–3826, 2001.

[39] J. Schmidt, M. Kerr, and A. Cuevas, "Surface passivation of silicon solar cells using plasma-enhanced chemical-vapour-deposited SiN films and thin thermal SiO_2/plasma SiN stacks," *Semiconductor Science and Technology*, vol. 16, no. 3, 2001.

[40] A. Aberle, T. Lauinger, J. Schmidt, and R. Hezel, "Injection-level dependent surface recombination velocities at the silicon-plasma silicon nitride interface," *Applied Physics Letters*, vol. 66, no. 2828, 1995.

[41] C. Leguijt, P. Lölgen, J. Eikelboom, A. Weeber, F. Schuurmans, W. Sinke, P. Alkemade, P. Sarro, C. Maree, and L. Verhoef, "Low-temperature surface passivation for silicon solar cells," *Solar Energy Materials and Solar Cells*, vol. 40, pp. 297–345, 1996.

[42] T. Lauinger, J. Schmidt, A. Aberle, and R. Hezel, "Record low surface recombination velocities on 1 Ωcm *p*-silicon using remote plasma silicon nitride passivation," *Applied Physics Letters*, vol. 68, p. 1232, 1996.

[43] J. Schmidt and A. Aberle, "Carrier recombination at silicon-silicon nitride interfaces fabricated by plasma-enhanced chemical vapor deposition," *Journal of Applied Physics*, vol. 95, p. 3626, 1999.

[44] B. Hoex, S. B. S. Heil, E. Langereis, M. C. M. van de Sanden, and W. M. M. Kessels, "Ultralow surface recombination of c-Si substrates passivated by plasma-assisted atomic layer deposited Al_2O_3," *Applied Physics Letters*, vol. 89, no. 04112, 2006.

[45] J. Schmidt, A. Merkle, R. Brendel, M. van de Sanden, and W. Kessels, "Surface passivation of high-efficiency silicon solar cells by atomic-layer-deposited Al_2O_3," *Progress in Photovoltaics: Research and Applications*, vol. 16, pp. 461–466, 2008.

[46] J. Schmidt, B. Veith, and R. Brendel, "Effective surface passivation of crystalline silicon using ultrathin Al_2O_3 films and Al_2O_3/SiN_x stacks," *Physica Status Solidi-Rapid Research Letters*, vol. 3, no. 9, pp. 287–289, 2009.

[47] M. Hofmann, C. Schmidt, N. Kohn, J. Rentsch, S. W. Glunz, and R. Preu, "Stack system of PECVD amorphous silicon and pecvd silicon oxide for silicon solar cell rear side passivation," *Progress in Photovoltaics*, vol. 16, no. 6, pp. 509–518, 2008.

[48] M. Schaper, J. Schmidt, H. Plagwitz, and R. Brendel, "20.1%-efficient crystalline silicon solar cell with amorphous silicon rear-surface passivation," *Progress in Photovoltaics*, vol. 13, no. 5, pp. 381–386, 2005.

[49] A. Descoeudres, L. Barraud, S. D. Wolf, B. Strahm, D. Lachenal, C. Guérin, Z. C. Holman, F. Zicarelli, B. Demaurex, J. Seif, J. Holovsky, and C. Ballif,

"Improved amorphous/crystalline silicon interface passivation by hydrogen plasma treatment," *Applied Physics Letters*, vol. 99, no. 123506, 2011.

[50] A. Aberle, S. Glunz, and W. Warta, "Field effect passivation of high efficiency silicon solar cells," *Solar Energy Materials and Solar Cells*, vol. 29, no. 178, 1993.

[51] J. Schmidt, A. Merkle, R. Bock, P. Altermatt, A. Cuevas, N. Harder, B. Hoex, M. Sanden, W. Kessels, and R. Brendel, "Progress in the surface passivation of silicon solar cells," *Proceedings 23rd European Photovoltaic Solar Energy Conference, Valencia, Spain*, pp. 974–981, 2008.

[52] A. Cuevas, "The recombination parameter J_0," *Energy Procedia*, vol. 55, pp. 53–62, 2014.

[53] A. Cuevas, "Applications of the quasi-steady-state photoconductance technique," *Proceedings of the 2nd World Conference on Photovoltaic Energy Conversion, Vienna, Austria*, 1998.

[54] D. E. Kane and R. M. Swanson, "Measurement of the emitter saturation current by a contactless photoconductivity decay method," *Proceedings of the 18th IEEE PVSC, Las Vegas, USA*, pp. 578–581, 1985.

[55] S. Sze, *Physics of Semiconductor Devices*, vol. 1. Wiley, New York,. p.85, 1981.

[56] S. Sze, *Physics of Semiconductor Devices*, vol. 1. Wiley, New York,. p.366, 1981.

[57] H. Flietner, "Passivity and electronic properties of the silicon/silicon dioxide interface," *Materials Science Forum*, vol. 73, pp. 185–188, 1995.

[58] A. S. Grove and D. J. Fritzgerald, "Surface effects in *p-n* junctions: Charactersistics of surface-charge regions under non-equilibrium conditions," *Solid State Electronics*, vol. 9, pp. 783–806, 1966.

[59] R. B. M. Girisch, R. P. Mertens, and R. F. de Keersmaecker, "Determination of Si-SiO$_2$ interface recombination parameters using a gate-controlled point-junction diode under illumination," *IEEE Transactions on Electron Devices*, vol. 35, no. 2, pp. 203–222, 1988.

[60] A. G. Aberle, S. Glunz, and W. Warta, "Impact of illumination level and oxide parameters on shockley–read–hall recombination at the Si/SiO$_2$ interface," *Journal of Applied Physics*, vol. 71, pp. 4422–4431, 1992.

[61] R. A. Sinton, "Contactless determination of current–voltage characteristics and minority-carrier lifetimes in semiconductors from quasi-steady-state photoconductance data," *Applied Physics Letters*, vol. 69, no. 2510, 1996.

[62] H. Nagel, C. Berge, and A. G. Aberle, "Generalized analysis of quasi-steady-state and quasi-transient measurements of carrier lifetimes in semiconductors," *Journal of Applied Physics*, vol. 86, no. 6218, 1999.

[63] D. H. Neuhaus, P. J. Cousins, and A. G. Aberle, "Trapping and junction-related perbutations of the effective excess carrier lifetime," *3rd World Conference on Photovoltaic Energy Conversion Osaka Japan*, 2003.

[64] S. Jäckle, M. Mattiza, M. Liebhaber, G. Brönstrup, M. Romme, K. Lips, and S. Christiansen, "Junction formation and current transport mechanisms in hybrid n-si/pedot:pss solar cells," *Scientific Reports*, vol. 5, no. 13008, pp. 1–12, 2015.

[65] M. Bail, M. Schulz, and R. Brendel, "Space-charge region-dominated steady-state photoconductance in low-lifetime Si wafers," *Applied Physics Letters*, vol. 82, no. 5, pp. 757–759, 2003.

[66] P. J. Cousins, D. H. Neuhaus, and J. E. Cotter, "Experimental verification of the effect of depletion-region modulation on photoconductance lifetime measurements," *Journal of Applied Physics*, vol. 95, no. 4, pp. 1854–1858, 2004.

[67] B. A. Veith-Wolf, S. Schäfer, R. Brendel, and J. Schmidt, "Reassessment of intrinsic lifetime limit in n-type crystalline silicon and implication on maximum solar cell efficiency," *Solar Energy Materials and Solar Cells*, vol. 186, pp. 194–199, 2018.

[68] R. H. Cox and H. Strack, "Ohmic contacts for GaAs devices," *Solid-State Electronics*, vol. 10, pp. 1213–1218, 1967.

[69] S. S. Winterton and N. G. Tarr, "An improved version of the cox and strack technique for contact resistivity measurement," *Semiconductor Science Technology*, vol. 6, pp. 1061–1065, 1991.

[70] W. Wang, H. Lin, Z. Yang, Z. Wang, J. Wang, L. Zhang, M. Liao, Y. Zeng, P. Gao, B. Yan, and J. Ye, "An expanded cox and strack method for precise extraction of specific contact resistance of transition metal oxide/n-silicon heterojunction," *IEEE Journal of Photovoltaics*, vol. 9, no. 4, 2019.

Bibliography

[71] W. D. Edwards, W. A. Hartman, and A. B. Torrens, "Specific contact resistance of ohmic contacts to gallium arsenide," *Solid-State Electronics*, vol. 15, pp. 387–392, 1972.

[72] R. P. Gupta, J. B. White, O. D. Iyore, U. Chakrabarti, H. N. Alshareef, and B. E. Gnade, "Determination of contact resistivity by the cox and strack method for metal contacts to bulk bismuth antimony telluride," *Electrochemical and Solid-State Letters*, vol. 12, no. 5, 2009.

[73] A. Shepela, "The specific contact resistance of Pd_2Si contacts on n- and p-Si," *Solid State Electronics*, vol. 16, pp. 477–481, 1973.

[74] M. Czerny and A. F. Turner, "Über den astigmatismus bei spiegelspektrometern," *Zeitschrift für Physik*, vol. 61, pp. 792–797, 1930.

[75] J. Huang, P. Miller, J. de Mello, A. de Mello, and D. Bradley, "Influence of thermal treatment on the conductivity and morphology of PEDOT/PSS films," *Synthetic Metals*, vol. 139, pp. 569–572, 2003.

[76] W. Kern, "The evolution of silicon wafer cleaning technology," *Journal of the Electrochemical Society*, vol. 137, no. 6, 1990.

[77] X. Zhand, D. Yand, Z. Yang, X. Guo, B. Liu, X. Ren, and S. Liu, "Improved PEDOT:PSS/c-Si hybrid solar cell using inverted structure and effective passivation," *Scientific Reports*, vol. 6, no. 35091, 2016.

[78] X. Jiang, P. Zhang, J. Zhang, J. Wang, G. Li, X. Fang, and L. Yang, "High performance of PEDOT:PSS/n-Si solar cells based on textured surface with agnws electrodes," *Nanoscale Research Letters*, vol. 13, no. 53, 2018.

[79] Z. Yang, P. Gao, J. He, W. Chen, W. Y. Yin, Y. Zeng, W. Gua, J. Ye, and Y. Cui, "Tuning of the contact properties for high- efficiency Si/PEDOT:PSS heterojunction solar cells," *ACS Energy Letters*, vol. 2, no. 3, p. 556–562, 2017.

[80] J. He, P. Goa, Z. Yang, J. Yu, W. Yu, Y. Zhand, J. Sheng, J. Ye, J. C. Amine, and Y. Cui, "Silicon/organic hybrid solar cells with 16.2% efficiency and improved stability by formation of conformal heterojunction coating and moisture-resistant capping layer," *Advanced Materials*, vol. 29, no. 1606321, 201.

[81] L. Yand, Y. Liu, W. Chen, Y. Wank, H. Liang, Z. Mei, A. Kuznetov, and Y. Du, "Interface engineering of high efficiency organic-silicon heterojunction solar cells," *ACS Applied Materials and Interfaces*, vol. 8, p. 26–30, 2017.

[82] R. Brendel, "Sunrays: A versatile ray tracing program for the photovoltaic community," *European photovoltaic solar energy conference; 12th*, pp. 1339–1342, 1994.

[83] "Sunrays program and user's manual." distributed by Garching Innovation GmbH, c/o M. Pasecky, Königinstr. 19, D-80539 München, Germany.

[84] C. A. Gueymard. Florida Solar Energy Center Report, FSEC-PF-270-95, 1995.

[85] E. D. Palik, *Handbook of Optical Constants of Solids*, vol. 2. Boston, America: Academic Press, 1 ed. p.341-758, 1998.

[86] Z. C. Holman, M. Filipic, B. Lipovsek, S. D. Wolfa, F. Smole, M. Topic, and C. Ballif, "Parasitic absorption in the rear reflector of a silicon solar cell: Simulation and measurement of the sub-bandgap reflectance for common dielectric/metal reflector," *Solar Energy Materials and Solar Cells*, vol. 120, pp. 426–430, 2014.

[87] Z. C. Holman, S. D. Wolf, and C. Ballif, "Improving metal reflectors by suppressing surface plasmon polaritons: a priori calculation of the internal reflectance of a solar cell," *Light: science and applications*, vol. 2, no. e106, 2013.

[88] D. Zielke, J. H. Petermann, F. Werner, B. Veith, R. Brendel, and J. Schmidt, "Contact passivation in silicon solar cells using atomic-layer-deposited aluminum oxide layers," *Physica Status Solidi RRL*, vol. 5, no. 8, p. 298–300, 2011.

[89] C. Zhang, Y. Zhang, H. Guo, Z. Zhang, and C. Zhang, "Hole-transporting layer treatment of planar hybrid *n*-Si/PEDOT:PSS solar cells with power conversion efficiency up to 14.5%," *International Journal of Photoenergy*, vol. 2017, p. 3192197, 2017.

[90] J. Ouyang, Q. Xu, C. Chu, Y. Yang, and J. S. G. Li, "On the mechanism of conductivity enhancement in poly(3,4-ethylenedioxythiophene):poly(styrene sulfonate) film through solvent treatment," *Polymer*, vol. 45, pp. 8443–8450, 2004.

[91] X. Crispin, F. L. E. Jakobsson, A. Crispin, P. C. M. Grim, P. Andersson, A. Volodin, C. van Haesendonck, M. V. der Auweraer, W. R. Salaneck, , and M. Berggren, "The origin of the high conductivity of poly(3,4-

ethylenedioxythiophene)-poly(styrenesulfonate) (PEDOT-PSS) plastic electrodes," *Polymer*, vol. 45, pp. 8443–8450, 2004.

[92] O. Carr, G. Gozzi, L. F. Santos, R. M. Faria, and D. L. Chinaglia, "Analysis of the electrical and optical properties of PEDOT:PSS/PVA blends for low-cost and high-performance organic electronic and optoelectronic devices," *Translational Materials Research*, vol. 2, no. 015002, 2015.

[93] E. Sheha, M. Nasr, and M. K. El-Mansy, "Characterization of poly (vinyl alcohol)/poly(3,4-ethylenedioxythiophene) poly(styrenesulfonate) polymer blend: structure, optical absorption, electrical and dielectric properties," *Physica Scripta*, vol. 88, no. 035701, 2013.

[94] N. G. Fang, J. Wan, H. Zhou, H. Longa, and X. Zhaoa, "Electrospun PEDOT:PSS–PVA nanofiber based ultrahigh-strain sensors with controllable electrical conductivity," *Journal of Materials Chemistry*, vol. 21, no. 47, pp. 18962–18966, 2011.

[95] G. B. Tseghai, D. A. Mengistie, B. Malengier, K. A. Fante, and L. V. Langenhove, "PEDOT:PSS-based conductive textiles and their applications," *Sensors*, vol. 20, no. 1881, 2020.

[96] K. H. Choi, M. Sajid, S. Aziz, and B.-S. Yang, "Wide range high speed relative humidity sensor based on PEDOT:PSS–PVA composite on an idt printed on piezoelectricsubstrate," *Sensors and Actuators A*, vol. 228, pp. 40–49, 2015.

[97] U. Lang, N. Naujoks, and J. Dual, "Mechanical characterization of PEDOT:PSS thin films," *Synthetic Metals*, vol. 159, pp. 473–479, 2009.

[98] C.-H. Chen, A. Torrents, L. Kulinsky, R. D. Nelson, M. J. Madou, L. Valdevit, and J. C. LaRue, "Mechanical characterizations of cast poly(3,4-ethylenedioxythiophene):poly(styrenesulfonate)/polyvinyl alcohol thin films," *Synthetic Materials*, vol. 161, pp. 2259–2267, 2011.

[99] "Conductive coatings." F. Jonas and A. Karbach and B. Muys and E. v. Thillo and R. Wehrmann and A. Elschner and R. Dujardin, European patent EP 0 686 662 B1,1995-04-24.

[100] S. Timpanaro, M. Kemerink, F. J. Touwslager, M. M. D. Kok, and S. Schrader, "Morphology and conductivity of PEDOT/PSS films studied by scanning tunneling microscopy," *Chemical Physics Letters*, vol. 394, pp. 339–343, 2004.

[101] S. Jönsson, J. Birgerson, X. Crispin, G. Greczynski, W. Osikowicz, A. D. van der Gon, W. Salaneck, and M. Fahlman, "The effects of solvents on the morphology and sheet resistance in poly(3,4-ethylenedioxythiophene)–polystyrenesulfonic acid (PEDOT–PSS) films," *Synthetic Metals*, vol. 109, pp. 1–10, 2003.

[102] A. M. Nardes, R. A. J. Janssen, and M. Kemerink, "A morphological model for the solvent-enhanced conductivity of PEDOT:PSS thin films," *Advanced Functional Materials*, vol. 18, pp. 865–871, 2008.

[103] L. A. Pettersson, S. Ghosh, and O. Inganäs, "Optical anisotropy in thin films of poly(3,4-ethylenedioxythiophene)–poly(4-styrenesulfonate)," *Organic Electronics*, vol. 3, pp. 143–148, 2002.

[104] I. V. Zozoulenko, A. Singh, S. K. Singh, V. Gueskine, X. Crispin, and M. Berggren, "Polarons, bipolarons, and absorption spectroscopy of PEDOT," *Applied Polymer Materials*, vol. 1, no. 1, pp. 83–94, 2019.

[105] J. C. Gustafsson, B. Liedberg, and O. Inganäs, "In situ spectroscopic investigations of electrochromism and ion transport in a poly (3,4-ethylenedioxythiophene) electrode in a solid state electrochemical cell," *Solid State Ionics*, vol. 69, no. 2, pp. 145–152, 1994.

[106] H. S. Nalwa, *Handbook of Organic Conductive Molecules and Polymers*, vol. 3. New York, America: Wiley and Sons. p.678-737, April 1997.

[107] A. O. Patil, A. J. Heeger, and F. Wudl, "Optical properties of conducting polymers," *Chemical Reviews*, vol. 88, no. 1, pp. 183–200, 1988.

[108] J. Cornil and J. Brédas, "Nature of the optical transitions in charged oligothiophenes," *Advanced Materials*, vol. 7, no. 3, pp. 195–297, 1995.

[109] S. Demtchenko, N. G. Tarr, and S. McGarry, "Effect of PEDOT band structure on conductive polymer-insulator-silicon junctions," *Journal of Applied Physics*, vol. 122, no. 065502, 2017.

[110] S. S. Kalagia and P. S. Patil, "Secondary electrochemical doping level effects on polaron and bipolaron bands evolution and interband transition energy from absorbance spectra of PEDOT:PSS thin films," *Synthetic Metals*, vol. 220, pp. 661–666, 2016.

Bibliography

[111] J. L. Bredas, R. R. Chance, and R. Silbey, "Comparative theoretical study of the doping of conjugated polymers: Polarons in polyacetylene and poly-paraphenylene," *Physical Review B*, vol. 26, no. 10, 1982.

[112] Q. Qiao, *Organic Solar Cells Materials, Devices, Interfaces, and Modeling*. Boca Raton, Florida, America: CRC Press, 1 ed. p.44-50, March 2015.

[113] J. Nevrela, M. Micjan, M. Novota, S. Kovacova, M. Pavuk, P. Juhasz, J. Kovac, J. Jakabovic, and M. Weis, "Secondary doping in poly(3,4-ethylenedioxythiophene):poly(4-styrenesulfonate) thin films," *Journal of Polymer Science Part B: Polymer Physics*, vol. 53, no. 1139, 2015.

[114] C. O. R. Quiroz, G. D. Spyropoulos, M. Salvador, L. M. Roch, M. Berlinghof, J. D. Perea, K. Forberich, L.-I. Dion-Bertrand, N. J. Schrenker, A. Classen, N. Gasparini, G. Chistiakova, M. Mews, L. Korte, B. Rech, N. Li, F. Hauke, E. Spiecker, T. Ameri, S. Albrecht, G. Abellán, S. León, T. Unruh, A. Hirsch, A. Aspuru-Guzik, and C. J. Brabec, "Interface molecular engineering for laminated monolithic perovskite/silicon tandem solar cells with 80.4% fill factor," *Advanced Functional Materials*, no. 1901476, 2019.

[115] H. W. Heuer, R. Wehrmann, and S. Kirchmeyer, "Electrochromic window based on conducting poly(3,4-ethylenedioxythiophene)–poly(styrene sulfonate)," *Advanced Functional Materials*, vol. 12, no. 2, pp. 89–94, 2002.

[116] S. Khasim, A. Pasha, A. S. Roy, A. Parveen, and N. Badi, "Effect of secondary doping using sorbitol on structure and transport properties of PEDOT–PSS thin films," *Journal of Electronic Materials*, vol. 46, pp. 4439–4447, 2017.

[117] C. Peng, A. H. L. Chow, and C. K. Chan, "Hygroscopic study of glucose, citric acid, and sorbitol using an electrodynamic balance: Comparison with unifac predictions," *Aerosol Science and Technology*, vol. 35, no. 3, pp. 753–758, 2001.

[118] A. Nardes, M. Kemerink, M. de Kok, E. Vinken, K. Maturova, and R. Janssen, "Conductivity, work function, and environmental stability of PEDOT:PSS thin films treated with sorbitol," *Organic Electronics*, vol. 9, pp. 727–734, 2008.

[119] V. Janardhanam, H.-J. Yun, I. Jyothi, J. Lee, H. Hong, V. R. Reddy, and C.-J. Choi, "Energy-level alignment and electrical properties of Al/p-type Si

schottky diodes with sorbitol-doped PEDOT:PSS as an organic interlayer," *Journal of Alloys and Compounds*, vol. 637, pp. 84–89, 2015.

[120] S. Park, S. J. Tark, and D. Kim, "Effect of sorbitol doping in PEDOT:PSS on the electrical performance of organic photovoltaic devices," *Current Applied Physics*, vol. 11, pp. 1299–1301, 2012.

[121] A. K. Havare, M. Cana, S. Demica, M. Kusb, and S. Icli, "The performance of oleds based on sorbitol doped PEDOT:PSS," *Synthetic Materials*, vol. 161, pp. 2734–2738, 2012.

[122] N. Koch, A. Vollmer, and A. Elschner, "Influence of water on the work function of conducting poly(3,4- ethylenedioxythiophene)/poly(styrenesulfonate)," *Applied Physics Letters*, vol. 90, no. 043512, pp. 753–758, 2007.

[123] S. Jäckle, M. Liebhaber, C. Gersmann, M. Mews, K. Jäger, S. Christiansen, and K. Lips, "Potential of pedot:pss as a hole selective front contact for silicon heterojunction solar cells," *Scientific Reports*, vol. 7, no. 2170, pp. 1–8, 2017.

[124] L. Wan, C. Zhang, K. Ge, X. Yang, F. Li, W. Yan, Z. Xu, L. Yang, Y. Xu, D. Song, and J. Chen, "Conductive hole-selective passivating contacts for crystalline silicon solar cells," *Advanced Energy Materials*, vol. 10, no. 16, pp. 1–8, 2020.

[125] R. Wang, Y. Wang, C. Wu, T. Zhai, J. Yang, B. Sun, S. Duhm, and N. Koch, "Direct observation of conductive polymer induced inversion layer in n-si and correlation to solar cell performance," *Advanced Functional Materials*, vol. 30, no. 4, pp. 1–10, 2020.

List of Publications

Parts of this thesis have previously been published in the following publications:

M. -U. Halbich and D. Zielke and R. Gogolin and R. Sauer and W. Lövenich and J. Schmidt, "Reduction of Parasitic Absorption in PEDOT:PSS at the Rear of c-Si Solar Cells", *AIP Conference Proceedings*, vol 1999, no. 04008, pp. 1-6, 2018.

M. -U. Halbich and D. Zielke and R. Gogolin and R. Sauer-Stieglitz and W. Lövenich and J. Schmidt, "Improved Surface Passivation and Reduced Parasitic Absorption in PEDOT:PSS/c-Si Heterojunction Solar Cells through the Admixture of Sorbitol", *Scientific Reports*, vol 9, no. 9775, pp. 1-8, 2019.

M. -U. Halbich and R. Sauer-Stieglitz and W. Lövenich and J. Schmidt, "Improving Organic-Silicon Heterojunction Solar Cells through the Admixture of Sorbitol", *Proceedings of the 36th European Photovoltaic Energy Conference 2019*, pp. 214-218, 2019.

Other publications:

D. Zielke, R. Gogolin, M. -U. Halbich, C. Marquardt, W. Lövenich, R. Sauer, and J. Schmidt, "Large-Area PEDOT:PSS/c-Si Heterojunction Solar Cells with Screen-Printed Metal Contacts," *Solar RRL*, vol. 2, no. 3:1700191, 2018.

Parts of this thesis have previously been presented in the following talks:

M. -U. Halbich and D. Zielke and R. Gogolin and R. Sauer and W. Lövenich and J. Schmidt; "Large-Area PEDOT:PSS/c-Si heterojunction Solar Cells", September 9-11, 2017, Silicon Forest, Falkau, Germany.

M. -U. Halbich and D. Zielke and R. Gogolin and R. Sauer and W. Lövenich and J. Schmidt, "Reduction of Parasitic Absorption in PEDOT:PSS at the Rear of c-Si Solar Cells ", March 19-21, 2018, 8th International Conference on Crystalline Silicon Photovoltaics, Lausanne, Switzerland.

M. -U. Halbich and R. Sauer-Stieglitz and W. Lövenich and J. Schmidt, "Improving Organic-Silicon Heterojunction Solar Cells through the Admixture of Sorbitol", September 9-13, 2019, 36th European PV Solar Energy Conference and Exhibition EUPVSEC, Marseille, France.

Danksagung

An dieser Stelle möchte ich mich bei all denjenigen bedanken, die zum Gelingen dieser Arbeit beigetragen haben:

- Prof. Dr. Jan Schmidt für die Übernahme des Referats und die hervorragende wissenschaftliche Betreuung.

- Prof. Dr. Tobias Wietler für die Übernahme des Korreferats.

- Prof. Dr. Stefan Glunz für die Übernahme des Korreferats.

- Prof. Dr. Olaf Lechtenfeld für die Übernahme des Prüfungsvorsitzes.

- Dem PEDOT-Team Ralf Gogolin, Dimitri Zielke und Cornelia Marquardt.

- Valeriya Titova, Dennis Bredemeier, Leilah Helmich, Michael Winter, Dominik Walter, und Boris Veith-Wolf für die fachlichen Diskussionen.

- Tobias Neubert und David Sylla für die Laserprozessierung.

- Michael Weiss und Stefan Beisse für die Instandhaltung der BAK550.

- Sarah Spätlich für Ofenprozesse und Unterstützung im Reinraum.

- Marvin Diederich für die EDX Messung.

- Benjamin Grimm für die Unterstützung bei der Probenprozessierung.

- Meinen Eltern, meinen Großeltern, meiner Schwester, und Sabrina.

Lebenslauf

Persönliche Daten

Name: Marc-Uwe Halbich
Geburtstdatum: 13. August 1990
Geburtsort: Laubach
Nationalität: Deutsch

Schulbildung

1997 - 2001   Theodor-Heuss-Schule Laubach

2001 - 2007   Friedrich-Magnus-Gesamtschule Laubach

2007 - 2010   Laubach Kolleg,
                 Abschluss: Allgemeine Hochschulreife

Wehrersatzdienst

Aug. 2010 - Feb. 2011   Verein für Jugendfürsorge und Jugendpflege e.V. Gießen

Universitätsausbildung

Okt. 2011 - Nov. 2016   Philipps Universität Marburg,
                          Studium der Physik,
                          Abschluss: Master of Science

Anstellung

Feb. 2011 - Okt. 2011   Verein für Jugendfürsorge und Jugendpflege e.V. Gießen

seit Dez. 2016   Institut für Solarenergieforschung Hameln,
                          Wissenschaftlicher Mitarbeiter
                          im Bereich Materialforschung